

# **University of Alberta**

Strategies for Maximizing Signal to Noise in Decoupled Receive Coil Arrays for  
Magnetic Resonance Imaging  
by

Adam Mitchell Maunder

A thesis submitted to the Faculty of Graduate Studies and Research  
in partial fulfillment of the requirements for the degree of

Masters of Science  
in  
Biomedical Engineering

Department of Electrical and Computer Engineering

©Adam Mitchell Maunder  
Fall 2013  
Edmonton, Alberta

Permission is hereby granted to the University of Alberta Libraries to reproduce single copies of this thesis and to lend or sell such copies for private, scholarly or scientific research purposes only. Where the thesis is converted to, or otherwise made available in digital form, the University of Alberta will advise potential users of the thesis of these terms.

The author reserves all other publication and other rights in association with the copyright in the thesis and, except as herein before provided, neither the thesis nor any substantial portion thereof may be printed or otherwise reproduced in any material form whatsoever without the author's prior written permission.

# **Abstract**

Designing radio frequency coil arrays for optimal Magnetic Resonance Imaging (MRI) has been a wide area of interest for many years. The optimum coil type for high density arrays and the mitigation of coupling between elements in arrays are significant problems addressed in this thesis.

Coupling causes signal and noise transfer between coils, which affects optimum preamplifier noise matching, can cause resonant frequency splitting and degrade individual coil sensitivities. A theoretical framework for modeling capacitive coupling between array elements is developed and it is shown that coils can be completely decoupled by modified capacitive coupling without loss of SNR performance.

Composite coils are three naturally decoupled orthogonal coils. During the design and testing of an 8-coil composite coil array their potential benefits in terms of SNR and parallel imaging are demonstrated. Also, composite arrays are compared to surface arrays with equal element count in relation to the maximum theoretical performance.

## Acknowledgements

I would like to thank my supervisors Dr. Nicola De Zanche, Dr. Mojgan Daneshmand and Dr. Pedram Mousavi; their expertise and patience were instrumental in the creation of this thesis. Without their support my graduate experience would not have been half as enjoyable.

I would also like to express my appreciation for the backing of my parents Darol Maunder and Darlene Werner, financial and otherwise, throughout this two year process. They have made me the person I am, for better or for worse, and they have provided me with all the opportunities for personal growth and pursuing my interests I could desire.

Most importantly, I want to express my love and appreciation to Lindsay Canham, who was most affected by the sporadic and sustained series of sleepless nights that ensues when developing a thesis. She has been a source of reprieve from the drudgery of relentless work and remains a constant beacon of happiness in my life.

# Contents

<b>Chapter 1.....</b>	<b>1</b>
1.1    From Proton to Magnetization .....	2
1.2    From Magnetization to Signal.....	4
1.3    From Signal to Image .....	7
1.4    Radio-Frequency Coils.....	9
1.4.1. Homogeneous Resonators .....	9
1.4.2. Arrays .....	10
1.4.3. Image Data Combination .....	11
1.4.4. Coil matching .....	13
1.4.5. Coil Coupling .....	14
1.5    Noise Covariance and Correlation from Impedance Matrices .....	15
1.6    Approaching Ultimate SNR .....	17
1.7    Measurement Techniques.....	18
1.7.1. VNA measurement of impedances.....	18
1.7.2. Q factor measurement .....	19
1.7.3. Preamplifier Decoupling and Coil Detuning.....	19
1.8    Thesis Summary.....	20
Bibliography .....	21
<b>Chapter 2 .....</b>	<b>26</b>
2.1. Introduction .....	26
2.2. Capacitive Coupling Models .....	27
2.2.1. Lumped Model .....	28
2.2.2. Distributed Model .....	29
2.3. Methods .....	30
2.3.1. Simulations.....	30
2.3.2. Experimental Arrays .....	33
2.3.3. Measurements.....	34
2.4. Results .....	35
2.4.1. Impedance Parameters.....	35

2.4.2. Fitted Parameters.....	39
2.4.3. Coil Current Transfer .....	41
2.4.4. Comparison of Coupling Situations .....	42
2.5. Conclusion .....	46
Bibliography .....	47
<b>Chapter 3 .....</b>	<b>26</b>
3.1. Introduction .....	50
3.2. Theory of Composite Coils.....	51
3.3. Construction.....	52
3.3.1. Matching and Transmit Detuning .....	53
3.3.2. Cabling .....	55
3.4. Upright coil height optimization.....	56
3.4.1. Simulation using the Finite Element Method.....	59
3.5. Experimental Methods.....	60
3.5.1. Imaging Measurements .....	60
3.6. Comparison of Upright Coil Orientations .....	60
3.6.1. Simulation .....	61
3.6.2. Noise Correlation and SNR.....	62
3.7. Full Array Results.....	64
3.7.1. Noise Correlation .....	64
3.8. SNR improvements.....	65
3.8.1. Constant phase combination .....	65
3.8.2. Optimal SNR combination.....	67
3.8.3. Effect of Noise Correlation .....	69
3.9. Parallel Imaging Performance .....	70
3.10. Conclusion .....	72
Bibliography .....	74
<b>Chapter 4 .....</b>	<b>74</b>
4.1. Introduction .....	76
4.2. Theory.....	77
4.2.1. Noise and Signal Calculation .....	77

4.2.2. uiSNR in sphere calculation.....	80
4.3. Methods .....	81
4.3.1. Three Coil Array Comparison.....	81
4.3.2. Coils on a Sphere.....	83
4.3.3. Coupling Comparison .....	86
4.3.4. Realistic Noise Comparison .....	87
4.4. Results .....	89
4.4.1. Three Coil Array Comparison.....	89
4.4.2. Coupling of Arrays.....	92
4.4.3. SNR with Matching Networks and Preamplifier Noise .....	93
4.4.4. SNR with varying Preamplifier Input Impedance .....	94
4.4.5. Individual Coil Noise Factors .....	96
4.4.6. SNR of Arrays compared to uiSNR .....	98
4.4.7. Parallel Imaging Comparison .....	102
4.5 Summary.....	105
Bibliography .....	106
<b>Chapter 5 .....</b>	<b>109</b>
5.1. Summary.....	109
5.2. Conclusion .....	110
5.3. Future Work.....	111

# List of Tables

Table 2-1: Capacitors used in two-coil array simulations depicted in Figure 2.2a32	
Table 2-2: Model parameters for the two-coil array obtained by fitting using the lumped and distributed models; the array has the standard dimensions and substrate permittivity ( $t = 7$ mm, $s = 2$ mm, $w = 9.5$ mm, $d = 70$ mm, $\epsilon_r = 3.4$ ) ..	39
Table 2-3: 1/g-factors for the 4-coil array up to an acceleration factor of 4.....	46
Table 2-4: Average measured mutual impedances and noise correlation coefficients (%) between adjacent coils.....	46
Table 3-1: Quality factors in unloaded ( $Q_{\text{unloaded}}$ ) and loaded ( $Q_{\text{loaded}}$ ) conditions for all coils used in this study; individual upright coils used for height optimization are made with silver-plated copper wire to facilitate simulations, and surface/upright coils in the final array are made with copper strip. Efficiency $\eta=1 - Q_{\text{loaded}}/Q_{\text{unloaded}}$ [13].....	58
Table 3-2: average SNR comparisons for the 8-coil array: optimal vs. RSS combination and SNR improvement over surface coils only (both with the array oriented parallel and orthogonal to $B_0$ ).....	68
Table 3-3: average and maximum g-factors for the slices shown in Figure 3.14 using surface coils only or with the full 8-coil array for 1-D accelerations in the direction parallel to the array .....	71
Table 4-1: The value of tuning capacitors for each coil in the arrays and the impedance of the coils is listed which is averaged separately over the upright and surface type coils.....	86
Table 4-2: Noise figure (dB) added to individual channel noise variances for matching networks (ESR_L=0.36,ESR_C=0.15) and preamplifiers. The noise figures are either calculated using the diagonal of the N-port covariance matrices or from noise figures of the individual matching networks and preamplifiers when the coils self-resistance is transformed to 50 $\Omega$ .....	97

# List of Figures

1.1: Imaging sequence for a spin echo method with Cartesian sampling of k-space. The sequence is repeated for each value of the phase encoding required and a new line in the frequency encoding direction is acquired until all the required lines of k-space are obtained.....	8
1.2: Equivalent circuit diagram of coils with matching networks (a) $C_m$ and $L_m$ form a quarter wave lattice balun that matches the circuit to 50 ohms and provides preamplifier decoupling by inverting the preamp's input impedance, $Z_{pre}$ . $C_t$ provides detuning with $L_{trap}$ when diodes D are forward biased. (b) Upright coils: $C_m, C_{m2}, C_{m3}$ and $L_m$ are used to match the coil impedance to $50 \Omega$ , while $C_t$ and $C_b$ provide tuning. The reactance of $C_b$ is such that the voltages across $C_b$ and $C_{m3}$ are equal and opposite relative to the coaxial cable's ground. ....	13
1.3: Equivalent circuit of coupled coils .....	15
2.1: Models for representing capacitive coupling between two coils. (a) Segmentation of coils into sections affected by stray capacitance (") and sections that are not ('). (b) Lumped capacitance circuit model. (c) Distributed capacitance model.....	27
2.2. (a) Coil geometry used in two-coil array simulations and construction. (b) Geometry used in construction of four-coil array.....	31
2.3: Phantom used for measurements with two coil array. Grid planes that provide inside image contrast are visible.....	35
2.4: Fitting and Simulation results for the 2-port mutual impedance parameters at a) 128 and b) 300 MHz. Dots are simulation results, solid lines prediction using distributed model and dashed lines predictions with the lumped model. ....	36
2.5. Predicted a) Change in resistive coupling coefficient and b) change in mutual inductance due only to stray capacitive coupling ( $C_2=0$ ) predicted using the distributed capacitance model. Arrows indicate actual resistance and inductance values obtained at the largest $C_3$ reactance.....	38
2.6. a) stray capacitance and b) inductance of capacitively coupled sections, obtained by fitting data to the distributed capacitance model. Line colors indicate different parameters that are varied while line/marker types indicate frequencies ( $f = 0$ for analytical solution). Points circled in green correspond to the standard parameter values. ....	40
2.7. Simulated current distributions with 1A source circled in red (bottom) show the differences when current transfer between coils act as a shared current path (current on first strip less than source) versus a coupled current loop (current on first strip less than source) . (top) current along coil strip adjacent to second coil	

(C <sub>2</sub> =0). Solid lines with dots are simulated and dashed lines are predicted from using the distributed model.....	41
2.8. Measured S <sub>21</sub> between (a) elements of the two coil array and (b) adjacent elements in the four coil array for three mutual impedance conditions.....	43
2.9: Measured two-coil optimum combination SNR maps and averages for three decoupling cases. Dashed white lines in the ‘No Decoupling’ case indicate the location of coils on the surface for two orientations of the array (parallel or perpendicular to B <sub>0</sub> ).....	44
2.10. Measured four-coil optimal SNR and 1/g-factor maps for an acceleration factor R = 4. The regional differences in SNR visible in the 2-coil array (Figure 10) are eliminated with careful port placement (Figure 2.2). Main differences in the g-factor maps are deep (>7cm) in the phantom where SNR is low and thus of little consequence.....	45
3.1: A composite coil element made up of three isolated orthogonal coils. The signal-producing region is located below the square surface coil (y < 0). .....	51
3.2: the 8-element composite coil array built to measure SNR and parallel imaging performance. ....	53
3.3: various contributions to noise figure for surface and upright coils. The largest difference is due to coil noise which is a much larger contribution in upright coils because they are not in sample-dominated regime. ....	55
3.4 Cable routing and coil orientation relative to B <sub>0</sub> for which the 8-coil array was designed. Coil dimensions and spacing are also shown. ....	56
3.5: upright coils built for comparison with heights ranging between 1 and 4 cm. ....	57
3.6: measured and simulated SNR of upright wire coils and simulated SNR of copper strip coils, averaged in three sagittal slices as a function of coil height and normalized to the maximum SNR achieved with wire coils. The simulated SNR assumes an equivalent series resistance of 0.05 Ω for each of the two tuning capacitors in addition to losses in the coil conductors (0.15-0.30Ω). ....	59
3.7: Plots of resistive ( $r_{12}$ ) and inductive ( $m_{12}$ ) coupling coefficients between upright and surface coils (70×70 mm <sup>2</sup> ) with varying separation. The upright coil is either perpendicular to the direction of separation (triangles), rotated 45° (circles) or oriented parallel to the direction of separation (diamonds). The coefficients were found using Finite Element simulation with HFSS.....	62
3.8: Comparison of upright coil orientations in the parallel/perpendicular direction, a), and rotated by 45°, b). Noise correlation from measured (red) and simulated (green) coil impedance parameters and the values found with noise	

scans are compared for each pair of coils. For simulated and measured values the higher value is the correlation without accounting for the influence of noise from matching circuits and preamplifiers. The lower value is the correlation after correcting for noise added by the matching network and preamplifier. The SNRs are measured in coronal slices 2.5 cm below the phantom surface from the upright elements alone to remove the influence of the surface coil (which is unaltered). The two SNRs of the two arrangements differ by less than 2% (see text). ..... 63

3.9: Noise correlation matrix (magnitude) for the 8-coil array. The diagonal represents the noise level (variance) for each coil normalized to the mean and symbols are placed over the elements to distinguish types of coil-to-coil interaction. Coils within composite elements are enclosed within square boundaries to indicate the values belonging to each triplet. ..... 65

3.10: (a) Maps of SNR improvement over surface coils alone obtained by combining the signals using a constant phase of  $288^\circ$  throughout the image, with the upright coil parallel to the magnetic field (top) and perpendicular to the magnetic field (bottom). (b) Average image SNR normalized to the average from the surface coil alone for different phase combination angles compared to that obtained with optimal SNR combination..... 66

3.11: Improvement in SNR (optimal combination) relative to that with surface coils alone in (a) a coronal slice and (b) a sagittal slice for surface coil images taken with the full array (left) and taken with upright coils removed (right). The solid gray lines indicate the locations of the slices: 1.2 cm below the surface for the coronal slices and through the centre of the array for the sagittal slice. The SNR increase is also shown for the array in the orientation orthogonal to  $B_0$  for (c) a transverse slice and (d) a coronal slice. Approximate locations of the surface coils are shown as thin dashed lines. ..... 67

3.12: optimal SNR as a function of depth into the phantom (left-hand scale) of the 8-coil array or surface coils alone averaged along the direction of  $B_0 \pm 10.5$  cm in 3 sagittal slices (centred with array  $\pm 2.5$  cm in the lateral direction). The SNR of the full array is compared to that from the surface coils in the presence or absence of the upright coils (right-hand scale), and shows that the SNR improvement due to the upright coils does not taper off to zero with depth. ..... 69

3.13: SNR of RSS combination relative to that using optimal combination (wRSS) in (a) a coronal slice and (b) a sagittal slice. The SNR loss using RSS is as high as 6% below the central composite coil and is attributed the significant noise correlation between it and the other elements (especially the adjacent upright elements orthogonal to  $B_0$ )..... 70

3.14: g – 1-factor maps for acceleration factors of 2 and 3 (sagittal view when the array is oriented parallel to  $B_0$ , and axial view in the orthogonal orientation) using only the surface coils or the complete 8-coil array. Arrows indicate direction of  $B_0$  and acceleration (phase encode direction). An acceleration factor of 4 would be

impossible with the surface coils only but is readily achievable with the composite coil array with a mean g-factor of only 1.07 (Table 3-3).....	72
4.1: N-port representation of coil array impedance matrix (Z), matching networks and preamplifiers, .....	79
4.2: (a) Composite coil array design including labels of decoupling and tuning capacitors (blue rectangles) on one coil and (b) surface coil array design with the tuning capacitor locations next to labels. The built arrays are shown in (c), which has the same dimensions as the simulated coils.....	82
4.3: composite and surface arrays. Conductors are placed 1cm from the surface of the sphere. .....	84
4.4: Diagram of an upright and surface coil element used in composite coil arrays with labels of coil dimensions and showing locations where the conductor is 10mm away from the sphere surface. ....	85
4.5: Optimally combined SNR maps of the three-coil surface coil array and composite array in a sagittal slice through the center. The dimensions of the images are indicated on the bottom which is the same for all images.....	90
4.6: Average SNR in sagittal slices relative to the single 12cm diameter surface coil as a function of depth for the (dashed) composite array and (dash-dot) surface coil array. The simulated (blue) and measured (red) single surface coil SNR normalized to their average in the slices is also shown with solid lines. The composite array begins to out-perform the surface coil array at depths of 60mm	91
4.7: Histogram of simulated arrays' (top) noise correlations and (bottom) coupling ratios between elements in composite and surface coil arrays. The average values for the adjacent coil-coil interactions given next to their symbols above the corresponding bars; for the non-adjacent coil interactions that aren't shown the majority are in the lowest range shown. ....	92
4.8: The noise factor contribution to optimum SNR at 128MHz using different lumped element ESRs with an added 0.5dB to the diagonal of the covariance matrix to represent preamplifier noise figure. With the higher ESR values the matching network is the larger noise contributor. ....	94
4.9: The average SNR of 36 (circle markers) and 54 (diamond markers) element arrays shown in Figure 4.4 using an N-port (dashed line) or individually added (solid line) preamplifier noise model at a distance of 0-15mm (left) or 60-75mm (right) from the center. Composite coil arrays (blue) show less sensitivity to the preamplifier input impedance than the surface coil arrays (red). ....	95
4.10: SNR of the arrays and uiSNR in a transverse slice through the center at 128MHz and 300Mhz. In the uiSNR the SNR at the periphery (outer 1.5cm) increases exponentially and is much higher than with the finite coil arrays. ....	99

4.11: Optimally combined SNR for finite coil arrays coils compared to the maximum achieved by all arrays, the ratio of the maximum to uiSNR is shown above each graph. Plots are without preamplifier or matching network noise (left) and ( $Z_{\text{pre}}=6\Omega$ ) with both (right) at 128MHz (ESR\_C=0.15Ω, ESR\_L=0.36 Ω) and 300MHz (ESR\_C=0.23 Ω, ESR\_L=0.55 Ω). The marker and line corresponding to each array size and type is shown in the legend at the top. The right axis is the scale for uiSNR at 128MHz (black dots) and 300MHz (grey dots) and the maximum achieved by finite coil arrays (blue dots, line marker). ..... 100

4.12: Average g-factor inside of the sphere for a central transverse slice for 128MHz and 300MHz. Blue lines are composite coil arrays, red lines are surface coil arrays and the solid black line is the uiSNR g-factors. The array size is indicated by the line type: 18 coils (dotted), 36 coils (dashed) and 54 coils (solid lines). The bottom row is the g-factors with preamplifier and matching network noise included. ..... 103

4.13: g-factor maps for a reduction factor of 5 in a central transverse slice at 128MHZ with realistic noise included. It is readily seen that only the 54 element surface coil array would provide acceptable g-factors at 128MHz (using the 1.2 – average g-factor limit), but as frequency increases the 36 element and 54 element composite and surface coil array have acceptable performance. ..... 104

## **List of Abbreviations**

Magnetic Resonance Imaging (MRI)

Radio-Frequency (RF)

Signal to Noise (SNR)

Nuclear Magnetic Resonance (NMR)

ultimate intrinsic Signal to Noise Ratio (uiSNR)

Vector Network Analyzer (VNA)

# List of Symbols

- $\mu$  - Nuclear magnetic moment
- $\gamma$ -Gyromagnetic ratio
- $J$  -Spin angular momentum
- $I$ -Nuclear spin quantum number
- $m_I$ -Magnetic quantum number
- $E$ -Energy
- $B_0$ -static magnetic field
- $k_b$ -Boltzmann constant
- $T$ -Temperature
- $\omega_0$ -Larmor frequency
- $M_0$ -Thermal Equilibrium Magnetization
- $M_{xy}$ -Transverse magnetization
- $M$ -Magnetization
- $T_1$ -Spin-lattice relaxation time constant
- $T_2$ -Spin-spin relaxation time constant
- $\mathbf{k}(t)$ - Position in k-space (phase accumulation due to gradients)
- $S(\mathbf{k})$ - MRI signal
- $\hat{B}_1^-(r)$ -Left circularly polarized magnetic field produced per unit current
- $\hat{B}_1^+(r)$ -Right circularly polarized magnetic field produced per unit current
- $\alpha$ - Tip angle
- $G_r$ -Linearly varying magnetic field gradient
- $\Delta s$ -Slice thickness
- $B$ -Bandwidth
- $w$ -Weighting coefficients applied to coil data
- $d$ -Pixel intensities for coils
- $\Psi$ -Covariance matrix
- $\widehat{v_s}$ -Open-circuit signal voltage
- $\phi_n$ -Phase shift applied to weighting of coils
- $s$ - Individual coil sensitivities

$g$ - g-factors  
**Z**-Impedance matrix  
R-resistance  
X-reactance  
L-Inductance  
C-Capacitance  
 $m_{12}$ -Magnetic coupling coefficient  
 $r_{12}$ -Resistive coupling coefficient  
**A<sub>I</sub>**-current gains for matching network  
 **$\Gamma$**  –Reflection coefficient matrix  
**G**-gain matix  
**S**-S parameter matrix  
F-noise factor  
NF-noise figure  
 $R_N$ -correlation resistance  
 $Y_{opt}$ -optimum input admittance  
Q-Q factor  
 $f_0$ -Center frequency  
**I**-Current vector  
**V**-Voltage vector  
 $a_\eta$ -forward travelling noise wave  
 $b_\eta$ -reverse travelling noise wave  
 $T_\alpha$ -forward noise parameter  
 $T_\beta$ -reverse noise parameter  
 $T_\Gamma^*$ -correlation noise parameter  
**X<sub>lm</sub>**-Vector spherical harmonic function  
 $Y_{lm}$ -Scalar spherical harmonic function  
 $j_1$ -spherical Bessel function of the first kind  
**s(r)**-basis function sensitivity vector  
 $r_\rho, \theta_p, \phi_p$ -polar coordinates

# **Chapter 1**

## **Background and Motivation**

Magnetic Resonance Imaging (MRI) is one of the most popular medical imaging methods. Among its many often touted benefits, MRI provides the best soft-tissue contrast and does not involve ionizing radiation like computed tomography (CT) and traditional x-ray imaging. Furthermore, different techniques in MRI result in images with varied contrast and the combination of imaging and spectroscopy results in even more important diagnostic information. More advanced techniques such as MR angiography [1, 2], functional MRI (fMRI) [3] and contrast enhanced MRI [4] makes it an even more powerful method. To take the greatest advantage of MRI, research and development into the hardware has been ongoing. The focus of this thesis is the coils used for reception of the radio frequency (RF) signal produced by Nuclear Magnetic Resonance (NMR) in the body.

Strategies for achieving the greatest possible signal-to-noise ratio (SNR) with receive coil arrays is an active area of research because the increasing numbers of elements available for use in arrays, increasing MRI field strength and advanced imaging techniques affect the design criteria and flexibility . Much of the recent research in receive coil arrays has been focused on the following topics: the coil type or combination of types of coils that provide optimum SNR in arrays [5-8], the effect of coupling and external sources of noise on the final image combination [9-11] and design of coil arrays for parallel imaging [12, 13]. The optimum coil type depends on the frequency and anatomy of imaging so there are no clear cut rules, but typically simple loop coils are used. The coupling between coils theoretically may not affect the optimum combination SNR under certain conditions [14], however the degree to which these conditions can be met experimentally has not been explored and additional sources of noise like preamplifiers must be considered. In addition, the parallel imaging performance has an upper limit, similar to the SNR, which depends on the geometry. The real goal in coil array

design for parallel imaging is therefore approaching this limit as closely as possible with the limited number of receiver channels available. This thesis addresses these issues with the main topics of study being the use of composite coil arrays and capacitive coupling/decoupling between coils.

The history of Nuclear Magnetic Resonance (NMR) and MRI follows the revolution in quantum mechanics and as medical imaging has progressed it has remained one of the premier imaging modalities. Detailing the research for which Nobel prizes have been awarded results in an impressive list and illustrates the background of MRI development. The 1944 Nobel Prize in physics was awarded to Isidor Rabi for his method of detecting NMR [15] using an oscillating magnetic field perpendicular to the main static magnetic field termed the molecular beam resonance method. The 1952 Nobel Prize in physics was awarded to Felix Bloch and Edward Mills Purcell for their development of new methods for NMR measurements and discoveries obtained from that [16, 17]. For his work on NMR spectroscopy Richard R. Ernst won the 1991 Nobel Prize in chemistry; the method of applying pulsed gradients during the signal acquisition and applying the Fourier transform to form 2D or 3D images is one of his major contributions to MRI [18]. In 2002 the Nobel Prize in Chemistry was awarded half to Kurt Wüthrich for the techniques he and his associates developed in NMR that enabled accurate determination of the three-dimensional structures of biological molecules in solution [19]. Most recently, the 2003 Nobel Prize in Physiology or Medicine was awarded to Paul C. Lauterbur for his work producing in producing two-dimensional images and localizing signal using NMR by application of linear magnetic field gradients and Sir Peter Mansfield for his development of methods using gradients for extremely fast imaging [20, 21].

## 1.1 From Proton to Magnetization

The constituents of the nucleus in atoms are neutrons and protons, which each have an intrinsic angular momentum called spin. The angular momentum of the nucleons result in a nuclear magnetic moment,  $\mu$ . If the number of neutrons or protons is an even number the combination of the spins result in no magnetic

moment, but if the number of either is odd there is a resulting magnetic moment for the nucleus. The following description of the magnetization of the nuclei in the body is detailed in reference [22]. The magnetic moment of the nucleus is given by

$$\boldsymbol{\mu} = \gamma \mathbf{J} \quad (1.1)$$

where  $\gamma$  is the gyromagnetic ratio and  $\mathbf{J}$  is the spin angular momentum. With a static magnetic field applied the magnetic moment in the direction of the field, conventionally taken to be in the direction of the z-axis, is

$$\mu_z = \gamma \hbar m_I \quad (1.2)$$

The magnetic quantum number  $m_I$  can take on a number of discrete values,  $-I, -I+1, \dots, I$ , where  $I$  is the nuclear spin quantum number and depends on the quantum state of the nucleus; even numbered spins cancel each other so  $I=0$ , while for the hydrogen nucleus (1H)  $I$  is 1/2. The magnitude of the total magnetic moment is

$$|\boldsymbol{\mu}| = \gamma \hbar \sqrt{I(I + 1)} \quad (1.3)$$

which includes  $\mu_z$  and the transverse component of the magnetic moment  $|\boldsymbol{\mu}_{xy}| = \sqrt{|\boldsymbol{\mu}|^2 - \mu_z^2}$  which is randomly oriented. Standard MRI imaging uses signal from hydrogen because it is the most numerous atom present in the human body and the gyromagnetic ratio for the hydrogen nucleus is relatively large ( $\gamma = 42.6$  MHz/T), so the remaining discussion will focus on the simplest case of  $I=1/2$ .

The energy of a magnetic moment in a static magnetic field is

$$E = -\boldsymbol{\mu}_z \cdot \mathbf{B}_0 \quad (1.4)$$

where  $B_0$  is the static magnetic field directed along the z-axis and  $E$  is the energy of the state. For  $I = \frac{1}{2}$  the energy difference between the antiparallel  $I = -1/2$  state and the parallel  $I = 1/2$  state results in a statistically predicted proportion of spins equal to

$$\frac{n_\uparrow}{n_\downarrow} = e^{\frac{\Delta E}{k_b T}} = e^{\frac{\gamma \hbar B_0}{k_b T}} \quad (1.5)$$

Where  $n_\uparrow$  is the number of atoms in the parallel state is,  $n_\downarrow$  is the number of atoms in the anti-parallel state. The energy difference in the two states corresponds to a photon with energy  $\gamma \hbar B_0 = \hbar \omega_0$ , where  $\omega_0$  is known as the Larmor frequency.

In the transverse plane there is no energy difference and the transverse magnetic moment will be random. The change in angular momentum (torque) exerted on the magnetic moment by the static magnetic field is,

$$\frac{\partial(\mathbf{J}\hbar)}{\partial t} = \frac{1}{\gamma} \frac{\partial(\boldsymbol{\mu})}{\partial t} = \boldsymbol{\mu} \times (B_0 \hat{z}) \quad (1.6)$$

Therefore, the change in the magnetic moment will be

$$\frac{\partial(\boldsymbol{\mu})}{\partial t} = \gamma B_0 (\mu_y \hat{x} - \mu_x \hat{y}) = \omega_0 (\mu_y \hat{x} - \mu_x \hat{y}) \quad (1.7)$$

And therefore the nuclei precess about the z-axis with the Larmor frequency  $\omega_0$ . The macroscopic nuclear magnetization along the direction of the static magnetic field is given by the product of their total excess number of spins in a volume and their magnetic moment.

$$M_0 = \frac{N B_0 (\gamma \hbar)^2}{4 k_b T} \quad (1.8)$$

where  $N$  is number of spins per unit volume. With the knowledge of a continuous distribution of magnetization, and the behavior of the magnetization when it is perpendicular to  $B_0$ , the production of a signal is the next step.

## 1.2 From Magnetization to Signal

The total magnetization follows similar equations of motion as individual magnetic moments presented in equation (1.7) except the effects of longitudinal and spin-lattice (transverse) relaxation must be included. This results in the Bloch equation [22], or equation of motion, for the change in magnetization with time,

$$\frac{\partial(\mathbf{M})}{\partial t} = \gamma \mathbf{M} \times \mathbf{B} - \frac{\mathbf{M}_{xy}}{T_2} - \frac{M_z(t) - M_z(0)}{T_1} \hat{z} \quad (1.9)$$

where  $\mathbf{B}$  is the total magnetic field,  $\mathbf{M}_{xy}$  is the transverse magnetization and  $M_z$  is the longitudinal magnetization.

$T_1$  is the longitudinal relaxation time constant and is due to the spins that have been excited coming to thermal equilibrium and losing energy through interactions with neighboring molecules (the lattice). The return to thermal equilibrium results in regaining the magnetization  $\mathbf{M}_0$ .  $T_1$  describes the time scale

on which this spin-lattice relaxation occurs and is defined as the reciprocal of the rate of energy loss[23].

$T_2$  is the transverse relaxation time constant and describes the loss of phase coherence in the transverse magnetization due to variations in the magnetic field produced by neighboring atoms and energy exchanges (spin-spin relaxation). Transverse relaxation occurs faster than longitudinal relaxation (spin-lattice) and in addition to the molecular interactions stated include variations in the magnetic field homogeneity, which shortens the coherence time constant to  $T_2^*$ .  $T_1$ ,  $T_2$  and  $T_2^*$  can be used to provide contrast in MRI images since they vary between different tissues [23].

To have precession of the magnetization that induces signal there first has to be transverse magnetization, which requires applying a rotating magnetic field. This can more easily be described below by converting to the rotating reference frame,

$$\begin{aligned} \mathbf{x}' &= \cos(\omega t) \hat{\mathbf{x}} - \sin(\omega t) \hat{\mathbf{y}} \\ \mathbf{y}' &= \sin(\omega t) \hat{\mathbf{x}} + \cos(\omega t) \hat{\mathbf{y}} \\ \mathbf{z}' &= \hat{\mathbf{z}} \end{aligned} \quad (1.10)$$

With this representation (1.9) is then,

$$\frac{\partial(\mathbf{M})}{\partial t} = \gamma \mathbf{M} \times (\mathbf{B}_0 + \frac{\boldsymbol{\omega}}{\gamma} + \mathbf{B}_1) - \frac{\mathbf{M}_{xy}}{T_2} - \frac{M_z(t) - M_z(0)}{T_1} \hat{\mathbf{z}} \quad (1.11)$$

where  $\mathbf{B}_1$  is an applied rotating magnetic field with angular frequency  $\boldsymbol{\omega}$ . In practice the  $\mathbf{B}_1$  RF field is produced by using a transmit coil that produces a homogenous magnetic field. If the direction of  $\mathbf{B}_1$  is in the transverse plane and has frequency  $\boldsymbol{\omega} = -\gamma \mathbf{B}_0$  then the magnetization rotates about the axis of the applied  $\mathbf{B}_1$  field (in the rotating reference frame) with frequency  $\gamma \mathbf{B}_1$ . For example, in the rotating reference frame if a homogeneous  $\mathbf{B}_1$  field is applied along the x-axis for a time  $\tau$  and the magnetization is initially  $M_0 \hat{\mathbf{z}}$  then the resulting magnetization will be.

$$\mathbf{M} \approx M_0(\cos(\alpha) \mathbf{z}' + \sin(\alpha) \mathbf{y}') \quad (1.12)$$

where,  $\alpha \approx \gamma \int B_1 dt$ . Therefore, the applied RF field  $\mathbf{B}_1$  excites the magnetization into the transverse plane, which will then precess with the Larmor frequency about

the z-axis. The angle of the magnetization can be chosen, as well as the range of frequencies that are excited, by changing the amplitude and shape of the  $\mathbf{B}_1$  pulse. In practice, not all spins in the body have exactly the same Larmor frequency due to: magnet inhomogeneity, variations in tissue permeability and especially the gradient fields produced for spatial encoding. This leads to off-resonance terms in equation (1.11) that affect magnetization and excitation (since  $\omega \neq -\gamma B_0$ ) and requires special consideration in image processing and pulse design. When the  $\mathbf{B}_1$  field is removed the precessing magnetization then induces a voltage ( $V$ ) on the receiving coil given by [22],

$$V(t) = e^{\frac{i\pi}{2}\omega_0 t} \int_V \hat{B}_1^-(r) \mathbf{M}_{xy} e^{-i(2\pi\mathbf{k}(t) \cdot \mathbf{r} + \omega_0 t)} dr, \quad (1.13)$$

$\hat{B}_1^-(r)$  is the component of the left circularly polarized magnetic field produced by the coil per unit current;  $k(t)$  is the position in k-space, which is the gradient in phase accumulated across the image from the time the magnetic gradient fields are applied. This equation indicates that the signal received is proportional to the magnetization as well as the sensitivity of the coil and frequency. Based on this relationship, gains in SNR have been obtained over the years by increasing the MRI system field strength ( $B_0$ ) resulting in a linear increase in the induced voltage and also in the magnetization based on the relationship in equation (1.8). Parallel imaging performance, which depends primarily on the sensitivities of the array elements and noise statistics, also improves with the higher frequencies that results in more structured and distinct sensitivities of the array elements [24]

Typically when looking at the signal expression a simplified version of equation (1.13) is used that assumes the receiver coil has a homogeneous reception, removes the scaling constant  $e^{\frac{i\pi}{2}\omega_0 t}$ , and removes the carrier signal  $e^{-\omega_0 t}$  [22], which is

$$S(\mathbf{k}) = \int_V \mathbf{M}_{xy} e^{-i(2\pi\mathbf{k}(t) \cdot \mathbf{r})} dr, \quad (1.14)$$

where the signal  $S$  is a function  $\mathbf{k}$ .

## 1.3 From Signal to Image

The use of gradients is the standard method of encoding spatial information into the received signal. Three gradient coils are used to create linearly varying DC magnetic fields that depend on position in the x,y, and z axis; like  $B_0$ , the direction of the gradient fields is along the z axis. These gradients create a linear variation in precession frequency with position and k-space can be acquired by sampling while applying the encoding gradients. K-space is defined in terms of the gradients as

$$\mathbf{k}(t) = \frac{\gamma}{2\pi} \int \mathbf{G}_r dt \quad (1.15)$$

where  $\mathbf{G}_r$  is the vector of the gradients applied.

For the production of an image the inverse Fourier transform is performed on the received signal in equation (1.14)

$$\mathbf{M}_{xy} = \int S(\mathbf{k}) e^{i2\pi\mathbf{k}(t)\cdot\mathbf{r}} d\mathbf{k} \quad (1.16)$$

Obtaining the image requires acquiring the signal for each point in k-space and then performing the discrete (2D or 3D depending on imaging) Fourier transform. This equation does not explicitly show the time dependence of  $\mathbf{M}_{xy}$  which arises because of the differences in relaxation between tissues and the imaging sequence timings.

One of the most common imaging acquisition sequences is the spin echo sequence shown in Figure 1.1 [20]. First, a sinc-shaped  $B_1$  RF pulse is applied by the homogeneous resonator, while a gradient magnetic field is applied, which excites a slice perpendicular to the gradient with thickness

$$\Delta s = \frac{2\pi B_{rf}}{\gamma G_s}, \quad (1.17)$$

where  $\Delta s$  is the slice thickness,  $G_s$  is the gradient strength in T/m and  $B_{rf}$  is the frequency bandwidth of the sinc pulse. Since the magnetization has a non-linear dependence on the applied  $B_1$  with frequency the sinc pulse is only an approximation for low tip-angles. For large angles of rotation, such as 180 degree refocusing pulses, selective RF pulses must be designed that account for the non-

linearity. A common method is the Shinnar-Leroux transformation algorithm, which makes use of the hard-pulse approximation [25].

A 180 degree pulse is applied after a time  $TE/2$  with the same  $\mathbf{G}_s$  to flip the transverse magnetization in that slice, which then refocuses  $TE/2$  later. In Figure 1.1 a since shaped pulse is shown, but in practice the shape is more complicated. A phase encoding gradient,  $G_p$ , is applied before the 180 degree pulse to set the position in k-space for the phase encoding direction. Then as the signal refocuses the signal is acquired with the frequency encoding gradient,  $G_f$ , applied during acquisition. In this way all the points of the frequency encoding k-space  $k_f = \gamma\tau_f G_f$  is found for each value of  $k_p = \gamma\tau_p G_p$ . The same sequence is repeated for each value of  $k_p$  until the full 2D k-space is acquired.

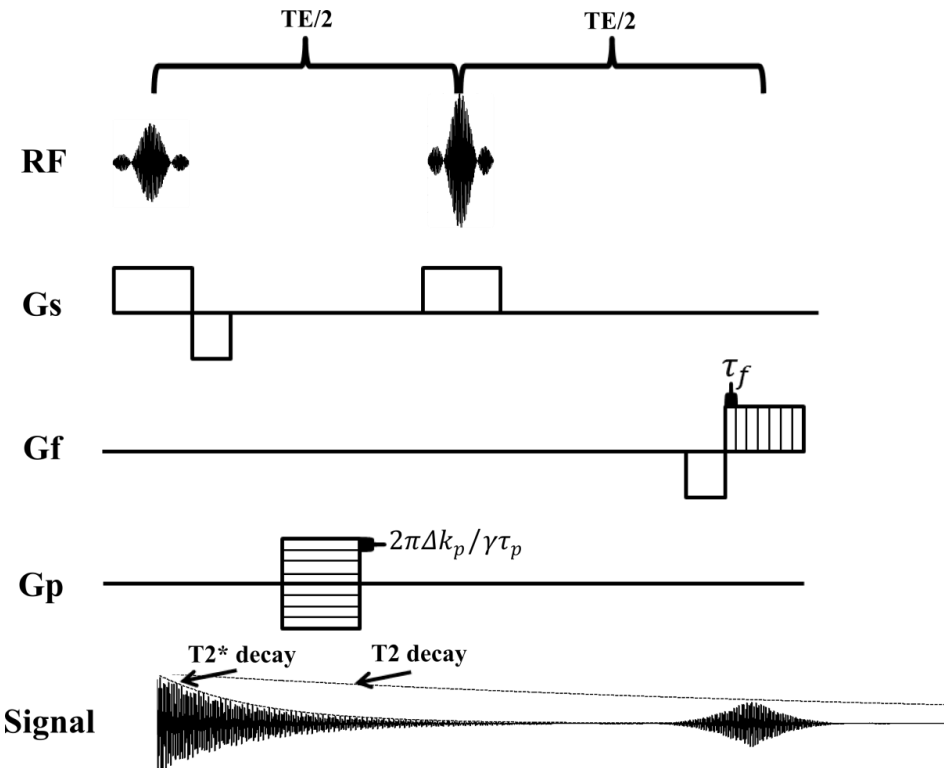


Figure 1.1: Imaging sequence for a spin echo method with Cartesian sampling of k-space. The sequence is repeated for each value of the phase encoding required and a new line in the frequency encoding direction is acquired until all the required lines of k-space are obtained.

The image contrast in the reconstructed image is provided by the spin density (from the term  $M_{xy}$ ), the difference in longitudinal and transverse relaxation times, ( $T_1$  and  $T_2$ ) and in special imaging sequences the flow [2], diffusion [26] and perfusion [23]. The signal diagram in Figure 1.1 shows the two different exponential lines representing the decay in transverse magnetization due to  $T_2$  and  $T2^*$  which are due to spin-spin interactions and static field inhomogeneity respectively.

Various pulse sequences change the contributions of the contrast mechanisms to the final image contrast. Altogether, the MRI soft tissue contrast is comparatively better and more flexible than other medical imaging modalities, particularly with the use of contrast agents that enhance the contrast between normal and diseased tissues.

## 1.4 Radio-Frequency Coils

### 1.4.1. Homogeneous Resonators

A homogeneous resonator is one that ideally produces a uniform  $B_1$  field in the imaging region. Typical resonators that produce suitably homogeneous fields are the Helmholtz coil, birdcage coils [27] or Transverse Electromagnetic (TEM) coil [28]; birdcage coils are the most commonly used for fields <3T.

These axial resonators operate by approximating a current distribution that varies sinusoidally in magnitude around a cylindrical surface [27], which results in a homogeneous field inside the cylinder perpendicular to the cylindrical axis. The RF magnetic field produced with this sinusoidal variation is linearly polarized, but from equation (1.11) it is evident that a rotating (right circularly polarized) magnetic field excites the magnetization (a linearly polarized field can be decomposed into a left and right circularly polarized field). Exciting a second mode on the resonator that approximates a cosinusoidally varying current around the cylinder 90 degrees out of phase with the current produced by the first mode and driving both modes ideally results in a right-circularly polarized field in the imaging volume. The quadrature driven current distribution increases the useful component of magnetic field produced (right circularly polarized) for the same power loss in

the body by a factor  $\sqrt{2}$  [27]. Ideally, these modes are isolated so that there is no power transfer between the ports they are driven from. For higher magnetic field strengths ( $>3\text{T}$ ) the use of transmit coil arrays [29, 30] is an area of active research since a single resonator cannot produce the required homogeneous field as far-field wavelength effects become unavoidable.

### 1.4.2. Arrays

The use of receiver coil arrays has become standard practice in MRI since their introduction in the mid-1980s [31, 32] and subsequent refinements by Roemer et al. [33] and others. They are essential for achieving the highest possible signal-to-noise ratio (SNR) in standard MRI and also to take advantage of parallel imaging techniques [34-36]. Arrays are composed of multiple coil loops [37], or other resonant structures such as microstrip coils [7], arranged to cover the surface of the desired volume of interest (VOI). Loops are by far the most common array coil elements due to their low profile and ability to become readily transparent to the  $B_1$  fields of a separate volume transmit coil by using active or passive detuning traps [38, 39].

The use of coils in MRI differs from antennas used in communications primarily because the MRI signal received is due to induction rather than the reception of radiated electromagnetic waves. Consequently, the sensitivity (phase and amplitude) of coils depends on their near field behavior and varies considerably in the imaging region. In addition, the noise picked up by coils comes primarily from eddy current losses in the lossy imaging region and there is significant noise correlation between elements in arrays. Therefore, the optimum signal combination between array elements varies considerably with position in the phantom and fixed phase combination is not practical for arrays (except quadrature combined elements).

The RF coils that receive signal from the excited spins are usually different from the system that excites the spins. The transmit coil, or array, is designed to create a homogeneous  $B_1$  field, while receive coils have a higher sensitivity within the region local to them and pick up less noise from the imaging volume. The

introduction of the phased coil array, where the signal is received by a number of coils with separate channels and then combined together, was an important advance in MRI imaging capabilities since the FOV with high Signal to Noise Ratio (SNR) is expanded compared to the using of a single surface coil. The individual elements of the array have a higher localized sensitivity in their region of coverage and pick up less noise from the body, this results in the final combined image from the array having an overall higher SNR than would be possible from a single large coil covering the same area. A fair comparison of the performance of a single coil to an array of coils requires that the positioning and size of both is optimized for imaging the same desired volume, or that they at least cover the same imaging area.

Additional challenges arise in using arrays of coils, namely the coupling between coils has the potential to degrade the receive performance and the receive coils must be detuned during transmit to prevent induced currents on the receive coil that can damage components, negatively interfere with the homogeneous  $B_1$  field and create a heating/burn safety hazard. Preamplifier decoupling is commonly used to reduce the coupling between coils, where a large impedance is presented by the preamplifier/matching network that suppresses the current and reduces crosstalk between coils. For detuning during transmit a DC voltage is provided to PIN diodes in the receive coils which create high impedances along the coil length or at the coil terminals to suppress the induced current [38, 39].

### 1.4.3. Image Data Combination

The pixel value and SNR for a general linear signal combination are given, respectively, at each pixel by

$$\begin{aligned} \rho &\triangleq \mathbf{w}^H \mathbf{d}, \text{ and} \\ \text{SNR} &= \frac{\mathbf{w}^H \mathbf{d}}{\sqrt{\mathbf{w}^H \mathbf{\Psi} \mathbf{w}}} \end{aligned} \quad (1.18)$$

where  $\mathbf{w}$  is a vector containing the weighting coefficients,  $\mathbf{d}$  contains the pixel intensities from each coil, the superscript ( $H$ ) indicates the Hermitian transpose, and  $\mathbf{\Psi}$  is the covariance matrix commonly measured using noise scans [40-42].

If signals from coils are combined using a fixed phase relationship such as by hardware combination the vector of weighting coefficients can be represented by

$$w = [e^{j\phi_1} \quad \dots \quad e^{j\phi_n}] \quad (1.19)$$

where  $\phi_n$  is the constant phase shift applied to the coil signal that is constant throughout the image. In image reconstruction the weighting coefficients,  $\mathbf{w}$ , are often chosen either for optimal SNR, or, for quick and simple reconstruction, the root sum-of-squares (RSS) combination is used [33].

If the image SNR is high, an accurate approximation of the SNR obtained by optimal (Roemer) combination [41] is obtained the weighted root sum-of-squared (wRSS) combination

$$\text{SNR} \cong \text{wRSS} = \sqrt{\mathbf{d}^H \boldsymbol{\Psi}^{-1} \mathbf{d}}. \quad (1.20)$$

The SNR from the more common (unweighted) RSS combination is given by [43]

$$\text{SNR} = \frac{\mathbf{d}^H \mathbf{d}}{\sqrt{\mathbf{d}^H \boldsymbol{\Psi} \mathbf{d}}} \quad (1.21)$$

In the case of uncorrelated coils with the same signal and noise level this would result in a square root dependence for SNR on the number of receive coils. Coils noise is rarely uncorrelated and their sensitivity varies over the volume so the increase in SNR with more coil elements doesn't typically follow this relation, In parallel imaging techniques such as SENSE imaging the SNR obtained by optimal reconstruction is degraded inversely with the square root of the reduction factor and furthermore inversely with the geometry factor [34]

$$g = \sqrt{(\mathbf{s}^H \boldsymbol{\Psi}^{-1} \mathbf{s})^{-1} (\mathbf{s}^H \boldsymbol{\Psi}^{-1} \mathbf{s})} \quad (1.22)$$

where  $\mathbf{s}$  is the sensitivity matrix, and  $\boldsymbol{\Psi}$  is the covariance matrix [34]. The g-factor is an important measure of the parallel imaging performance of an array and measures its ability to encode position information from the coil sensitivity profiles. If the coil sensitivities are very similar the matrix inversion required for SENSE reconstruction becomes ill-conditioned and the g-factor measures the consequent regional decrease in SNR [13].

#### 1.4.4. Coil matching

Correct matching is essential to achieve effective preamplifier decoupling [44] and optimal SNR. Two different matching networks which are used to provide a  $50\Omega$  match to the preamplifier terminals and high blocking impedance, when the input impedance of the preamplifier is low, are shown in Figure 1.2. The quarter-wave lattice balun in Figure 1.2b provides simultaneously, effective balancing and high blocking impedance when connected to a low-input-impedance preamp. Coils with very low resistance, however, require impractically low inductance values for the lattice balun. Instead, the  $\pi$  matching network in Figure 1.2a) is used in that case.

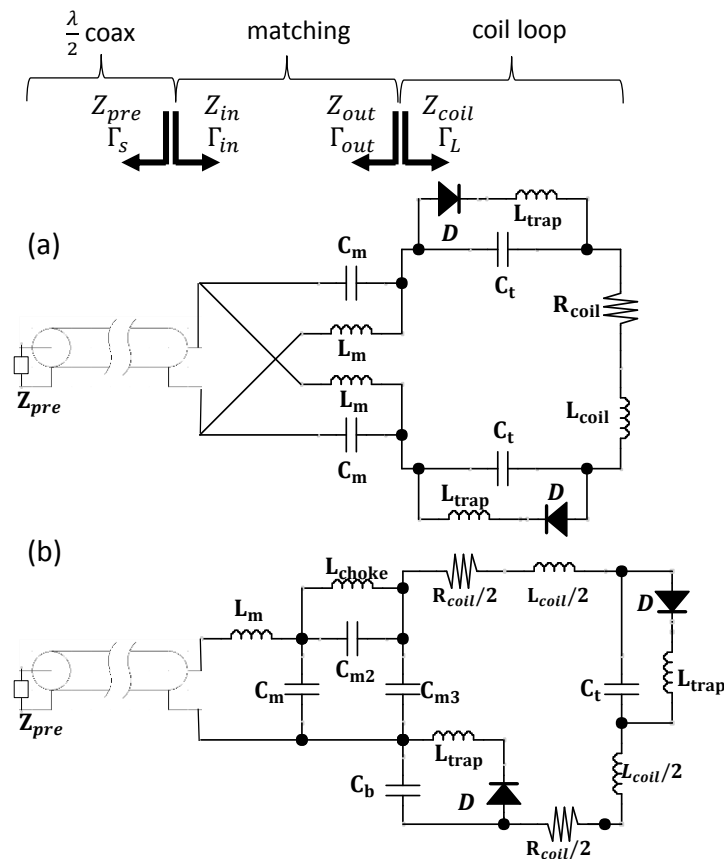


Figure 1.2: Equivalent circuit diagram of coils with matching networks (a)  $C_m$  and  $L_m$  form a quarter wave lattice balun that matches the circuit to  $50 \Omega$  ohms and provides preamplifier decoupling by inverting the preamp's input impedance,  $Z_{pre}$ .  $C_t$  provides detuning with  $L_{trap}$  when diodes  $D$  are forward biased. (b) Upright coils:  $C_m, C_{m2}, C_{m3}$  and  $L_m$  are used to match the coil impedance to  $50 \Omega$ , while  $C_t$  and  $C_b$  provide tuning. The reactance of  $C_b$  is such that the voltages across  $C_b$  and  $C_{m3}$  are equal and opposite relative to the coaxial cable's ground.

### 1.4.5. Coil Coupling

There are many technical challenges to building and using large element count arrays, but this effort is justified by the gains in SNR and possibility of high accelerations. The general design principles to optimize array coil performance were developed more than twenty years ago [33] when field strengths were relatively low ( $f_0 = 64$  MHz at  $B_0 = 1.5$  tesla) and the number of receiver channels was limited (<10). The importance of minimizing crosstalk, the transfer of signal/energy through coupled circuits [45], was realized early on since achieving the superior performance expected with arrays requires good isolation between individual elements to ensure spatially unique sensitivities [46]. Isolation depends on the mutual impedance between coils, including the resistive component which is the source of intrinsic noise correlation [45, 47], i.e., correlation between noise voltages when coils are open-circuited [45]. Standard decoupling methods such as those using reflective preamps [33] or capacitive networks [29, 48-50] remove only the effect of crosstalk that results from mutual reactance between coils[48, 50-52], but they are not effective against mutual resistance.

Mutual impedance is responsible for signal crosstalk and noise correlation between coils [14, 47]. Due to the close proximity of coils in an array it can never be completely eliminated and must therefore be well characterized, e.g., with bench measurements using a Vector Network Analyzer (VNA). The equivalent circuit in Figure 1.3, similar to that in reference [53], is used to define mutual impedance  $Z_{12} = R_{12} + iX_{12}$  between two coils with self-impedance  $Z_{nn} = R_{nn} + iX_{nn}$  when capacitive coupling and electrical delays in transmission lines are absent or calibrated out. The mutual reactance is therefore proportional to the mutual inductance,  $X_{12} = \omega L_{12}$ , where  $\omega$  is the angular frequency of operation. Normalized coupling coefficients can also be defined to quantify the strength of coupling relative to the network's self-impedances. The resistive coupling coefficient is given by  $r_{12} \triangleq R_{12}/\sqrt{R_{11}R_{22}}$

and the inductive coupling coefficient  $m_{12} \triangleq L_{12}/\sqrt{L_{11}L_{22}}$  [33]. The driving-point reactance in practice is cancelled out at resonance by capacitors  $C_1$  and  $C_2$ .

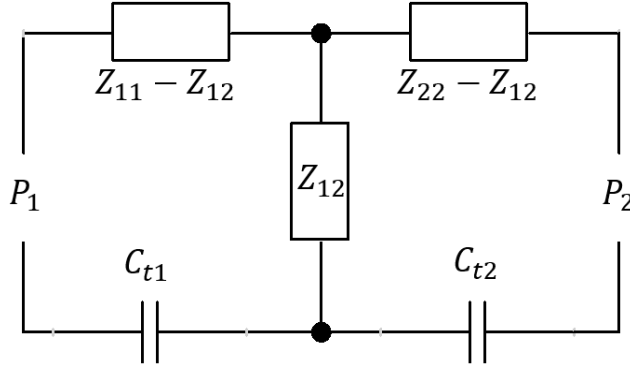


Figure 1.3: Equivalent circuit of coupled coils

## 1.5 Noise Covariance and Correlation from Impedance Matrices

The noise covariance at the preamplifier ports is intimately related to the mutual impedance between coil elements. The covariance matrix of the noise voltages expressed at the input of the preamplifiers can be calculated from the circuit parameters of the coil array as [54]

$$\Psi = (4kBT) \mathbf{A}_I (\tilde{\mathbf{Z}}^{-1}) \mathbb{R}(\mathbf{Z}) (\tilde{\mathbf{Z}}^{-1})^H \mathbf{A}_I^H, \quad (1.23)$$

where  $k$  is the Boltzmann constant,  $B$  is the receiver bandwidth,  $T$  is the absolute temperature,  $\mathbf{A}_I$  is a diagonal matrix of gains that relate the coil currents and corresponding input preamplifier currents,  $Z$  is the impedance matrix at the coil terminals (self and mutual impedances) and  $\tilde{\mathbf{Z}} = \mathbf{Z} + \mathbf{Z}_{block}$  where  $\mathbf{Z}_{block}$  is a diagonal matrix containing the blocking impedances of the matching networks at the coil;  $\mathbb{R}(\mathbf{Z})$  indicates taking the real part of the  $Z$  matrix. The elements of the noise covariance matrix are often normalized to give the noise correlation coefficients

$$\psi_{ab} = \sqrt{\frac{\Psi_{ab}\Psi_{ba}^*}{\Psi_{aa}\Psi_{bb}}} \quad (1.24)$$

which do not depend on the  $\mathbf{A}_I$  matrices or scalar factors  $(4kBT)$ . In addition, if the blocking impedance is very high, as when preamplifier decoupling is used, then  $\tilde{\mathbf{Z}}$

is nearly diagonal and the noise correlation between coils can be closely approximated by the resistive coupling coefficient, which combines the real elements of the impedance matrix [33, 55].

The open circuit signal voltage [55] and the signal produced at the preamplifier ports from a region using the same circuit parameters as for calculating the noise covariance is

$$\begin{aligned}\widehat{\boldsymbol{v}}_{open} &= \omega_0 \Delta V M_0 \widehat{\boldsymbol{B}_1} \\ \boldsymbol{v}_{open} &= \mathbf{A}_I(\tilde{\mathbf{Z}}^{-1}) \widehat{\boldsymbol{v}}_s\end{aligned}\quad (1.25)$$

where  $\widehat{\boldsymbol{B}_1}$  is a vector of the left circularly polarized magnetic fields produced per-unit-current by the coils,  $M_0$  is the magnetization,  $\Delta V$  is voxel volume,  $\widehat{\boldsymbol{v}}_{open}$  is the open-circuit coil voltage and  $\boldsymbol{v}_{open}$  is the signal produced at the preamplifier input terminals. A more relevant comparison value for coil array performance is the open-circuit voltage for equivalent magnetization and voxel volume that is normalized to the Larmor frequency. The relative open-circuit signal is then simply

$$\widehat{\boldsymbol{v}}_s = \widehat{\boldsymbol{B}_1} \quad (1.26)$$

and the relative open-circuit signal  $\widehat{\boldsymbol{v}}_s$  is converted to the signal at the preamplifier input ( $\boldsymbol{v}_s$ ) as  $\widehat{\boldsymbol{v}}_{open}$  is in equation (1.25).

Noise correlation at the coil ports is reduced by the addition of noise from the matching networks and preamplifiers. With sufficiently decoupled coils these additional noise sources affect the noise of each channel independently thus increasing the noise variances (diagonal elements of the covariance matrix) that are at the denominator of equation 1.24. The noise from matching circuit elements originates from the corresponding equivalent series resistances (ESR) and has been shown to result in a significant increase in noise figure for coils whose resistance is not body-dominated [10]. Using the equivalent noise power sources of these resistances and ignoring any coil coupling we can then calculate the individual noise factor (SNR squared at the output relative to that at the input) for the matching networks,  $F_{match}$ , as

$$F_{match} = \frac{R_{in}}{R_{coil}} \left( \frac{(Z_{out} + Z_{coil})}{A_I(Z_{in} + Z_{pre})} \right)^2 = \frac{1}{G_{12}} = \frac{|1 - S_{11}\Gamma_s|^2(1 - |\Gamma_{out}|^2)}{|S_{21}|(1 - |\Gamma_s|^2)} \quad (1.27)$$

here  $G_{12}$  is the available power gain of the matching network,  $Z_{pre}$  is the input impedance of the preamplifier and  $A_I$  is the current gain in equation (1.23) for the individual matching network [56]. The relation to the coil/matching/preamplifier system for impedances  $Z_{out}$ ,  $Z_{coil}$ ,  $Z_{in}$  and reflection coefficients  $\Gamma_{out}$ ,  $\Gamma_s$ ,  $\Gamma_{out}$  are shown in Figure 1.2. The S-parameters  $S_{11}$  and  $S_{21}$  are those of the matching network.  $R_{in}$  and  $R_{coil}$  are the real parts of  $Z_{in}$  and  $Z_{coil}$ . For only the diagonal of the noise covariance to increase it must be assumed that noise from the matching circuits is not transferred between coils, which is reasonable for coils decoupled using preamplifiers or other methods. The diagonal of the covariance matrix is also multiplied by the noise factor of the preamplifiers, which is given by

$$F_{pre} = 10^{\frac{1}{10}(NF_{min} + \frac{R_N}{G_S}|Y_S - Y_{opt}|^2)}, \quad (1.28)$$

where  $Y_S = G_S + iB_S$  is the admittance presented to the preamplifier input, and the remaining terms in the parentheses are the noise parameters of the preamplifier:  $NF_{min}$ , minimum noise figure,  $R_N$ , correlation resistance, and  $Y_{opt}$ , optimum input admittance [56].

## 1.6 Approaching Ultimate SNR

In MRI, it is desirable for most of the noise from the receive coils to originate from the object being imaged. The intrinsic signal-to-noise ratio (iSNR) is the comparison of the NMR signal received to the noise produced by circulating eddy-currents in the imaging volume [57]. Since this noise source is unavoidable the iSNR is a measure of the theoretical maximum obtainable SNR for a given receiver coil or array with no other sources of noise (i.e., preamplifier noise, coil conductor losses).

The final goal of array design is to approach the ultimate intrinsic Signal to Noise Ratio (uiSNR) [58, 59] and the upper bound, or optimal, parallel imaging performance [60, 61]. In the description of the uiSNR, each hypothetical coil in the array produces a  $B_1$  field distribution, or basis function, that is a solution of Maxwell's equations with the given boundary conditions and excitation at that coil

only. As in other mathematical vector spaces, the basis functions can be combined linearly to produce field distributions that span a sub-space of the solutions of Maxwell's equations. If *all* possible solutions of Maxwell's equations can be described in this manner then the basis spans the whole solution space and the basis is said to be *complete*. In most EM problems a basis with a finite number of elements cannot be complete, but an infinite number of elements is not always sufficient to ensure completeness. For example, uniform plane waves [60, 61] lack evanescent components that are necessary for a full multipole expansion of the electromagnetic field. Similarly, if elementary  $B_1$  dipole sources are restricted to be normal to the surface of the VOI (corresponding to infinitesimal surface coil loops parallel to the surface), even an infinite number of such elements will not lead to a complete basis [62]. High-density coil arrays with 32-128 channels have been developed to approach these limits [37, 59], which are easier to achieve in the middle of the body than at the periphery.

## 1.7 Measurement Techniques

The characterization of coils on the bench is important for validating their quality and safety. A vector network analyzer (VNA) is a measurement instrument that measures the network parameters from the phase and magnitude of reflected and transmitted power relative to a variable frequency source. For measuring the impedance matrix between coils measurements with a VNA is necessary, while for most simple tests of the coils resonant frequency and self-resistance measurement of the Q-factor is an easier and sometimes more reliable test.

### 1.7.1. VNA measurement of impedances

Direct measurements of the S-parameters are performed on a VNA following a full two-port Short-Open-Load-Thru (SOLT) calibration that accounts for cable losses and phase shifts [63, 64]. Cables are attached to SMA-type RF connectors soldered across the port locations on the coils. Two-port Z-matrices are calculated from the measured S-parameters using standard conversion formulas [56]

## 1.7.2. Q factor measurement

Using two small sniffer loop probes attached to the ports of the VNA the coil loop can be excited by one loop, which then inductively excites the second loop. The highest transmitted power will occur at the resonant frequency of the coil and the 3dB bandwidth of  $S_{21}$  measured using the VNA has a simple relation to the  $Q$ , for a simple resonant loop not yet connected to preamplifier, given by

$$Q = \frac{\omega L_{coil}}{R_{coil}} = \frac{f_0}{B_{3dB}} \quad (1.29)$$

where  $B_{3dB}$  is the 3dB bandwidth and  $f_0$  is the center frequency [10]. The  $Q$  differs when the coil is loaded versus unloaded, primarily due to the difference in  $R_{coil}$ , and the ratio of the two is an important indication of coil sensitivity [10].

## 1.7.3. Preamplifier Decoupling and Coil Detuning

Preamplifier decoupling is a standard method, along with geometric decoupling, for reducing signal and noise crosstalk between coils [44]. By introducing a large impedance at the coil ports the currents are reduced on the coils, while the received voltage/signal is still sampled, amplified and acquired.

The preamplifier decoupling effectiveness is measured by the change in  $S_{21}$  between two decoupled loop probes near the coil under test when it is terminated in  $Z_0=50 \Omega$  (power match) compared to when it is connected to the low input impedance preamplifier (noise match) [44, 65]. The coil current, and therefore coupling measured by the loop probes, is proportional to the loop impedance which changes according to

$$20 \log \frac{|Z_{coil} + Z_{block}|}{|Z_{coil} + Z_{power}|} \quad (1.30)$$

where  $Z_{block}$  is  $Z_{out}$  provided at the coil terminals by the balun when it is connected to  $Z_{pre}$ , and  $Z_{power}$  is the impedance provided when it is terminated in  $Z_0$ . Detuning effectiveness is measured similarly to decoupling as the difference in  $S_{21}$  between forward and reverse bias in the PIN diodes (in detuning traps shown in Figure 1.2) with the preamplifier connected.

If the current is significantly reduced than the coupling between coils is removed and there is little noise and signal transferred between the coils. The voltage induced on the coupled coils is proportional to current on the coils. This can be more clearly seen in the impedance matrix  $\tilde{\mathbf{Z}}$  of equation (1.23) which is nearly diagonal when the blocking impedance seen at each of the coil ports is large, indicating no noise transfer.

## 1.8 Thesis Summary

This thesis consists of five chapters. In Chapter 2, expanding on previous work [66], we present a general strategy for modeling stray capacitive coupling using lumped and distributed models leading to simple equivalent circuits. Firstly, the circuit models for a two-coil array are presented and expressions for the two-port impedance parameters are obtained. Capacitive coupling is then studied by simulation as a function of substrate permittivity, coil strip width, substrate thickness and Larmor frequency. The models are validated by fitting the simulated data. Two- and four-coil arrays are constructed and performance is compared in terms of image quality in three coupling situations: zero mutual reactance, zero mutual impedance (both mutual resistance and reactance reduced to negligible levels) and no decoupling (no additional decoupling capacitors added).

A composite coil consists of a surface coil and two coils orthogonal to the surface, termed “upright coils.” Chapter 3 includes a comparison and analysis of upright coils and an 8-coil composite coil array. The comparison validates that upright coils combined with surface result in SNR and parallel imaging improvements at 3T. The optimal upright coil height is determined and since both parallel and standard imaging performance is affected by resistive and inductive coupling [14, 33], the coupling and correlation were evaluated between all coil pairs by simulation and measurement. The potential of using upright coils in quadrature with surface coils and the difference between RSS and optimum reconstruction are also examined.

In Chapter 4 the comparison between a three-element surface coil array that has been decoupled with the method developed in Chapter 2 (mutual resistance and reactance removed between elements) is compared to a naturally decoupled

composite coil array. The comparison between composite and surface coil arrays is extended to simulations of 18-, 36- and 54-coil element arrays that cover the surface of a sphere. The SNR of these arrays is compared along with the uiSNR calculated analytically at 128MHz and 300MHz. The effect of realistic noise from matching networks and preamplifiers is also included. The result of both the 3-element array measurements and larger array simulations is that the composite arrays provides higher SNR farther into the body or phantom, but the surface-array still provides higher SNR near the periphery and the inclusion of noise enhances this difference. In addition, the composite coil arrays are found to be less susceptible to the impact of noise from preamplifiers and matching networks.

## Bibliography

- [1] R. M. Henkelman, G. J. Stanisz and S. J. Graham, "Magnetization transfer in MRI: a review," *NMR Biomed.*, vol. 14, pp. 57-64, 2001.
- [2] P. Gatehouse, J. Keegan, L. Crowe, S. Masood, R. Mohiaddin, K. Kreitner and D. Firmin, "Applications of phase-contrast flow and velocity imaging in cardiovascular MRI," *Eur. Radiol.*, vol. 15, pp. 2172-2184, 10/01, 2005.
- [3] S. Ogawa, R. S. Menon, D. W. Tank, S. G. Kim, H. Merkle, J. M. Ellermann and K. Ugurbil, "Functional brain mapping by blood oxygenation level-dependent contrast magnetic resonance imaging. A comparison of signal characteristics with a biophysical model," *Biophys. J.*, vol. 64, pp. 803-812, 3, 1993.
- [4] C. Burtea, S. Laurent, L. Elst and R. Muller, "Contrast agents: Magnetic resonance," in , W. Semmler and M. Schwaiger, Eds. Springer Berlin Heidelberg, 2008, pp. 135-165.
- [5] M. A. Ohliger, R. L. Greenman, R. Giaquinto, C. A. McKenzie, G. Wiggins and D. K. Sodickson, "Concentric coil arrays for parallel MRI," *Magn. Reson. Med.*, vol. 54, pp. 1248-1260, 2005.
- [6] R. F. Lee, C. J. Hardy, D. K. Sodickson and P. A. Bottomley, "Lumped-element planar strip array (LPSA) for parallel MRI," *Magn. Reson. Med.*, vol. 51, pp. 172-183, 2004.
- [7] A. Kumar and P. A. Bottomley, "Optimizing the intrinsic signal-to-noise ratio of MRI strip detectors," *Magn. Reson. Med.*, vol. 56, pp. 157-166, 2006.
- [8] A. Kumar and P. Bottomley, "Optimized quadrature surface coil designs," *Magnetic Resonance Materials in Physics, Biology and Medicine*, vol. 21, pp. 41-52, 2008.

- [9] C. D. Constantinides, E. Atalar and E. R. McVeigh, "Signal-to-noise measurements in magnitude images from NMR phased arrays," *Magnetic Resonance in Medicine*, vol. 38, pp. 852-857, 1997.
- [10] A. Kumar, W. A. Edelstein and P. A. Bottomley, "Noise figure limits for circular loop MR coils," *Magn. Reson. Med.*, vol. 61, pp. 1201-1209, 2009.
- [11] R. G. Pinkerton, E. A. Barberi and R. S. Menon, "Noise properties of a NMR transceiver coil array," *Journal of Magnetic Resonance*, vol. 171, pp. 151-156, 11, 2004.
- [12] D. K. Sodickson, M. A. Ohliger, R. Lattanzi and G. C. Wiggins, "Coil array design for parallel imaging: Theory and applications," in *Encyclopedia of Magnetic Resonance* Anonymous 2011, .
- [13] D. Larkman, "The g-factor and coil design," in , S. Schoenberg, O. Dietrich and M. Reiser, Eds. Springer Berlin Heidelberg, 2007, pp. 37-48.
- [14] M. A. Ohliger, P. Ledden, C. A. McKenzie and D. K. Sodickson, "Effects of inductive coupling on parallel MR image reconstructions," *Magn. Reson. Med.*, vol. 52, pp. 628-639, 2004.
- [15] I. Rabi, S. Millman, P. Kusch and J. Zacharias, "The Molecular Beam Resonance Method for Measuring Nuclear Magnetic Moments," *Phys. Rev.*, vol. 53, pp. 318, 1938.
- [16] E. M. Purcell, H. C. Torrey and R. V. Pound, "Resonance Absorption by Nuclear Magnetic Moments in a Solid," *Phys. Rev.*, vol. 69, pp. 37-38, 01/01, 1946.
- [17] F. Bloch, W. Hansen and M. Packard, "The nuclear induction experiment," *Physical Review*, vol. 70, pp. 474-485, 1946.
- [18] A. Kumar, D. Welti and R. R. Ernst, "NMR Fourier zeugmatography," *Journal of Magnetic Resonance (1969)*, vol. 18, pp. 69-83, 4, 1975.
- [19] K. Wüthrich, "Protein structure determination in solution by NMR spectroscopy." *J. Biol. Chem.*, vol. 265, pp. 22059-22062, 1990.
- [20] P. Mansfield, "Multi-planar image formation using NMR spin echoes," *Journal of Physics C: Solid State Physics*, vol. 10, pp. L55, 1977.
- [21] P. C. Lauterbur, "Image formation by induced local interactions: examples employing nuclear magnetic resonance," *Nature*, vol. 242, pp. 190-191, 1973.
- [22] Z. Liang and P. Lauterbur, *Principles of Magnetic Resonance Imaging: A Signal Processing Perspective*. Wiley-IEEE Press, 2000.
- [23] P. V. Prasad, *Magnetic Resonance Imaging: Methods and Biologic Applications*. Totowa, N.J.: Humana Press, 2006.
- [24] F. Wiesinger, P. Van de Moortele, G. Adriany, N. De Zanche, K. Ugurbil and K. P. Pruessmann, "Potential and feasibility of parallel MRI at high field " *NMR Biomed.*, vol. 19, pp. 368-378, 2006.

- [25] M. Shinnar, S. Eleff, H. Subramanian and J. S. Leigh, "The synthesis of pulse sequences yielding arbitrary magnetization vectors," *Magn. Reson. Med.*, vol. 12, pp. 74-80, 1989.
- [26] P. J. Basser, J. Mattiello and D. LeBihan, "MR diffusion tensor spectroscopy and imaging," *Biophys. J.*, vol. 66, pp. 259-267, 1, 1994.
- [27] J. Mispelter, M. Lupu and A. Briguet, *NMR Probeheads for Biophysical and Biomedical Experiments*. London: Imperial College Press, 2006.
- [28] T. S. Ibrahim, R. Lee, B. A. Baertlein, A. M. Abduljalil, H. Zhu and P. L. Robitaille, "Effect of RF coil excitation on field inhomogeneity at ultra high fields: a field optimized TEM resonator," *Magn. Reson. Imaging*, vol. 19, pp. 1339-1347, 12/01, 2001.
- [29] K. M. Gilbert, A. T. Curtis, J. S. Gati, L. Martyn Klassen, L. E. Villemaire and R. S. Menon, "Transmit/receive radiofrequency coil with individually shielded elements," *Magn. Reson. Med.*, vol. 64, pp. 1640-1651, 2010.
- [30] K. N. Kurpad, S. M. Wright and E. B. Boskamp, "RF current element design for independent control of current amplitude and phase in transmit phased arrays" *Concepts Magn. Reson.*, vol. 29B, pp. 75-83, 2006.
- [31] J. S. Hyde, A. Jesmanowicz, W. Froncisz, J. Bruce Kneeland, T. M. Grist and N. F. Campagna, "Parallel image acquisition from noninteracting local coils," *Journal of Magnetic Resonance*, vol. 70, pp. 512-517, 1986.
- [32] E. B. Boskamp, "A new Revolution in Surface Coil Technology: the Array Surface Coil," *SMRM 6th Annual Meeting*, pp. 405, 1987.
- [33] P. B. Roemer, W. A. Edelstein, C. E. Hayes, S. P. Souza and O. M. Mueller, "The NMR phased array," *Magn. Reson. Med.*, vol. 16, pp. 192-225, 1990.
- [34] K. P. Pruessmann, M. Weiger, M. B. Scheidegger and P. Boesiger, "SENSE: Sensitivity encoding for fast MRI," *Magn. Reson. Med.*, vol. 42, pp. 952-962, 1999.
- [35] D. K. Sodickson and W. J. Manning, "Simultaneous acquisition of spatial harmonics (SMASH): Fast imaging with radiofrequency coil arrays," *Magn. Reson. Med.*, vol. 38, pp. 591-603, 1997.
- [36] M. A. Griswold, P. M. Jakob, R. M. Heidemann, M. Nittka, V. Jellus, J. Wang, B. Kiefer and A. Haase, "Generalized autocalibrating partially parallel acquisitions (GRAPPA)," *Magn. Reson. Med.*, vol. 47, pp. 1202-1210, 2002.
- [37] G. C. Wiggins, J. R. Polimeni, A. Potthast, M. Schmitt, V. Alagappan and L. L. Wald, "96-Channel receive-only head coil for 3 Tesla: Design optimization and evaluation," *Magn. Reson. Med.*, vol. 62, pp. 754-762, 2009.
- [38] W. A. Edelstein, C. J. Hardy and O. M. Mueller, "Electronic decoupling of surface-coil receivers for NMR imaging and spectroscopy," *Journal of Magnetic Resonance*, vol. 67, pp. 156-161, 1986.

- [39] C. C. Guclu, "Effect of body coil electric field distribution on receive-only surface coil heating," *Journal of Magnetic Resonance Imaging*, vol. 14, pp. 484-487, 2001.
- [40] N. De Zanche, A. M. Maunder, T. Charlton, K. Wachowicz and B. G. Fallone, "A Unified Framework for SNR Comparisons of Four Array Image Combination Methods," *Proc. Intl. Soc. Mag. Reson. Med.*, vol. 19, pp. 4659, 2011.
- [41] C. E. Hayes and P. B. Roemer, "Noise correlations in data simultaneously acquired from multiple surface coil arrays," *Magn. Reson. Med.*, vol. 16, pp. 181-191, 1990.
- [42] D. O. Walsh, A. F. Gmitro and M. W. Marcellin, "Adaptive reconstruction of phased array MR imagery," *Magn. Reson. Med.*, vol. 43, pp. 682-690, 2000.
- [43] D. Erdogmus, E. G. Larsson, R. Yan, J. C. Principe and J. R. Fitzsimmons, "Asymptotic SNR-performance of some image combination techniques for phased-array MRI," *Signal Process*, vol. 84, pp. 997-1003, 2004.
- [44] A. Reykowski, S. M. Wright and J. R. Porter, "Design of Matching Networks for Low Noise Preamplifiers," *Magn. Reson. Med.*, vol. 33, pp. 848-852, 1995.
- [45] G. R. Duensing, H. R. Brooker and J. R. Fitzsimmons, "Maximizing Signal-to-Noise Ratio in the Presence of Coil Coupling," *Journal of Magnetic Resonance, Series B*, vol. 111, pp. 230-235, 6, 1996.
- [46] M. A. Ohliger and D. K. Sodickson, "An introduction to coil array design for parallel MRI" *NMR Biomed.*, vol. 19, pp. 300-315, 2006.
- [47] T. W. Redpath, "Noise correlation in multicoil receiver systems" *Magn. Reson. Med.*, vol. 24, pp. 85-89, 1992.
- [48] X. Zhang and A. Webb, "Design of a capacitively decoupled transmit/receive NMR phased array for high field microscopy at 14.1 T," *Journal of Magnetic Resonance*, vol. 170, pp. 149-155, 9, 2004.
- [49] C. von Morze, J. Tropp, S. Banerjee, D. Xu, K. Karpodinis, L. Carvajal, C. P. Hess, P. Mukherjee, S. Majumdar and D. B. Vigneron, "An eight-channel, nonoverlapping phased array coil with capacitive decoupling for parallel MRI at 3 T," *Concepts Magn. Reson.*, vol. 31B, pp. 37-43, 2007.
- [50] B. Wu, P. Qu, C. Wang, J. Yuan and G. X. Shen, "InterconnectingL/C components for decoupling and its application to low-field open MRI array" *Concepts Magn. Reson.*, vol. 31B, pp. 116-126, 2007.
- [51] R. F. Lee, R. O. Giaquinto and C. J. Hardy, "Coupling and decoupling theory and its application to the MRI phased array" *Magn. Reson. Med.*, vol. 48, pp. 203-213, 2002.
- [52] Y. Li, Z. Xie, Y. Pang, D. Vigneron and X. Zhang, "ICE decoupling technique for RF coil array designs" *Med. Phys.*, vol. 38, pp. 4086, 2011.

- [53] P. J. Cassidy, K. Clarke and D. J. Edwards, "Determining the tuning and matching requirements of RF coils using electromagnetic simulation and electric circuit analysis " *Concepts Magn. Reson.*, vol. 25B, pp. 27-41, 2005.
- [54] R. Brown and Y. Wang, "Transmission line effects on the coil noise correlation matrix in MRI " *Conf. Proc. IEEE Eng. Med. Biol. Soc.*, pp. 2032-2035, 2008.
- [55] S. M. Wright and L. L. Wald, "Theory and application of array coils in MR spectroscopy," *NMR Biomed.*, vol. 10, pp. 394-410, 1997.
- [56] D. M. Pozar, *Microwave Engineering*, 3rd. Danvers, MA: John Wiley & Sons, Ltd, 2005.
- [57] W. A. Edelstein, G. H. Glover, C. J. Hardy and R. W. Redington, "The intrinsic signal-to-noise ratio in NMR imaging," *Magn. Reson. Med.*, vol. 3, pp. 604-618, 1986.
- [58] O. Ocali and E. Atalar, "Ultimate intrinsic signal-to-noise ratio in MRI " *Magn. Reson. Med.*, vol. 39, pp. 462-473, 1998.
- [59] F. Wiesinger, N. DeZanche and K. Pruessman, "Approaching Ultimate SNR with Finite Coil Arrays," *Proc. Intl. Soc. Mag. Reson. Med.*, vol. 13, pp. 627, 2005.
- [60] M. A. Ohliger, A. K. Grant and D. K. Sodickson, "Ultimate intrinsic signal-to-noise ratio for parallel MRI: Electromagnetic field considerations," *Magn. Reson. Med.*, vol. 50, pp. 1018-1030, 2003.
- [61] F. Wiesinger, P. Boesiger and K. P. Pruessmann, "Electrodynamics and ultimate SNR in parallel MR imaging," *Magn. Reson. Med.*, vol. 52, pp. 376-390, 2004.
- [62] W. Zhiyue J., "Towards a complete coil array," *Magn. Reson. Imaging*, vol. 26, pp. 1310-1315, 2008.
- [63] A. Ferrero, U. Pisani and K. J. Kerwin, "A new implementation of a multiport automatic network analyzer," *Microwave Theory and Techniques, IEEE Transactions on*, vol. 40, pp. 2078-2085, 1992.
- [64] H. Heuermann, "GSOLT: the calibration procedure for all multi-port vector network analyzers," *Microwave Symposium Digest*, vol. 3, pp. 1815-1818, 2003.
- [65] B. Keil, G. C. Wiggins, C. Triantafyllou, L. L. Wald, F. M. Meise, L. M. Schreiber, K. J. Klose and J. T. Heverhagen, "A 20-channel receive-only mouse array coil for a 3 T clinical MRI system," *Magn. Reson. Med.*, vol. 66, pp. 582-593, 2011.
- [66] A. M. Mauder, M. Daneshmand, P. Mousavi, B. G. Fallone and N. De Zanche, "Parasitic capacitance in MRI coil arrays: Models and application to Array decoupling," in *Microwave Symposium Digest (MTT), 2013 IEEE MTT-S International*, 2013, .

## Chapter 2

# Stray Capacitance between MRI Coil Elements: Models and Application to Array Decoupling

### 2.1. Introduction

Stray (unintentional) mutual capacitance has largely been ignored in the literature, even though its effects are no longer negligible now that numerous 300 MHz (7T) and some 400 MHz (9.4T) [1] scanners are available in research centers. A number of systems between 435MHz (10.5T) [2] and 500MHz (11.7T) [3] are also being installed. Some of the challenges of designing coil arrays at higher frequencies may be overcome with a better theoretical understanding of capacitive coupling. However, quantitative models of stray capacitive coupling in MRI coil arrays do not exist even though its effects can be observed on coil tuning, matching, and overall coupling.

In this chapter the mutual resistance is shown be eliminated with capacitive coupling as an alternative to using specific geometrical coil configurations [4] or hardware combination after amplification [5]. Similar results using additional circuits with negligible losses [6] have been shown recently. The impact of noise correlation in image combination has been investigated in detail [7, 8], and we note that ignoring noise correlation in image combination can result in SNR losses greater than 20% [9]. In arrays with large noise correlations ( $>0.3$ ) between adjacent elements [10] it is important to reduce or remove mutual resistance since in this situation reaching the optimum preamplifier noise figure can be impossible with standard uncoupled matching networks [11] resulting in sub-optimal combined image SNR. Removing mutual resistance also benefits transceive arrays [12] where amplifier decoupling [13, 14] in transmission is much more difficult to achieve than in reception.

First, the circuit models for a two-coil array are presented and expressions for the two-port impedance parameters are obtained. Capacitive coupling is then studied by simulation as a function of substrate permittivity, coil strip width,

substrate thickness and Larmor frequency. The models are validated by fitting the model parameters to the simulated data and comparing the resulting prediction by the model of impedances to the simulation and the fitted parameters to quasistatic predictions. Two- and four-coil arrays are constructed and performance is compared in terms of image quality in three coupling situations: zero mutual reactance, zero mutual impedance (both mutual resistance and reactance reduced to negligible levels) and no decoupling (no additional decoupling capacitors added).

## 2.2. Capacitive Coupling Models

The following analysis relies on the assumption that capacitive coupling between adjacent coils is dominated by the closest conductive portions of the coils, denoted 1'' and 2'' in Figure 1.4 a. Lumped and distributed circuit models are presented in Figure 1.4 b and c.

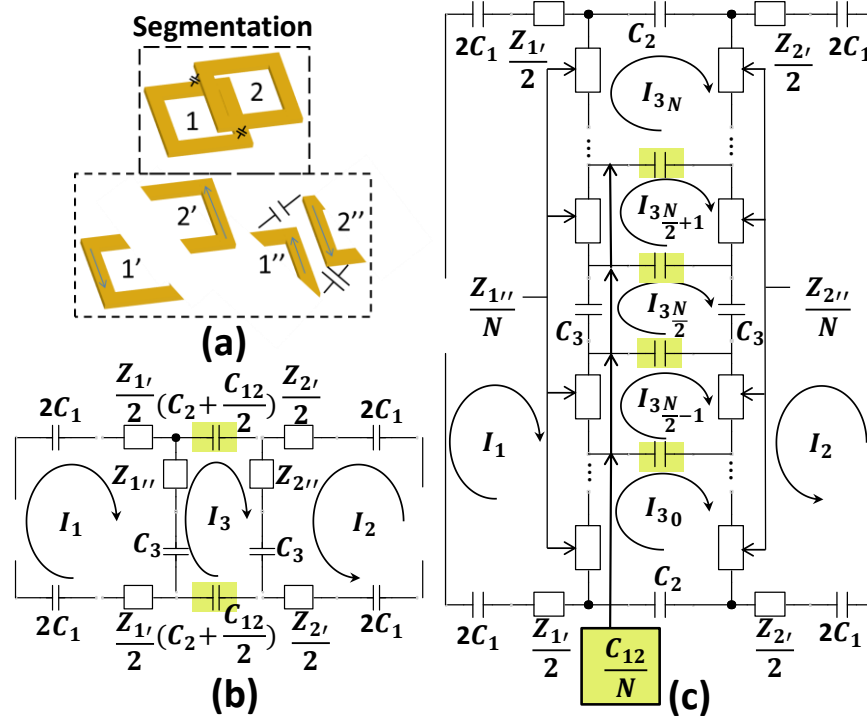


Figure 1.4: Models for representing capacitive coupling between two coils. (a) Segmentation of coils into sections affected by stray capacitance (') and sections that are not (''). (b) Lumped capacitance circuit model. (c) Distributed capacitance model.

In both the lumped and distributed models there are meshes without signal ports. The two-port impedance elements are defined as

$$Z_{mn}^{two-port} = \left. \frac{\mathbf{V}_m}{\mathbf{I}_n} \right|_{I_{k \neq n}=0}, \quad (1.31)$$

where  $m, n, k \in \{1, 2\}$ . equation (1.31) must be derived from the complete impedance matrix equation

$$\mathbf{ZI} = \begin{bmatrix} Z_{11} & Z_{12} & -\mathbf{Z}_{31}^T \\ Z_{21} & Z_{22} & \mathbf{Z}_{32}^T \\ -\mathbf{Z}_{31} & \mathbf{Z}_{32} & \mathbf{Z}_{33} \end{bmatrix} \begin{bmatrix} I_1 \\ I_2 \\ I_3 \end{bmatrix} = \begin{bmatrix} V_1 \\ V_2 \\ 0 \end{bmatrix}. \quad (1.32)$$

where  $Z_{11}$ ,  $Z_{12}$  and  $Z_{22}$  are the self and mutual impedances in absence of capacitive coupling,  $\mathbf{Z}_{3n}$  is a column vector containing the mutual impedances between the meshes without ports and coil  $n$ , and  $\mathbf{Z}_{33}$  is the impedance matrix of those meshes.  $\mathbf{Z}_{31}$  is negative because the current convention of Figure 1.4 shows  $I_1$  directed opposite the mesh currents and  $I_2$  directed with them. Using the definition in equation (1.31), solving for  $\mathbf{Z}_{mn}^{two-port}$  requires solving equation 2.2 for  $I_n$  and  $\mathbf{I}_3$  with  $I_{k \neq n} = 0$ , which is equivalent to solving,

$$\begin{bmatrix} I_n \\ \mathbf{I}_3 \end{bmatrix} = \begin{bmatrix} Z_{nn} & (-1)^n \mathbf{Z}_{3n}^T \\ (-1)^n \mathbf{Z}_{3n} & \mathbf{Z}_{33} \end{bmatrix}^{-1} \begin{bmatrix} V_n \\ 0 \end{bmatrix}. \quad (1.33)$$

Where the elements of the matrix  $Z_{mn}^{two-port}$  are then found as

$$Z_{mn}^{two-port} = Z_{mn} + \left. \frac{(-1)^n \mathbf{Z}_{3m}^T \mathbf{I}_3}{I_n} \right|_{I_{k \neq n}=0} \quad (1.34)$$

### 2.2.1. Lumped Model

The lumped approximation shown in Figure 1.4b concentrates the stray capacitance at the ends of the coupled portions of the coils (1" and 2"). In this case  $\mathbf{Z}_{3n}$  and  $\mathbf{Z}_{33}$  are scalars labeled "lump", which are expressed in terms of the impedances of the segmented sections.

$$\begin{aligned}
Z_{3n}^{lump} &= Z_{Line}^n + Z_{coup}^n - j \frac{1}{\omega C_3} \\
Z_{33}^{lump} &= Z_{Line}^1 + Z_{Line}^2 - \frac{2j}{\omega} \left( \frac{C_3(C_2 + C_{12}/2)}{C_3 + (C_2 + C_{12}/2)} \right). \\
Z_{Line}^n &= Z_{n''} + Z_{n''k''} \\
Z_{coup}^n &= Z_{n'k''} + Z_{n'n''}
\end{aligned} \tag{1.35}$$

where  $k, n \in \{1,2\}, k \neq n$ . The impedances  $Z_{Line}^n$ ,  $Z_{coup}^n$ ,  $Z_{11}, Z_{12}, Z_{22}$ , and stray capacitance  $C_{12}$  are the model's parameters that need to be determined.  $Z_{Line}^n$  is the impedance of the capacitively coupled section of coil  $n$ ,  $Z_{coup}^n$  is the mutual impedance between the capacitive coupling mesh and uncoupled portion of coil  $n$ . Using equations (2.1-2.4) to find

$$I_3/I_n|_{I_{k \neq n}=0} = (-1)^{n+1} Z_{3n}^{lump} / Z_{33}^{lump}, \tag{1.36}$$

the two-port impedance matrix then simplifies to

$$Z_{two-port}^{lump} = \begin{bmatrix} Z_{11} - \frac{Z_{31}^{lump}}{Z_{33}} & Z_{12} + \frac{Z_{31}^{lump} Z_{32}^{lump}}{Z_{33}} \\ Z_{21} + \frac{Z_{31}^{lump} Z_{32}^{lump}}{Z_{33}} & Z_{22} - \frac{Z_{32}^{lump}}{Z_{33}} \end{bmatrix}. \tag{1.37}$$

This result shows that for symmetric coils where  $Z_{32} = Z_{31}$  the change in self and mutual impedance due to capacitive coupling will be equal in magnitude and opposite in sign. Mutual impedance between coils is completely removed as predicted using the lumped model when  $Z_{21} = -Z_{32}Z_{31}/Z_{33}$ .

## 2.2.2. Distributed Model

In the distributed model the impedances of the coupled sections are distributed uniformly over the length which is split into an odd number of  $(N+1)$  segments. The elements of the matrix in equation (1.33) are given as follows.  $\mathbf{Z}_{3n}^{dist}$  is an  $(N+1)$  size vector with elements given by

$$\mathbf{Z}_{3n}^{dist} (i) = (Z_{Line}^n + Z_{coup}^n)/N, \tag{1.38}$$

and  $\mathbf{Z}_{33}^{dist}$  is tri-diagonal matrix with elements given by

$$\begin{aligned}
\mathbf{Z}_{33}^{dist} (i,i) &= -2Nj/(\omega C_{12}) + (Z_{Line}^1 + Z_{Line}^2)/N \\
\mathbf{Z}_{33}^{dist} (i,j=i\pm 1) &= Nj/(\omega C_{12})
\end{aligned} \tag{1.39}$$

when  $i = 2 \dots N$ . For the end meshes including  $C_2$  and center mesh with  $C_3$  the matrix elements are

$$\begin{aligned}\mathbf{Z}_{33}^{dist}(i,i) \Big|_{i=1,N+1} &= \frac{-NC_2C_{12}j}{\omega(C_2 + C_{12})} + \frac{Z_{Line}^1 + Z_{Line}^2}{N} \\ \mathbf{Z}_{33}^{dist}(i,i) \Big|_{i=N/2+1} &= -2Nj/(\omega C_{12}) - 2Nj/(\omega C_3). \\ \mathbf{Z}_{3n}^{dist}(i) \Big|_{i=N/2+1} &= -j/(\omega C_3)\end{aligned}\quad (1.40)$$

The two-port impedance matrix  $\mathbf{Z}_{dist}^{two-port}$  of the distributed model is a  $2 \times 2$  matrix like equation (1.37), with elements found using equation (1.33) and equation (1.34).

## 2.3. Methods

The circuit models above are validated by measurements of coupling and mutual impedance using simulated and experimental arrays. The resulting image SNRs and geometry factors are also calculated for experimental arrays.

### 2.3.1. Simulations

The impedance ( $Z$ ) parameters between the ports of simulated coils (Figure 1.5a) were obtained in HFSS (Ansys Corp., USA) using the driven modal solution at four different Larmor frequencies (64 MHz, 128 MHz, 200 MHz, and 300 MHz). Meshing was performed using second-order basis functions and four adaptive passes. Repeated simulations resulted in the same impedance parameters to an accuracy of three digits. The two coils shown in Figure 1.5a are modeled as copper traces with a thickness of 40  $\mu\text{m}$  on a 7 mm insulating substrate over a large ( $60 \times 60 \times 11 \text{ cm}^3$ ) lossy dielectric phantom ( $\epsilon_r = 76$ ,  $\sigma = 0.8 \text{ S/m}$ ). A radiating boundary is applied to the surrounding ( $60 \times 60 \times 70 \text{ cm}^3$ ) vacuum. Lumped ports with  $50 \Omega$  termination are used at locations P1 and P2. The effect of variations in design parameters (substrate thickness  $t$ , coil spacing  $s$ , coil diameter  $d$ , strip width  $w$  and substrate permittivity  $\epsilon_r$ ) are also investigated by varying one parameter at a time while the rest are kept constant at the following standard values:  $t = 7 \text{ mm}$ ,  $s = 2 \text{ mm}$ ,  $w = 9.5 \text{ mm}$ ,  $d = 70 \text{ mm}$  and  $\epsilon_r = 3.4$  for the substrate.

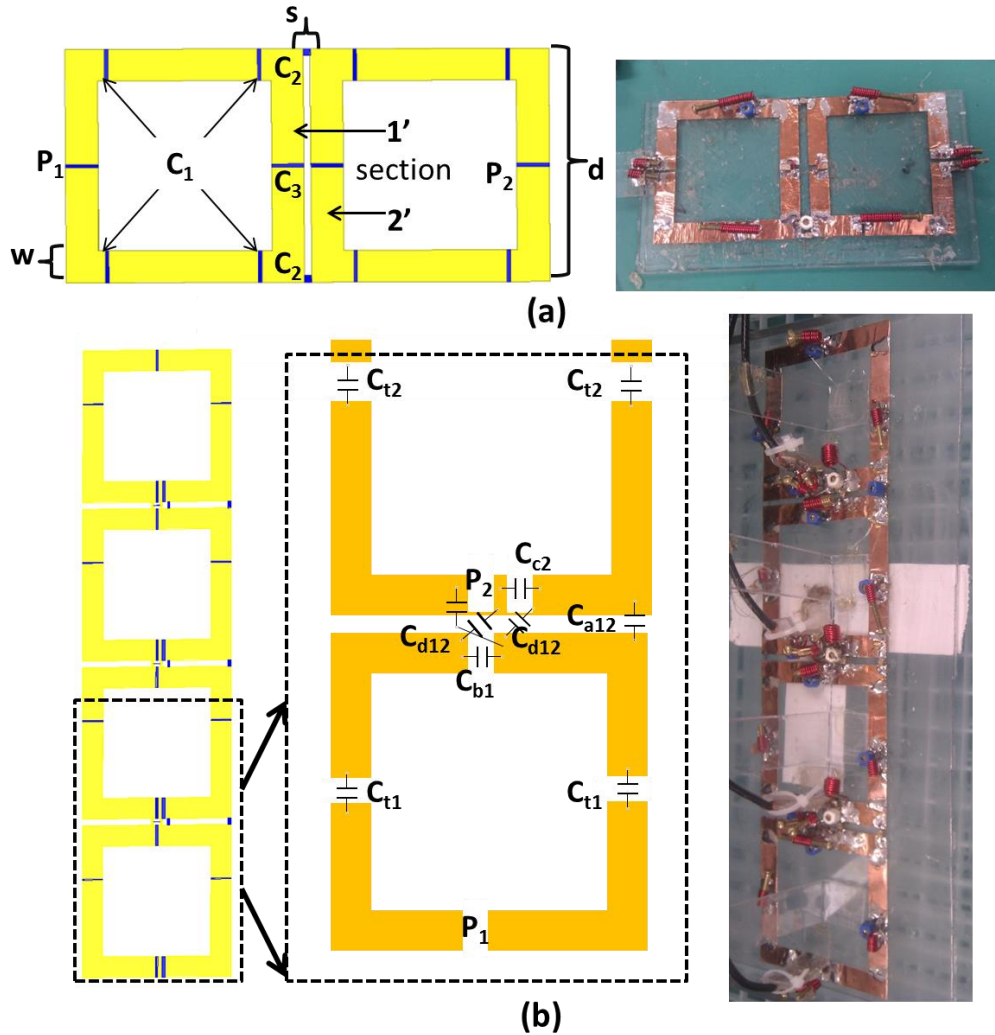


Figure 1.5. (a) Coil geometry used in two-coil array simulations and construction. (b) Geometry used in construction of four-coil array.

The simulations are repeated with all combinations of ten  $C_2$  and four  $C_3$  values (forty points) and the resulting two-port  $Z$  matrices are used to determine the model parameters (stray capacitance  $C_{12}$ ,  $\mathbf{Z}_{Line}^n$ ,  $\mathbf{Z}_{coup}^n$  and  $\mathbf{Z}_{11}$ ,  $\mathbf{Z}_{22}$ ,  $\mathbf{Z}_{21}$ ) by least squares fitting in MATLAB (The MathWorks, USA). The values of  $C_2$  and  $C_3$  shown in Table 1-1 are chosen to provide a wide range of reactance at each frequency, while avoiding resonance between the copper strips (when the reactance of  $\mathbf{Z}_{33}$  in equation (5) becomes zero).

Table 1-1: Capacitors used in two-coil array simulations depicted in Figure 1.5a

Frequency (MHz)	Frequency (MHz)		
	Capacitance (pF)		
	C <sub>1</sub>	C <sub>2</sub>	C <sub>3</sub>
<b>64</b>	280	0, 5.6, 10, 20, 33, 56, 82, 100, 150, 200	100, 200, 450, 900
<b>128</b>	70	0, 5.6, 10, 20, 33, 47, 56, 82, 100, 120	27, 36, 68, 100
<b>200</b>	28	0, 5.6, 10, 15, 20, 27, 33, 39, 56, 68	15, 20, 27, 36
<b>300</b>	12	0, 5.6, 6.8, 10, 15, 20, 27, 33, 39, 47	6.8, 10, 15, 20

The value of C<sub>1</sub> is chosen at each frequency to tune the coils approximately to resonance (zero port reactance) with standard design parameter values. Consequently, with a coil self-inductance of 117nH and values of C<sub>1</sub> in Table 1-1, the C<sub>3</sub> required for resonance is 215 pF, 54 pF, 24 pF and 12 pF for 64MHz, 128MHz, 200MHz and 300 MHz respectively. These are all in the middle range of C<sub>3</sub> shown in Table 1-1.

It is standard practice to distribute the coil tuning capacitance as a series of equal capacitances separated by conductor lengths shorter than  $\lambda/20$  [15] to minimize sensitivity to dielectric loading, and losses by radiation and in the phantom. However, capacitive coupling is strongly dependent on C<sub>3</sub>, the electric field distribution and therefore these losses unavoidably change. Indeed, the value of C<sub>3</sub> directly modifies the terms in equation (2.5) and the tuning capacitor distribution, with consequent effects on the electromagnetic field distribution, impedances and coupling that are independent of capacitive coupling [16]. HFSS simulations of single coils confirmed that the coil inductance and resistance are sensitive to changes in C<sub>3</sub>. In an array the effect of C<sub>3</sub> is more complex since there are magnetically induced eddy currents in the conductor of adjacent coils [17] that increase loss.

We therefore adopted an approach that allows the separation of the effect of C<sub>3</sub> on capacitive coupling from that on inductance, magnetic coupling effects and loss while simulating the full coil array. This is achieved by taking the partial derivative of the two-port impedance matrix in equation (1.37) with respect to C<sub>2</sub>,

$$\frac{\partial \mathbf{Z}_{two-port}^{lumped}}{\partial C_2} = \frac{-2j}{\omega(C_2 + \frac{C_{12}}{2})^2 Z_{33}^2} \begin{bmatrix} -Z_{31}^2 & Z_{32}Z_{31} \\ Z_{32}Z_{31} & -Z_{32}^2 \end{bmatrix}. \quad (1.41)$$

which is independent of  $Z_{11}$ ,  $Z_{22}$  and  $Z_{12}$ . This derivative is approximated using a second-order finite difference formula for non-uniform intervals [18].

The residual for least squares fitting is calculated as the difference between the finite difference values calculated for the predicted and simulated data. The finite difference cannot be calculated at the end values of  $C_2$  resulting in 32 partial derivative values corresponding to the central 8 values of  $C_2$  and four  $C_3$  values. These partial derivative values are used in the fitting routine to solve for  $Z_{line}$ ,  $Z_{coup}$  and  $C_{12}$ .

The remaining model parameters  $Z_{11}$ ,  $Z_{22}$ ,  $Z_{21}$  are subsequently obtained for each value of  $C_3$  by fitting over the ten values of  $C_2$  using the  $Z_{line}$ , and  $Z_{coup}$  and  $C_{12}$  obtained previously.

If  $Z_{11}$  or  $Z_{12}$  in equation (1.32) did change when varying  $C_2$  it is unlikely that the simulated change in  $\mathbf{Z}_{two-port}^{lumped}$  with  $C_2$  would be exactly equal for self and mutual two-port impedances, since most parameters (e.g. series capacitor distribution) affect the two asymmetrically. In this model  $Z_{11}$  and  $Z_{12}$  depend on the resistance and inductance only and capacitive coupling doesn't affect these values.

### 2.3.2. Experimental Arrays

A two-coil array was built for 127.8 MHz with the same dimensions as those simulated (the four  $C_1$  capacitors in Figure 1.5a are combined into two capacitors because the resulting conductor segments are short enough at this frequency to satisfy the  $\lambda/20$  requirement). The standard design parameter values above were used except for a separation  $s = 3$  mm, which allows a wider range of mutual resistance and reactance to be achieved. Three coupling situations are compared:  $(C_2, C_3) = (27, 36)$  pF, giving zero mutual reactance;  $(C_2, C_3) = (68, 300)$  pF, giving zero mutual impedance; and  $(C_2, C_3) = (0, 36)$  pF for no additional capacitive

decoupling (only stray). Each version is tuned by adjusting  $C_1$  and matched to  $50 \Omega$  using a discrete  $\lambda/4$  balun [19], shown in Figure 1.2a, at 127.8 MHz.

A four-coil linear array (Figure 1.5b) was simulated to find the appropriate values of the decoupling capacitors  $C_a$  (10 – 12 pF),  $C_b$  (27-36 pF),  $C_c$  (100 pF), and  $C_d$  (80-100 pF) for the same three situations above (range of values is given when precise value is not critical). The capacitors  $C_b$ ,  $C_c$  and  $C_d$  adjust the mutual reactance, while  $C_a$  removes mutual resistance by driving a current in the mesh between the coils. This scheme allows the spacing to be chosen independently as 3 mm, thus avoiding the excessive 5 mm gap used for the two-coil array that could result in signal loss in that region. Without decoupling  $C_c$  is short circuited and  $C_a$  and  $C_d$  are removed, while  $C_a$  alone are removed for the no mutual reactance case. All decoupling capacitors,  $C_b$ ,  $C_c$ ,  $C_d$  and  $C_a$  are used for the case of no mutual impedance.

Active PIN diode traps are placed on the series capacitors ( $C_1$  and  $C_{t1}$ ) in both arrays to detune the coils during the transmit RF pulses emitted by the system's body coil.

### 2.3.3. Measurements

Coils are connected using  $\lambda/2$  coaxial cables to low-input-impedance preamps (input impedance  $Z_{\text{pre}} = 4.1 \pm 0.4 \Omega$  for the four preamplifiers used avoiding ones with higher  $Z_{\text{pre}}$ , minimum noise figure 0.90 dB) housed within a connector box (Philips Healthcare; Cleveland, OH). Arrays are placed on a  $36 \times 26 \times 11 \text{ cm}^3$  phantom (Figure 1.6) filled with demineralized water and  $3.6 \text{ g/l}$  NaCl and  $1.96 \text{ g/l}$   $\text{CuSO}_4 \cdot 5\text{H}_2\text{O}$  corresponding to the simulated phantom dielectric properties ( $\epsilon_r = 76$ ,  $\sigma = 0.8 \text{ S/m}$ ). Additive white noise is present in each array channel and therefore noise data from scans without RF excitation are used to calculate the noise covariance and correlation coefficients.

Direct measurements of the S-parameters were performed as detailed in section 1.

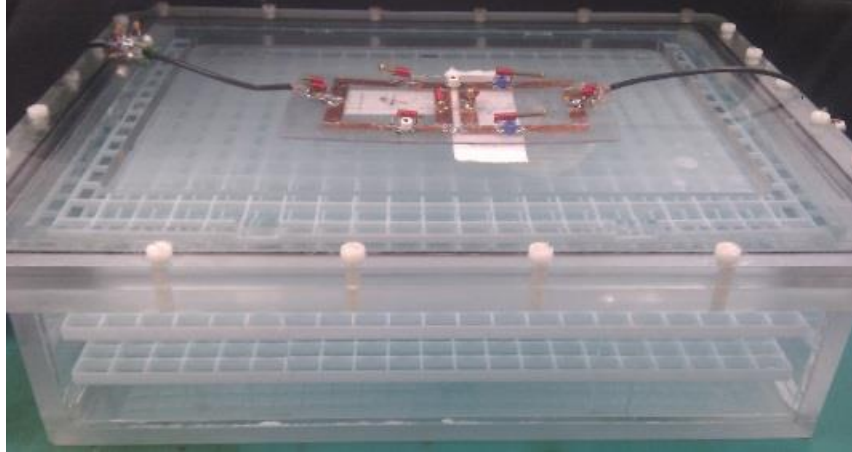


Figure 1.6: Phantom used for measurements with two coil array. Grid planes that provide inside image contrast are visible.

## 2.4. Results

### 2.4.1. Impedance Parameters

The simulated mutual impedances at 128 MHz and 300 MHz were fitted to the distributed and lumped models as shown in Figure 1.7. While both models correctly predict the impedance trends, the distributed model fits the data substantially better than the lumped model and over a larger range of capacitances. These results show that an appropriate choice of  $C_2$  and  $C_3$  allows removal of not only the mutual reactance, but also the mutual resistance (as indicated by the mutual resistance and reactance lines crossing the zero line). Although not shown both can be eliminated approximately at the same time using a higher value of  $C_3$ , but complete mutual elimination is not guaranteed in general and small changes in geometry may be required as well for coils.

Changes in self-impedance are equal and opposite to those displayed for mutual impedance in Figure 1.7. To validate this the average percent difference between the two is calculated as

$$100\% \frac{\left| \frac{\partial Z_{11}}{\partial C_2} - \frac{\partial Z_{21}}{\partial C_2} \right|}{\left| \frac{\partial Z_{11}}{\partial C_2} \right|} \quad (1.42)$$

Using this equation for the real and imaginary components separately the average for all the values at 128MHZ in Figure 1.7 is  $(0.18 \pm 0.36 - j0.22 \pm j0.48)\%$ . Since the standard deviation is double the average the differences can be attributed to the simulation numerical error.

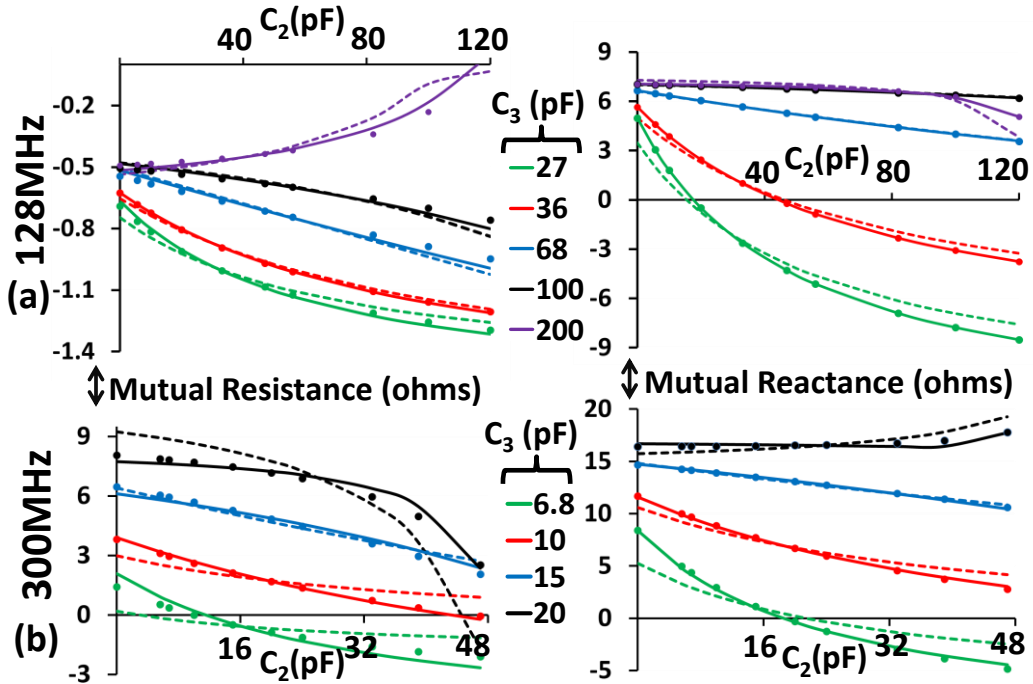


Figure 1.7: Fitting and Simulation results for the 2-port mutual impedance parameters at a) 128 and b) 300 MHz. Dots are simulation results, solid lines prediction using distributed model and dashed lines predictions with the lumped model.

When the third loop formed by the adjacent coil sections and capacitors  $C_2$  approaches resonance both models lose accuracy; however, this region of large  $C_2$  values is of little practical importance and it should be avoided to preserve coil efficiency and well-defined sensitivity patterns.

From Figure 1.7 it appears that mutual impedance between coils can be stabilized against changes in dielectric loading. For example, in Figure 1.7 at 128MHz if the series capacitor  $C_3$  is between 100-200 pF and the parallel capacitor  $C_2$  is less than 40pF there will be little variation in the mutual and self-impedances due to changing stray capacitance. Capacitors are commonly distributed around

coils to lessen the effect of stray capacitance and the results here indicate the importance of this.

Figure 1.8 shows the effect of  $C_3$  on the distributed models' resistive coupling coefficient and mutual inductance with only stray capacitance present ( $C_2 = 0$ ). The change in resistive coupling coefficient, defined in reference [8], is used rather than resistance to display the results at different frequencies on the same plot since the resistance itself increases greatly with frequency. The actual self and mutual resistances and inductances are indicated (arrows) at each frequency for the largest reactance value of  $C_3$ .

By comparing the trends in Figure 1.8 to the stated values of mutual inductances and resistances it is shown that at higher frequencies the stray capacitance becomes significant compared to mutual inductance/resistance, this effect is highly dependent on the series capacitor  $C_3$ ; with larger reactance (smaller  $C_3$ , e.g., required for operation at high frequency) the impact of the stray capacitance is greater. It is interesting to note that capacitive coupling has little effect if the reactance of  $Z_{3n}^{lump}$  in equation (2.5) is close to zero; in Figure 1.8 this is the case for the lower reactance values of  $C_3$ . These results suggest that stray capacitive coupling can be exploited to reduce coupling by adjusting the series capacitance on the coils.

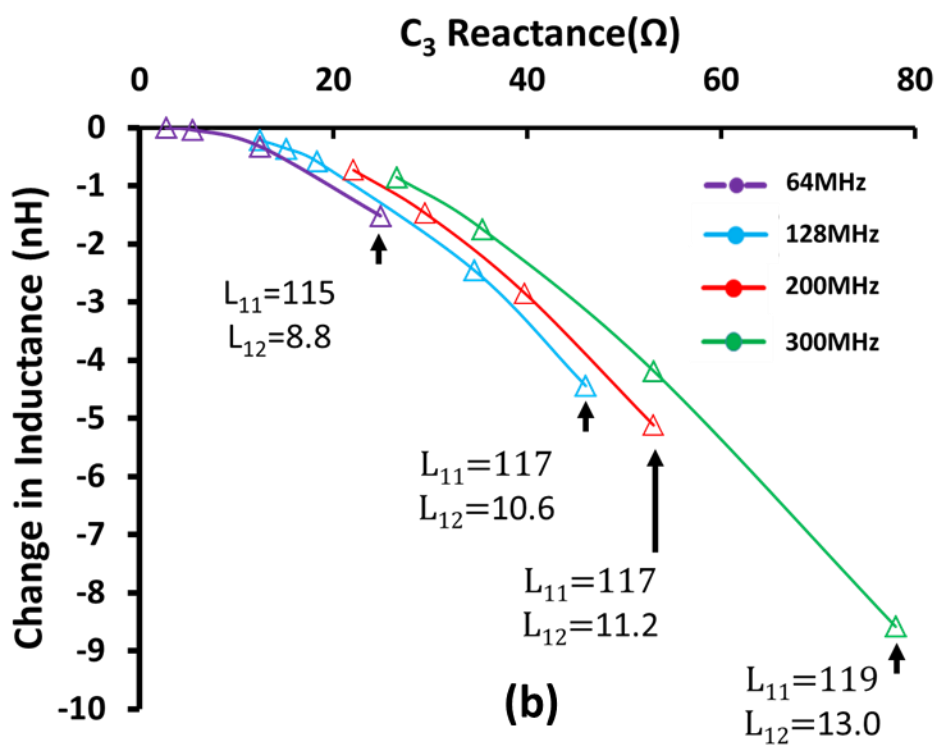
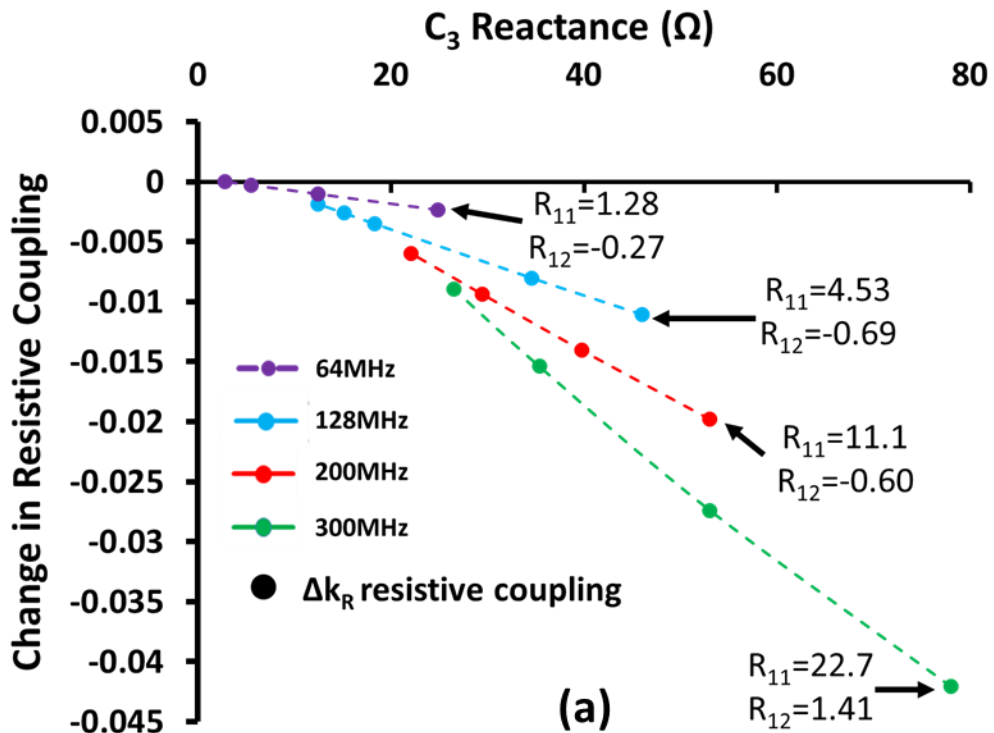


Figure 1.8. Predicted a) Change in resistive coupling coefficient and b) change in mutual inductance due only to stray capacitive coupling ( $C_2=0$ ) predicted using the distributed capacitance model. Arrows indicate actual resistance and inductance values obtained at the largest  $C_3$  reactance.

## 2.4.2. Fitted Parameters

The fitted parameter values for the two-coil array with standard dimensions are listed in Table 1-2. The superscripts are dropped since for this symmetric array  $Z_{Line}^1 = Z_{Line}^2$  and  $Z_{coup}^1 = Z_{coup}^2$ . The inductances found with both models match closely, while the capacitance is consistently larger in the lumped model. The resistance increases approximately in proportion to the square of the frequency, similarly to single coils. The lumped model fitted result for the real part of  $Z_{Line}$  at 300MHz is  $-0.13\Omega$ . Since this value is small its variation had little impact on the impedance predictions, so the lumped model was unable to accurately predict it.

Table 1-2: Model parameters for the two-coil array obtained by fitting using the lumped and distributed models; the array has the standard dimensions and substrate permittivity ( $t = 7$  mm,  $s = 2$  mm,  $w = 9.5$  mm,  $d = 70$  mm,  $\epsilon_r = 3.4$ ).

Parameter	Frequency (MHz)			
	64	128	200	300
$Z_{line}$ <u>distributed</u>	Resistance( $\Omega$ )/ Inductance(nH)			
	0.09/18.9	0.53/18.7	0.87/18.2	0.38/17.3
	0.10/19.1	0.46/20.0	1.60/19.7	-0.13 /17.6
$Z_{coup}$ <u>lumped</u>	-0.20/-8.2	-1.07/-8.0	-2.50/-7.5	-4.65/-6.6
$Z_{coup}$ <u>distributed</u>	-0.21/-8.3	-1.01/-8.4	-2.86/-7.5	-4.69/-5.2
$C_{12}$ <u>distributed</u>	12.3 (pF)	12.1 (pF)	12.5 (pF)	14.0 (pF)
$C_{12}$ <u>lumped</u>	15.5 (pF)	15.6 (pF)	17.7 (pF)	18.9 (pF)

Figure 1.9 shows the value of the stray capacitance  $C_{12}$  and line inductance  $L_{line}$  (reactive part of  $Z_{line}$ ) found by fitting the circuit model components to the simulated data as the parameters  $w$ ,  $t$ , and  $s$ , or  $\epsilon_r$  are varied. The variation of the capacitance with substrate thickness or the line inductance with coil spacing is not shown since there is little change in the analytical and fitted values for the range used.

The analytical solution for capacitance is obtained by quasi-static conformal mapping for coplanar strips of length equal to the coil diameter over a layered substrate [20]. The analytical result for the line inductance is calculated for

rectangular strips with the length of the coil diameter using equations derived by Neumann's formula [21].

In Figure 1.9 the fitted  $C_{12}$  increases marginally with frequency and follows analytical values for coil strip width. The capacitance decreases rapidly as substrate permittivity is reduced. It decreases slightly when substrate thickness is increased, showing that stray capacitance is more dependent on substrate than phantom permittivity unless thickness is small ( $<5\text{mm}$ ). The fitted  $L_{\text{line}}$  is slightly lower than the analytical for the standard spacing, but as spacing increases it increases much faster. Since the self-inductance stays the same, the mutual inductance between strips must decrease slower in the analytical prediction.

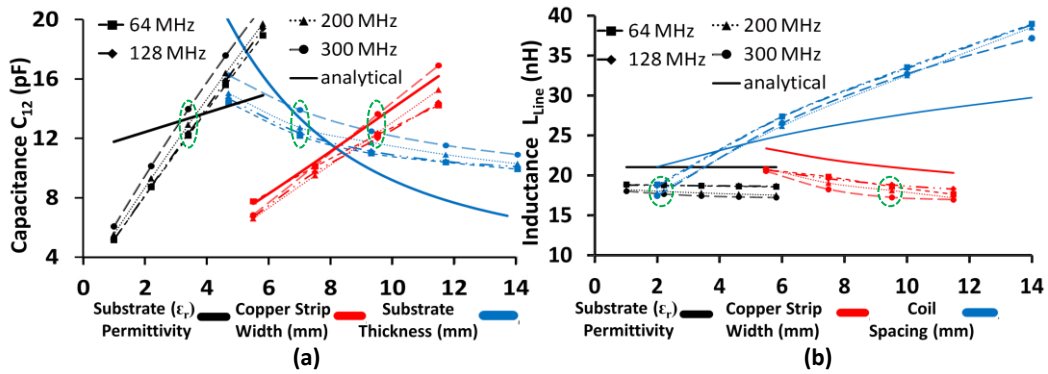


Figure 1.9. a) stray capacitance and b) inductance of capacitively coupled sections, obtained by fitting data to the distributed capacitance model. Line colors indicate different parameters that are varied while line/marker types indicate frequencies ( $f = 0$  for analytical solution). Points circled in green correspond to the standard parameter values.

The non-uniform current along the strip, shielding due to the lossy body, the finite length of the coils and the contribution of the rest of the coil to capacitive coupling are reasons imperfect agreement between quasistatic and fitted values.

Although the quasi-static method of predicting coil impedance parameters has been used extensively [10, 22] it is only accurate at low frequencies. Method-of-Moment methods including the lossy phantom [23], or others where full-wave fields are calculated for the coils individually from the vector potential provide greater accuracy, but this study shows that even if they include the series capacitor

distribution [16], they will not be completely accurate if the scalar potential is not included.

### 2.4.3. Coil Current Transfer

The stray mutual capacitance and subsequent mutual impedance is responsible for inducing currents in the mesh between coils represented by  $I_3$  in equation (1.34). Figure 1.10 shows simulations of the current induced at 128 MHz and 300 MHz by a coil driven by a 1A source current onto an adjacent coil when it is open circuited (i.e., when calculating equation (1.31)). The arrows indicate the direction of the current on the capacitively coupled sections of the coils, which is plotted in the graphs above. When  $I_3/I_n|_{I_{k \neq n}=0}$  in equations (3-4) is positive the current on the capacitively coupled section of the source coil is greater than the source current and the current on the adjacent strip is in the opposite direction; current on both strips adds to the 1A source. The mutual resistance can be increased or reduced depending on the direction of this induced current.

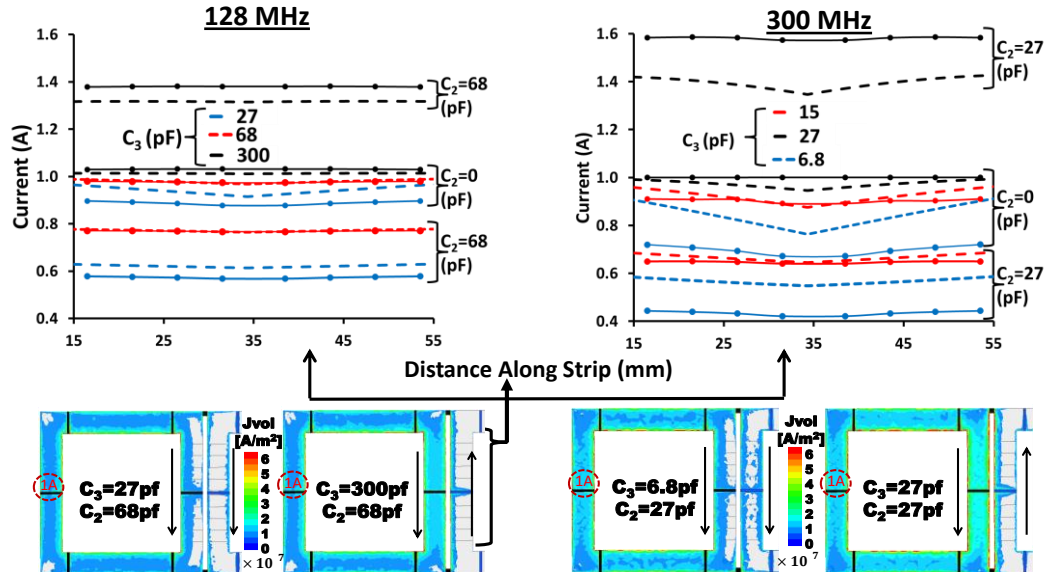


Figure 1.10. Simulated current distributions with 1A source circled in red (bottom) show the differences when current transfer between coils act as a shared current path (current on first strip less than source) versus a coupled current loop (current on first strip less than source) . (top) current along coil strip adjacent to second coil ( $C_2=0$ ). Solid lines with dots are simulated and dashed lines are predicted from using the distributed model.

The imaginary component of the induced current is negligible unless resonance is approached in the loop between the coils. The distributed capacitance model predicts the progressive transfer of current accurately until resonance is approached where current magnitude and phase fluctuate rapidly with changing  $C_2$ . For the reasons cited above this region is not of interest for MRI coil design and therefore does not present a practical limitation of the model.

The prediction of current transfer (dashed lines in Figure 1.10) is more accurate at 128MHz than 300MHz and it is better for the middle of the range of  $C_3$ . This indicates that the fitted model parameter values may change slightly with  $C_3$ , likely for the same reasons stated in section 2.3.1 for fitting to the change in impedance parameters with respect to  $C_2$ . The current in Figure 1.10 stays roughly uniform across the strip, which makes the assumption of lumping mutual impedance between the adjacent strips reasonable. For different shaped coils, such as circular, the uniform distribution of capacitance and impedance will be less accurate, but since the lumped model of capacitance appear to work as an approximation, the distributed model will be applicable treating all variables as average values.

#### 2.4.4. Comparison of Coupling Situations

The simulations and capacitive coupling models predict that a careful choice of  $C_3$  and  $C_2$  can eliminate both the mutual resistance and reactance. Figure 1.11 shows measured  $|S_{21}|$  of the two- and four-coil arrays in the three coupling situations after matching. Completely removing mutual impedance allows for a reduction in  $S_{21}$  to below -50dB compared to  $S_{21} \approx -25$  dB when only the mutual reactance is removed. This result proves that it is possible to eliminate mutual resistance with lossless circuits contrary to what was previously believed [4]. In the four-coil array with no mutual impedance between adjacent coils the mutual coupling between non-adjacent pairs remains unchanged or is slightly improved compared to the other two decoupling.

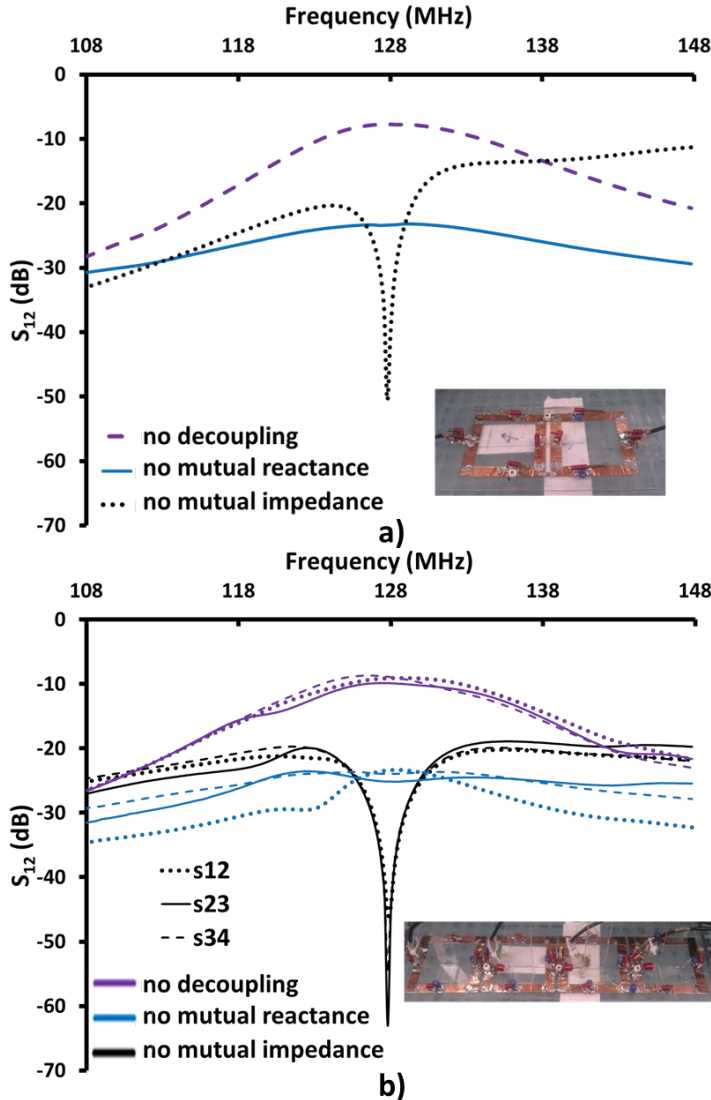


Figure 1.11. Measured  $S_{21}$  between (a) elements of the two coil array and (b) adjacent elements in the four coil array for three mutual impedance conditions.

When mutual resistance is comparable to mutual reactance, as is the case in high-field MRI [6], this method can be used to achieve required decoupling levels. Since very few decoupling methods address mutual resistance between coils this may prove to be the easiest to implement in larger arrays.

Figure 1.12 shows the SNR maps using equation (1.20) in a sagittal slice through the center of the two-coil array, for the same three coupling conditions, when the two coils are aligned along the direction of the static magnetic field ( $B_0$ ) and a coronal slice when they are perpendicular ( $\approx 2.5$  cm depth). The SNR of the

two-coil array with no mutual impedance is greater near the surface because the third shared loop picks up significant signal superficially. In this case there is a slight decrease in SNR farther into the phantom between the coils (red ellipse), likely due to the effects of the shared loop on the sensitivity patterns of the main loops. The average SNR in the three cases is nearly indistinguishable (within 2%), with some minor regional differences.

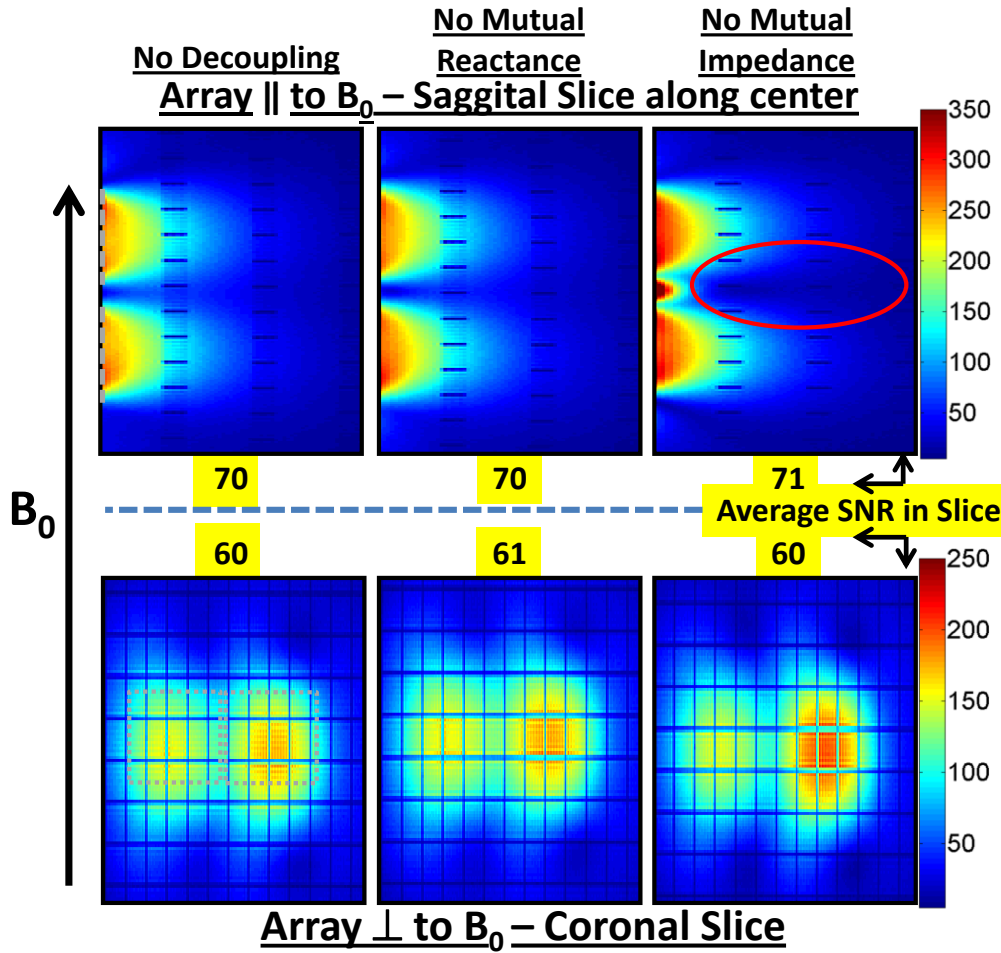


Figure 1.12: Measured two-coil optimum combination SNR maps and averages for three decoupling cases. Dashed white lines in the ‘No Decoupling’ case indicate the location of coils on the surface for two orientations of the array (parallel or perpendicular to  $B_0$ ).

The four-coil array topology shown in Figure 1.5 allows the high impedance at the coil ports to be placed in series with the shared mesh (Figure 1.5) and thus the current and signal are not enhanced by resonance. As shown in Figure 1.13 this feature leaves the single-coil sensitivities unaltered, unlike what is observed in

Figure 1.12 for the two-coil array. In Figure 1.13 the optimal SNR maps as well as g-factor maps (acceleration factor  $R = 4$ ) are compared for the three versions of the four-coil array.

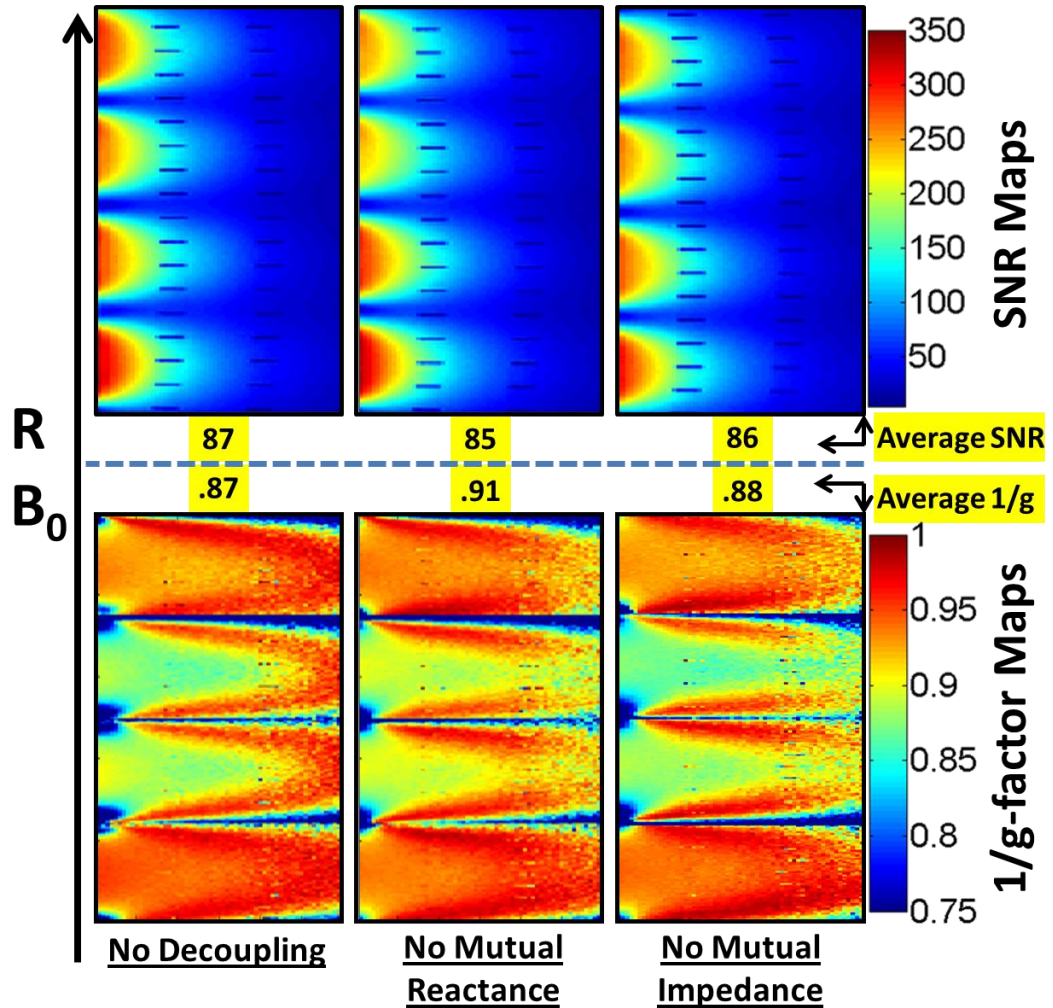


Figure 1.13. Measured four-coil optimal SNR and  $1/g$ -factor maps for an acceleration factor  $R = 4$ . The regional differences in SNR visible in the 2-coil array (Figure 10) are eliminated with careful port placement (Figure 1.5). Main differences in the  $g$ -factor maps are deep ( $>7\text{cm}$ ) in the phantom where SNR is low and thus of little consequence.

The corresponding mean and minimum  $1/g$ -factors are listed in Table 1-3 and do not indicate systematic differences between the three tuning arrangements, with slightly better performance at  $R=4$  when mutual reactance is zero. Differences in the average SNR are again insignificant (below 2%).

Table 1-3: 1/g-factors for the 4-coil array up to an acceleration factor of 4

SENSE Acceleration	1/g factor mean/min		
	No decoupling	No mutual reactance	No mutual impedance
2	0.98/0.81	0.99/0.80	0.99/0.84
3	0.91/0.74	0.92/0.48	0.93/0.70
4	0.87/0.02	0.91/0.28	0.88/0.03

The mutual impedances measured between coils in the arrays (at the coil ports before the matching circuits) are listed in Table 1-4 along with the measured noise correlations. Measured self-resistance of 4- and 2-coil arrays are  $6.2 \Omega$  and  $5.2 \Omega$  respectively.

Table 1-4: Average measured mutual impedances and noise correlation coefficients (%) between adjacent coils.

	No Decoupling	No Mutual Reactance	No Mutual Impedance
Noise correlation and mutual impedance (in parentheses)	Two coil (-0.99+j5.25) $\Omega$	13.4 % (-0.88+j0.04) $\Omega$	14.0 % 3.2 % (-0.004-j0.01) $\Omega$
	Four coil (0.42-j6.10) $\Omega$	5.19 % (0.44+j0.18) $\Omega$	9.03 % 1.27 % (0.09-j0.16) $\Omega$

The mutual impedance is almost completely eliminated and the noise correlation is reduced to levels similar to the lower bound obtained from noise scans with receiver channels terminated in uncoupled  $50 \Omega$  loads (1.3% average noise correlation). The noise correlation of the no mutual reactance and no decoupling cases are slightly different because equation (1.23) indicates the finally noise covariance has a dependence on the overall impedance matrix as well as the real part which is slightly different for the two.

## 2.5.Conclusion

The models described in this chapter are the first quantitative investigation of the effect of stray and intentional capacitive coupling on the two-port impedance parameters of array coils. The mutual impedances resulting from various distributions of coil capacitance are accurately predicted at the most common MRI frequencies. The values of stray capacitance obtained from the models by fitting are consistent with those calculated using analytical methods. The distributed

model is accurate over a larger range of design parameters than the lumped model, and is able to account for the progressive transfer of current along the coupled sections of adjacent coils.

Both models provide valuable insight into the mechanisms and effects of capacitive coupling in MRI coil arrays. For example, the models predict that mutual impedance, including mutual resistance, can be reduced to negligible levels using inter-element capacitors. This result was verified experimentally and is consistent with a recently-published method that requires introducing small coupling loops between coils [6]; in this chapter the decoupling element between coils is the shared loop introduced by the capacitive coupling . Removing mutual resistance in addition to mutual reactance does not compromise SNR, but allows previously unachievable levels of decoupling with anticipated benefits in transmit and high-density arrays. Cancelling mutual resistance using this method in traditional overlapped coil arrays is unlikely to be possible. However, since crosstalk is readily eliminated using reflective preamps or capacitive decoupling, our method of cancelling mutual resistance suggests that overlapping is not only unnecessary, but also undesirable.

## Bibliography

- [1] T. Vaughan, L. DelaBarre, C. Snyder, J. Tian, C. Akgun, D. Shrivastava, W. Liu, C. Olson, G. Adriany, J. Strupp, P. Andersen, A. Gopinath, d. M. van, M. Garwood and K. Ugurbil, "9.4T human MRI: Preliminary results," *Magn. Reson. Med.*, vol. 56, pp. 1274-1282, 2006.
- [2] C. E. Akgun, "Radiofrequency fields and SAR for transverse electromagnetic (TEM) surface coils," in *Encyclopedia Magnetic Resonance*Anonymous John Wiley & Sons, Ltd, 2011, .
- [3] P. Vedrine, W. A. Maksoud, G. Aubert, F. Beaudet, J. Belorgey, S. Bermond, C. Berriaud, P. Bredy, D. Bresson, A. Donati, O. Dubois, G. Gilgrass, F. -. Juster, H. Lannou, C. Meuris, F. Molinie, M. Nusbaum, F. Nunio, A. Payn, T. Schild, L. Scola and A. Sinanna, "Latest Progress on the Iseult/INUMAC Whole Body 11.7 T MRI Magnet," *Applied Superconductivity, IEEE Transactions on*, vol. 22, pp. 4400804-4400804, 2012.
- [4] C. D. Constantinides, E. Atalar and E. R. McVeigh, "Signal-to-noise measurements in magnitude images from NMR phased arrays," *Magnetic Resonance in Medicine*, vol. 38, pp. 852-857, 1997.

- [5] S. B. King, S. M. Varosi and G. R. Duensing, Optimum SNR data compression in hardware using an eigencoil array *Magn. Reson. Med.* 63(5), pp. 1346-1356. 2010.
- [6] N. I. Avdievich, J. W. Pan and H. P. Hetherington, "Resonant inductive decoupling (RID) for transceiver arrays to compensate for both reactive and resistive components of the mutual impedance," *NMR Biomed.*, pp. n/a-n/a, 2013.
- [7] C. E. Hayes and P. B. Roemer, "Noise correlations in data simultaneously acquired from multiple surface coil arrays," *Magn. Reson. Med.*, vol. 16, pp. 181-191, 1990.
- [8] P. B. Roemer, W. A. Edelstein, C. E. Hayes, S. P. Souza and O. M. Mueller, "The NMR phased array," *Magn. Reson. Med.*, vol. 16, pp. 192-225, 1990.
- [9] G. C. Wiggins, J. R. Polimeni, A. Potthast, M. Schmitt, V. Alagappan and L. L. Wald, "96-Channel receive-only head coil for 3 Tesla: Design optimization and evaluation," *Magn. Reson. Med.*, vol. 62, pp. 754-762, 2009.
- [10] B. Keil, G. C. Wiggins, C. Triantafyllou, L. L. Wald, F. M. Meise, L. M. Schreiber, K. J. Klose and J. T. Heverhagen, "A 20-channel receive-only mouse array coil for a 3 T clinical MRI system" *Magn. Reson. Med.*, vol. 66, pp. 582-593, 2011.
- [11] M. L. Morris and M. A. Jensen, "Network model for MIMO systems with coupled antennas and noisy amplifiers," *Antennas and Propagation, IEEE Transactions on*, vol. 53, pp. 545-552, 2005.
- [12] R. G. Pinkerton, E. A. Barberi and R. S. Menon, "Noise properties of a NMR transceiver coil array," *Journal of Magnetic Resonance*, vol. 171, pp. 151-156, 11, 2004.
- [13] K. N. Kurpad, S. M. Wright and E. B. Boskamp, "RF current element design for independent control of current amplitude and phase in transmit phased arrays" *Concepts Magn. Reson.*, vol. 29B, pp. 75-83, 2006.
- [14] X. Chu, X. Yang, Y. Liu, J. Sabate and Y. Zhu, "Ultra-low output impedance RF power amplifier for parallel excitation" *Magn. Reson. Med.*, vol. 61, pp. 952-961, 2009.
- [15] C. Chen, D. I. Hoult and v, *Biomedical Magnetic Resonance Technology*. Bristol: Adam Hilger, 1989.
- [16] J. Wei, J. Yuan and G. X. Shen, "Effect of tuning capacitor placement on mutual coupling for MRI array coils" *Concepts Magn. Reson.*, vol. 29B, pp. 50-54, 2006.
- [17] A. Kumar, W. A. Edelstein and P. A. Bottomley, "Noise figure limits for circular loop MR coils," *Magn. Reson. Med.*, vol. 61, pp. 1201-1209, 2009.
- [18] H. SUNDQVIST and G. VERONIS, "A simple finite-difference grid with non-constant intervals," *Tellus*, vol. 22, pp. 26-31, 1970.

- [19] D. M. Peterson, "Impedance matching and baluns," in *Encyclopedia Magnetic Resonance* Anonymous John Wiley & Sons, Ltd, 2011, .
- [20] Erli Chen and S. Y. Chou, "Characteristics of coplanar transmission lines on multilayer substrates: modeling and experiments," *Microwave Theory and Techniques, IEEE Transactions on*, vol. 45, pp. 939-945, 1997.
- [21] C. Hoer and C. Love, "Exact Inductance Equations for Rectangular Conductors With Applications to More Complicated Geometries," *J. Res. Nat. Bur. Stand.*, vol. 69C, pp. 127-137, 1965.
- [22] J. Wang, A. Reykowski and J. Dickas, "Calculation of the signal-to-noise ratio for simple surface coils and arrays of coils " *IEEE Trans. Biomed. Eng.*, vol. 42, pp. 908-917, Sep, 1995.
- [23] S. M. Wright, "Full-wave analysis of planar radiofrequency coils and coil arrays with assumed current distribution," *Concepts Magn. Reson.*, vol. 15, pp. 2-14, 2002.

# Chapter 3

## Experimental Verification of SNR and Parallel Imaging Improvements Using Composite Coils

### 3.1. Introduction

Completeness of the basis is necessary to approach the ultimate intrinsic SNR in both standard and parallel imaging [1]. Since coil loops capture only field components that are *normal* to the surface of the VOI, it is natural to ask whether the tangential components carry any additional information that could improve SNR or parallel imaging performance. This has motivated the theoretical work of Wang [2, 3], in which standard dipole sources with  $B_1$  normal to the surface of the VOI are supplemented by the two orthogonal components tangential to the surface. This arrangement approximates a complete array coil and simulations [3] have shown that composite coils consisting of three orthogonal loops can better construct the magnetic multipole expansion vector fields than equivalent and greater numbers of flat loops. Additional simulations by Wang [2] with truncated orthogonal coils and realistic resistive loading confirm the potential increases in SNR as well as iSNR [4], but do not account for realistic electromagnetic coupling and noise correlation between the elements. The parallel imaging potential of such arrays also remains to be investigated.

To date, a full experimental implementation of composite arrays has not been reported, although the partial approach of Mueller et al. [5] at 1.5T has shown promising SNR improvements for surface coils paired with a single orthogonal coil oriented parallel the  $B_0$  field. This additional coil improves sensitivity in the same region as the surface coil similarly to the butterfly coil [6] and so-called vertical coil [7], but with a much shorter conductor length and stray capacitance to neighboring coils, making it potentially a better choice. We show that the third coil element that is omitted in (9) provides a high sensitivity in the region *between* the surface coil elements and thus provides a noticeable reduction in SENSE g-factor

values. The by resistive and inductive coupling affects the array performance [8, 9], so the behavior of the upright coil coupling with adjacent coils is investigated thoroughly.

### 3.2. Theory of Composite Coils

In this study the complete coil system suggested by Wang [3] is approximated by an array of composite coils [2], each consisting of three orthogonal rectangular loops arranged according to Figure 3.1. Multiple such triplets can be arranged to cover the surface of the VOI similarly to standard surface coil arrays.

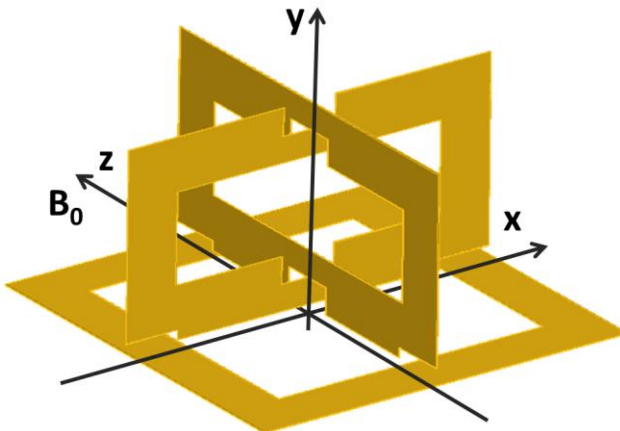


Figure 3.1: A composite coil element made up of three isolated orthogonal coils. The signal-producing region is located below the square surface coil ( $y < 0$ ).

A composite coil triplet can produce linearly or elliptically polarized RF magnetic fields in three orthogonal orientations at any spatial location. Simulations have shown that an array of such composite coils provides a better approximation of a complete basis set [3] than surface coil elements alone, in part because of the additional degrees of freedom in the direction of the magnetic fields produced and also because the number of independent loops per unit surface is tripled.

Composite coil array construction, however, is more challenging than traditional array construction because there are numerous locations where the coils are in close proximity but must avoid physical contact. Possible solutions are to use upright coils that are smaller than the inner radius of the surface coil element and that have different heights. Since the upright coils must rise above the surface

a rigid structure must be made to support the coil loops orthogonal to each other and to support the feed cables. These additional mechanical components also make flexible coil design more challenging. Finally, the presence of upright coils makes overlapping surface coils to achieve minimal mutual inductance more difficult.

When capacitive coupling and cable interactions are neglected, and the sample is homogeneous, the mutual impedance between orthogonal coils in one triplet is zero if the coils are arranged symmetrically as in Figure 3.1 [10]. This attractive property was verified by simulation and measurement of the impedance matrix and ensures that crosstalk will be minimal within the triplet. Instead of using upright coils this behavior can also be achieved with coils such as the butterfly coil [11] (essentially an unfolded, 2-turn upright coil) or the “wheel-and-spoke” coil [6, 10] (a butterfly coil combined with a loop) that have similar field patterns. However, in addition to having a longer conductor length a butterfly coil also has greater potential for capacitive coupling to the surface loop and to the second butterfly coil needed for the third channel of the triplet. Upright coils are therefore a natural choice in high density arrays even though they require some mechanical support above the surface.

Coils in adjacent triplets (surface or upright) are not arranged with the necessary symmetry that provides zero mutual impedance. This coupling, as well as any that arises from imperfect construction and non-ideal behavior, affects the final image SNR as described below.

### 3.3. Construction

Coils were constructed of 9.5-mm-wide self-adhesive copper strips (Venture Tape Corp., Rockland, MA, USA) attached to 2-mm-thick polycarbonate sheets. Capacitors (700B series, American Technical Ceramics; USA) are distributed along the coil loop to split its length into sections of one twentieth of a wavelength or less [12]. On the upright coils the capacitor at the connection point is further split equally on either side the coaxial cable ground to provide a partially balanced match [13].

An 8-channel array was assembled from three surface elements of dimensions  $7 \times 7 \text{ cm}^2$ , aligned in the direction parallel to  $B_0$  and separated by 3 mm gaps. Five upright elements  $7 \times 3.5 \text{ cm}^2$  in size (see Figure 3.2) are positioned orthogonally above the surface coils and can be detached to allow the comparison of performance with and without their presence. The coils are connected using  $\lambda/2$  coaxial cables to eight low-impedance preamplifiers (input impedance  $Z_{\text{pre}} = 6 \pm 3 \Omega$  measured with all 8 preamplifiers, minimum noise figure 0.90 dB at  $43+13j \Omega$  impedance) housed within a connector box (Philips Healthcare; Cleveland, OH). Due to the limited number of preamplifiers the middle surface coil has only one corresponding upright coil which is oriented in the plane orthogonal to  $B_0$  to provide increased SNR in regions where the centre surface coil has low SNR. The self-inductance of the surface coils is  $123 \pm 4 \text{ nH}$ , requiring an equivalent series capacitance of  $13 \text{ pF}$  to resonate at 128 MHz, while that of the upright coils is  $70 \pm 3 \text{ nH}$  which requires  $22 \text{ pF}$ . Values of  $Q_{\text{unloaded}}$ ,  $Q_{\text{loaded}}$  and corresponding coil efficiency [14] are given in Table 3-1. The average measured loaded resistances of the surface and upright coils are  $4.9 \pm 0.3 \Omega$  and  $0.40 \pm 0.03 \Omega$  respectively.

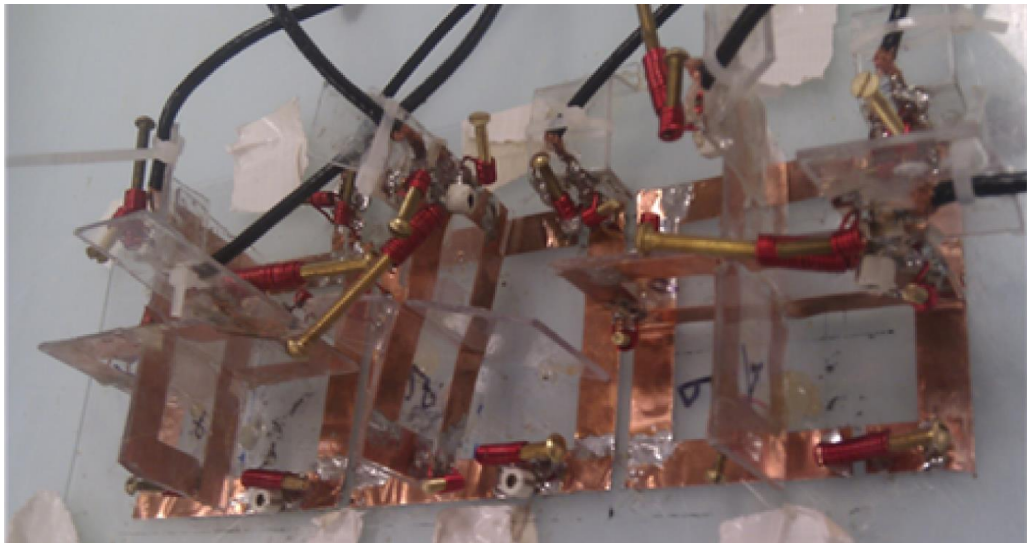


Figure 3.2: the 8-element composite coil array built to measure SNR and parallel imaging performance.

### 3.3.1. Matching and Transmit Detuning

Surface coils are matched using a quarter-wave lattice balun (Figure 1.2a) since it provides, simultaneously, effective balancing and a high blocking

impedance when connected to a low-input-impedance preamp. The elements  $C_m$  and  $L_m$  used are approximately 68 pF and 23 nH. The upright coils, however, have a much lower resistance than the surface coils at 128 MHz and would therefore require impractically low inductance values for the lattice balun. Instead, the  $\pi$  matching network in Figure 1.2b is used, where  $C_m$ ,  $C_{m2}$ ,  $C_{m3}$  and  $L_m$  are, respectively, 47 pF, 10 pF, 38 pF and 27 nH. Reasonable equivalent series resistances (ESR) for the lumped elements in Figure 1.2 are obtained from manufacturers' data sheets. The capacitors used in this work have an ESR of  $\approx 0.05 \Omega$  according to American Technical Ceramics (Huntington Station, NY, USA, <http://www.atceramics.com/products.aspx>) and, according to Coilcraft (Cary, IL; USA; <http://www.coilcraft.com/midi.cfm>), aircore inductors similar to those used here have an ESR of  $\approx 0.12 \Omega$ . These values are used to find the noise factors of the matching networks with equation (1.23).

Noise figures (the noise factor expressed in decibels) derived using equations (1.27) and (1.28) for each stage in the coil receiver chain are shown in Figure 3.3, where the 0 dB level corresponds to noise originating only in the body or phantom (corresponding to the intrinsic SNR). The coil noise is dominant for the upright coil and because of the low body loading the matching circuitry contributes relatively more noise to the upright coil than to the surface coil. Overall, for the surface coils the decrease in SNR due to the matching networks is only 0.9% (0.08 dB noise figure) and approximately 4.1% (0.37 dB noise figure) for the 3.5cm high upright coils used in the 8-coil array. As illustrated in Figure 3.3 these decreases are still small in comparison to the 3.3% and 29% decrease for surface and upright respectively due to coil losses and 9.8% due to the preamplifiers (corresponding to their 0.9 dB minimum noise figure).

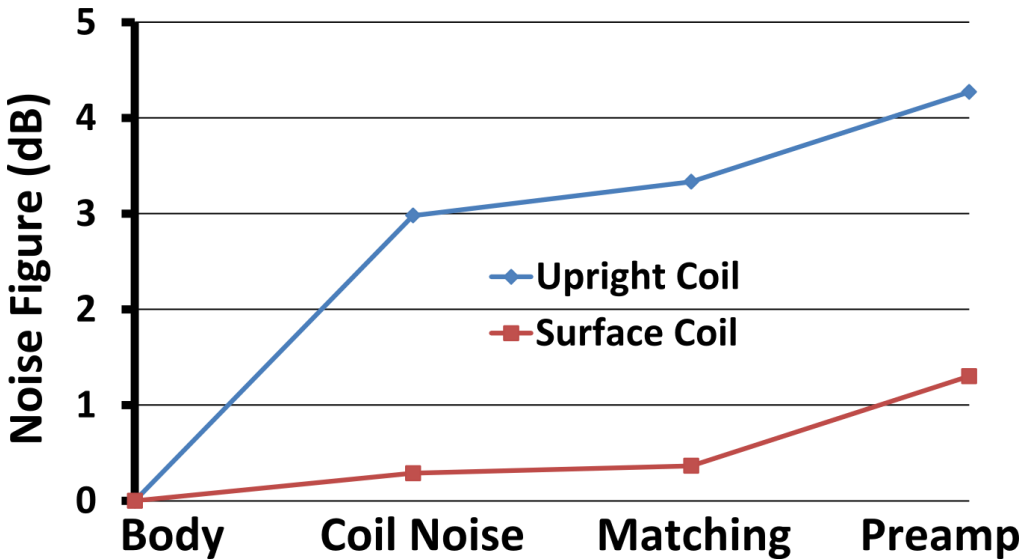


Figure 3.3: various contributions to noise figure for surface and upright coils. The largest difference is due to coil noise which is a much larger contribution in upright coils because they are not in sample-dominated regime.

The preamplifier decoupling effectiveness is measured using equation (1.30) is 14 dB for the surface coils and 12 dB for the upright coils, which is consistent with the values of 16 dB and 13 dB calculated as the ratio of the impedance of the coil mesh when in the two matching conditions (power match vs. noise match)

While better preamplifier decoupling is possible using preamplifiers with smaller input impedances (e.g., 25dB [15] and 30dB [16]), in this study no resonance splitting was observed and the noise correlations between surface coils are acceptably small (c.f. Full Array Results). The positions of the two active PIN diode traps used to detune each coil during transmission with the system's body coil are also shown in Figure 1.2. Detuning effectiveness, measured similarly to decoupling with equation (1.30), is greater than 35 dB.

### 3.3.2. Cabling

Cable placement in an array requires careful consideration to minimize the additional coupling between cables and the coils' electric fields [8]. Near the coils it is desirable to route cables along lines of zero or low tangential electric fields such as along lines of electrical symmetry created by baluns and symmetric capacitor placement. In many cases such as this array this criterion is not easily

satisfied because of lack of symmetry and geometrical constraints; the layout of Figure 3.4 was found to provide acceptable performance.

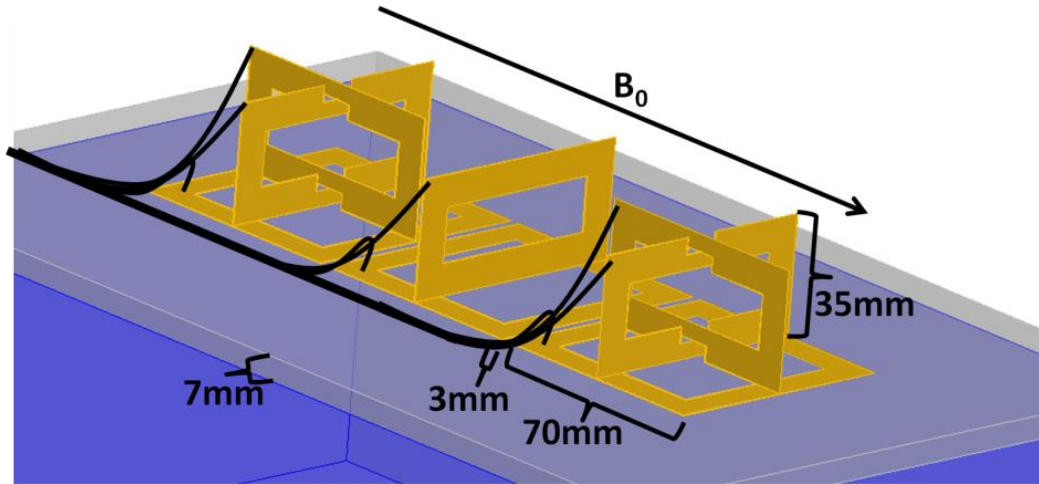


Figure 3.4 Cable routing and coil orientation relative to  $B_0$  for which the 8-coil array was designed. Coil dimensions and spacing are also shown.

### 3.4. Upright coil height optimization

The effect of the height of upright coils on SNR was studied to verify the existence of an optimum beyond which further increases in coil height would be detrimental due to increases in self-resistance, and mutual inductance and resistance between neighboring coils. Four coils 7 cm in length and 1 to 4 cm in height were built using 1-mm-diameter silver-plated wire as shown in Figure 3.5. Similar coils made of 8-mm copper strip did not result in substantial differences in loading or SNR, and thus wire was preferred to facilitate the numerical simulations performed for comparison (below). Images were taken by sequentially placing individual upright coils on a uniform phantom in the same position in the scanner.

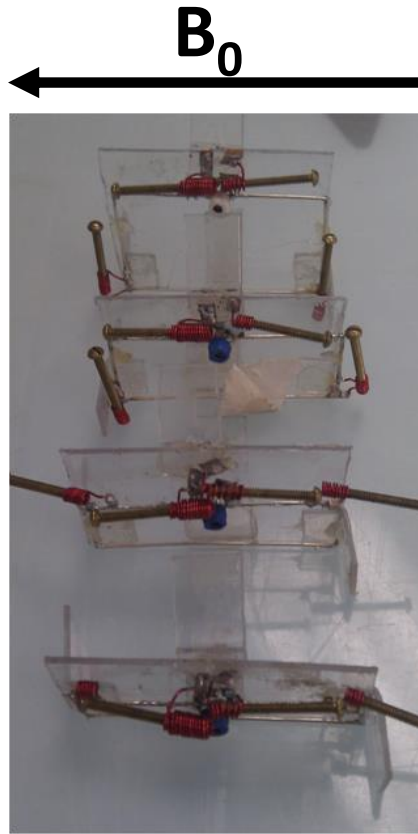


Figure 3.5: upright coils built for comparison with heights ranging between 1 and 4 cm.

The plane of the coil was parallel to the static magnetic field, thus providing the highest SNR directly below the coil. The average SNR was measured within three sagittal slices (one centered with the coil and two offset by  $\pm 3.5\text{cm}$ ) for pixels  $\pm 7\text{cm}$  in the direction of  $B_0$  and to a depth of 8 cm. The measured  $Q_{\text{unloaded}}/Q_{\text{loaded}}$  and efficiency values are provided in Table 3-1 and for the upright coils they are similar to the value of 2.00 assumed in the simulations in reference [2] for square coils with 5.5cm side length.

Upright wire coils with heights ranging between 5 and 55 mm and strip coils with heights between 20 and 55 mm were simulated (see Simulation using the Finite Element Method below), and the SNR was calculated in slices with the same positioning as for the measurements above from the transverse circularly polarized magnetic field per unit current and resistance using standard formulas (e.g., equation 21 in reference [17]). Average SNR across the slices was

Table 3-1: Quality factors in unloaded ( $Q_{\text{unloaded}}$ ) and loaded ( $Q_{\text{loaded}}$ ) conditions for all coils used in this study; individual upright coils used for height optimization are made with silver-plated copper wire to facilitate simulations, and surface/upright coils in the final array are made with copper strip. Efficiency  $\eta = 1 - \frac{Q_{\text{loaded}}}{Q_{\text{unloaded}}}$  [14].

Upright coils (individual, wire)					Upright Coils (in array, strip)	Surface Coils (in array, strip)
	7cm×1cm	7cm×2cm	7cm×3cm	7cm×4cm	7cm×3.5cm	7cm×7cm
$Q_{\text{loaded}}$	190	167	165	180	140±12	19.8±0.8
$Q_{\text{unloaded}}$	240	302	360	395	280±20	310±41
$\eta$	0.208	0.447	0.542	0.544	0.491	0.935

normalized for each coil to the maximum of the wire coils and shown in Figure 3.6 along with the corresponding measured values for wire coils. The maximum SNR of the strip coils occurs with a larger height than the wire coils (between a height of 4 and 5 cm). The copper strip coils reach a higher SNR because their conductor ohmic losses are lower, while reaching a maximum SNR with larger height because the 9.5 mm copper strip width decreases the distance from the phantom and current on the coil; the effective height of the coil is also smaller (distance between inner conductor edges where most of the current actually flows). This behavior contrasts with that in reference [5], where SNR increases exponentially with *decreasing* coil height because coil losses are neglected.

The height of the upright coils in the final version of the array was chosen to be 3.5 cm. A smaller coil height is preferred for lower coupling between adjacent elements and the 5% increase expected with a 55mm height from Figure 3.6 is minor.

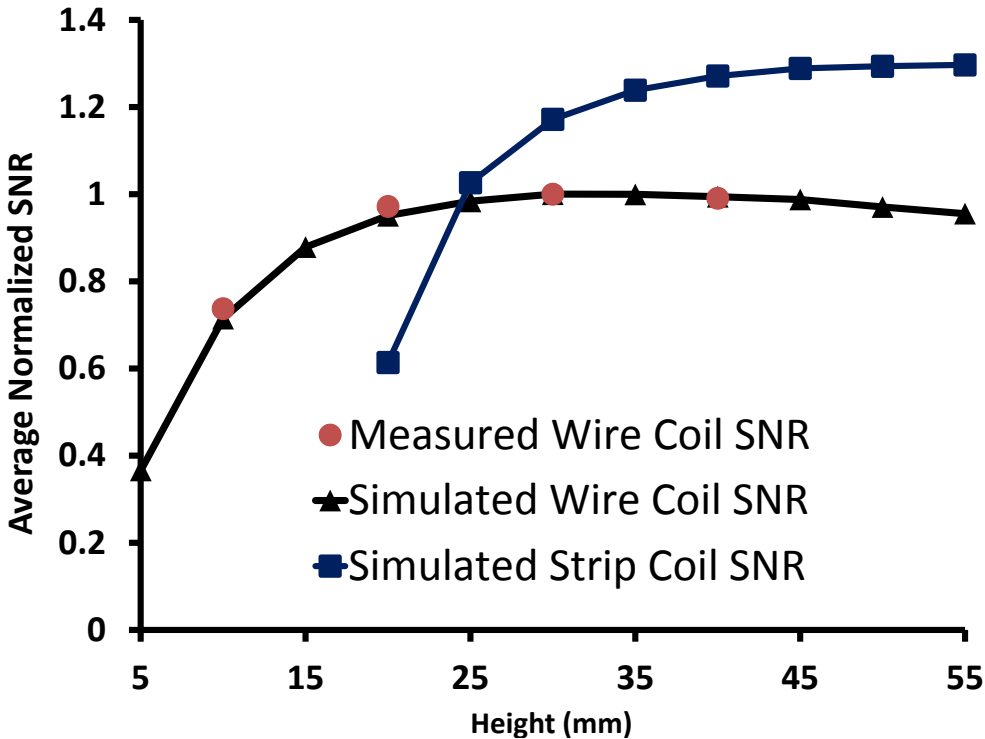


Figure 3.6: measured and simulated SNR of upright wire coils and simulated SNR of copper strip coils, averaged in three sagittal slices as a function of coil height and normalized to the maximum SNR achieved with wire coils. The simulated SNR assumes an equivalent series resistance of  $0.05 \Omega$  for each of the two tuning capacitors in addition to losses in the coil conductors ( $0.15\text{--}0.30\Omega$ ).

### 3.4.1. Simulation using the Finite Element Method

All electromagnetic field simulations of the coils were performed using the finite-element software HFSS [18] (Ansys Corp., Canonsburg, PA, USA) using the driven modal solution method with lumped ports located at the coil terminals to calculate the impedance matrices and then replaced with current sources to calculate the magnetic fields produced per unit current. Stability of the solution (fields maps and S-parameter matrices) is ensured by adaptive meshing which iteratively reduces the mesh size until the solution becomes invariant of grid size. Results were analyzed in MATLAB (The MathWorks, Natick, MA, USA), e.g., to calculate SNR from the fields and resistances as indicated in Upright coil height optimization.

Geometrical dimensions of the models are the same as those built for experimental measurements and each coil is made resonant at 127.8 MHz with

lumped capacitors distributed as in the corresponding coil construction. The lossy phantom solution ( $\epsilon_r = 76$ ,  $\sigma = 0.8 \text{ S/m}$ ) is situated 7 mm below the coils to account for the 2 mm polycarbonate sheet and 5-mm-thick PMMA phantom shell. According to §3.4 the upright coils are simulated using 1 mm silver wire and simulations are repeated with the various coil heights. The final copper strip coils were modelled as built using 9.5 mm wide copper strip 0.04 mm in thickness, 3.5 cm high upright coils, and 7 cm square surface coils.

The geometries are simple enough that each simulation run takes only 10–15 minutes on a computer with an AMD A8-3850 2.9GHz accelerated processing unit (APU) and 16GB of RAM.

### 3.5. Experimental Methods

#### 3.5.1. Imaging Measurements

All images in this study were taken on a  $36 \times 26 \times 11 \text{ cm}^3$  phantom with three grid planes at approximately 2.5 cm, 5 cm and 7.5 cm depth. The phantom is filled with 3.6 g/l NaCl and 1.96 g/l CuSO<sub>4</sub>·5H<sub>2</sub>O to simulate the human body. The solution has approximately a relative permittivity of 76 and conductivity of 0.8 S/m [19]. Gradient-echo imaging is used ( $T_R/T_E = 11/1.95 \text{ ms}$ , pixel bandwidth = 727.2 Hz, acquisition matrix  $256 \times 256$ , FOV = 30 cm, 1 average). Scans are also taken without excitation to calculate the noise covariance matrix (see Noise below).

The SENSE g-factors are calculated for each acceleration factor using equation (1.22), and pixels where the intensity is less than 1% of the maximum are excluded to avoid g-factor discontinuities in noisy regions.

### 3.6. Comparison of Upright Coil Orientations

Unlike surface coils, the sensitivity profile for upright coils and others such as the butterfly [11], microstrip [20] and vertical [7] coils is strongly influenced by a rotation of the coils around an axis that is normal to the surface. The coupling between adjacent coils also depends on such rotations, potentially influencing array performance. We therefore investigated how the orientation of the upright coils influences coupling and overall SNR by considering arrangements in which the

upright coils are oriented in alignment or diagonally with respect to the arrangement of the composite elements on the surface.

### 3.6.1. Simulation

Figure 3.7 illustrates simulated resistive and inductive coupling coefficients [8] at varying separations between a surface coil and an upright coil when it is perpendicular to the direction of separation, when rotated at 45°, and when parallel to the direction of separation. Simulations were performed with the geometric dimensions detailed in Upright coil height optimization. The coupling coefficients for all three situations start near zero with zero separation (upright coil centered on the surface coil) as expected from symmetry. Resistive coupling shows a sharp inflection in the perpendicular orientation at a distance of 35 mm, i.e., when adjacent coil segments are essentially overlapped thus creating considerable stray capacitive coupling that modifies the mutual impedance [21]. The analysis of coupling changes due to capacitive coupling are detailed extensively in Chapter 2; specifically section 2.4.1. The inductive coupling coefficients falls quickly with increasing spacing, while the resistive coupling coefficient remains considerable even up to two coil diameters away from center. The perpendicular and parallel coil orientations were chosen for the final coil array since with this arrangement at least one set of coil pairs exhibits negligible coupling. This compares favorably to the 45° rotated arrangement in which both orientations required to create a composite coil exhibit strong coupling to neighboring elements which needs to be carefully managed, e.g., by using preamp decoupling.

It should also be noted that, in absolute terms, the reactive component of the mutual impedance is far more dominant over the resistive component even though the resistive coupling coefficients are larger in Figure 3.7. The magnitude of reactive to resistive coupling between upright and surface coils is given by the ratio

$$\frac{X_{12}}{R_{12}} = \frac{m_{12}\omega\sqrt{L_{11}L_{22}}}{r_{12}\sqrt{R_{11}R_{22}}} = \sqrt{Q_{loaded}^{upright}Q_{loaded}^{surface}} \frac{m_{12}}{r_{12}} \approx 53 \frac{m_{12}}{r_{12}}, \quad (3.1)$$

where the  $Q_{loaded}$  values are given in Table 3-1; This ratio is much larger than unity since  $r_{12}/m_{12}$  is rarely comparable or larger than 53.

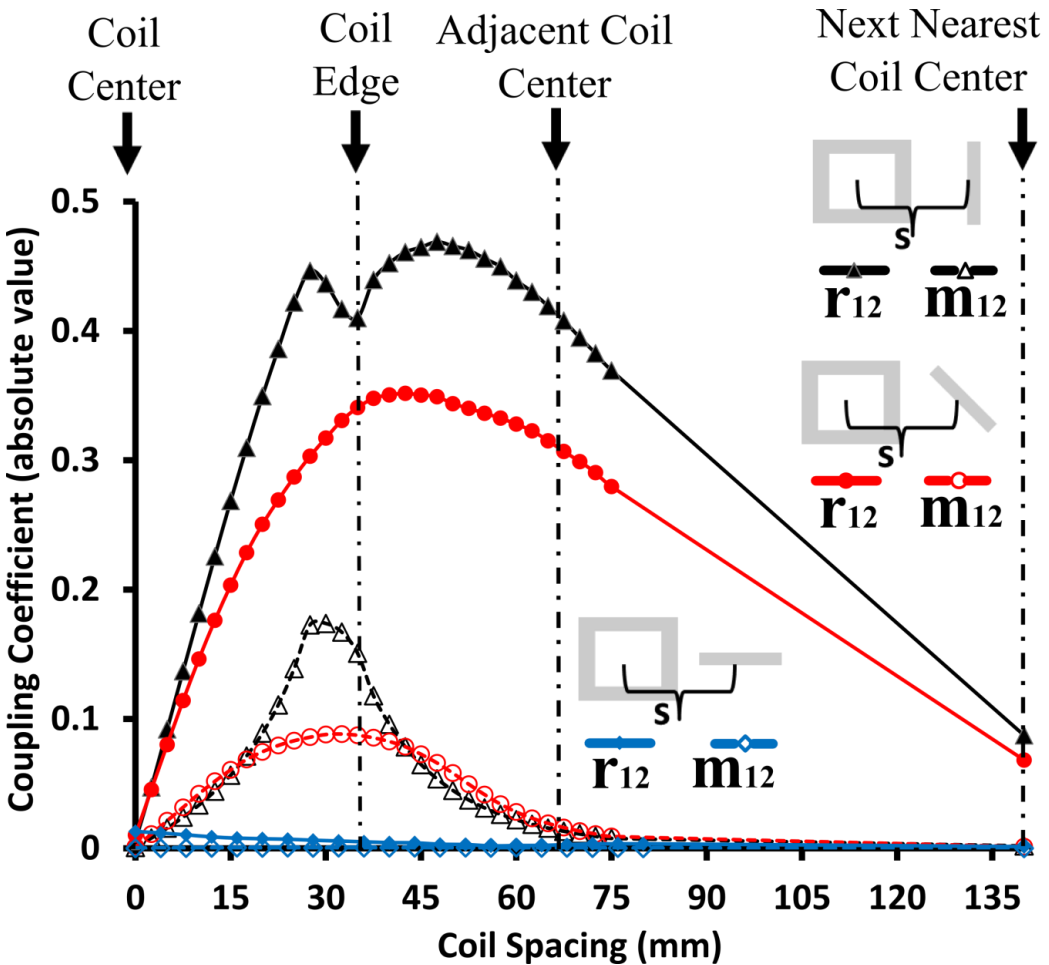


Figure 3.7: Plots of resistive ( $r_{12}$ ) and inductive ( $m_{12}$ ) coupling coefficients between upright and surface coils ( $70 \times 70 \text{ mm}^2$ ) with varying separation. The upright coil is either perpendicular to the direction of separation (triangles), rotated  $45^\circ$  (circles) or oriented parallel to the direction of separation (diamonds). The coefficients were found using Finite Element simulation with HFSS.

### 3.6.2. Noise Correlation and SNR

The simulations of the previous section were confirmed by constructing a simplified four-element array composed of two surface coils and two upright coils oriented firstly along the axes of the array, and subsequently at  $45^\circ$  with the axes. Noise correlation (Figure 3.8) was calculated from simulated and measured Z-parameters using equation (1.23) both with and without the effect of the additional noise added by the matching network and preamplifier (assuming a noise figure of 0.9 dB). For comparison, noise data were acquired by scanning without RF

excitation and the noise covariance between the acquisition channels was calculated from the data using the MATLAB “cov” function. Results in Figure 3.8 indicate overall agreement of the various measurements.

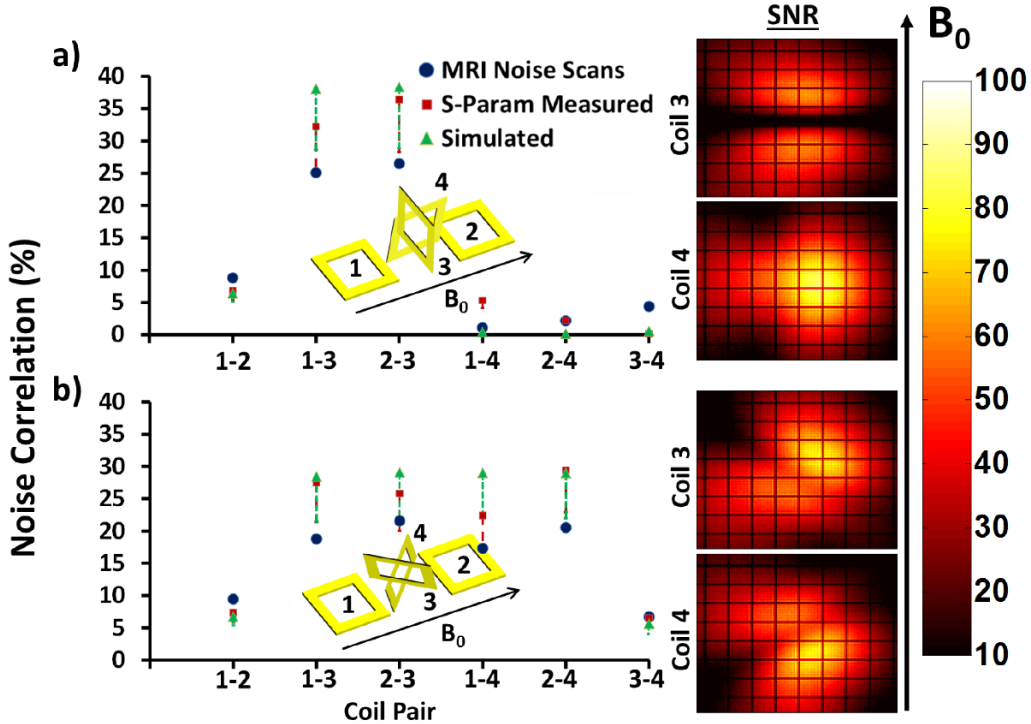


Figure 3.8: Comparison of upright coil orientations in the parallel/perpendicular direction, a), and rotated by  $45^\circ$ , b). Noise correlation from measured (red) and simulated (green) coil impedance parameters and the values found with noise scans are compared for each pair of coils. For simulated and measured values the higher value is the correlation without accounting for the influence of noise from matching circuits and preamplifiers. The lower value is the correlation after correcting for noise added by the matching network and preamplifier. The SNRs are measured in coronal slices 2.5 cm below the phantom surface from the upright elements alone to remove the influence of the surface coil (which is unaltered). The two SNRs of the two arrangements differ by less than 2% (see text).

The average SNR provided by the two upright coils for each orientation was compared in the same field of view defined previously for the single upright coils. The coils in the parallel/perpendicular arrangement (Figure 3.8a) had an average SNR that was 98.3% of that of the coils in the  $45^\circ$  arrangement (Figure 3.8b). This insignificant difference could be due to small differences in positioning and from coupling to surface coils. Consequently the choice of upright coil orientation is a matter of manufacturing preference.

### **3.7. Full Array Results**

Images were taken with the full 8-coil array shown in Figure 3.2 in two orthogonal orientations relative to  $B_0$  to compare SNR and parallel imaging performance with acceleration in both directions. In the first orientation the coil centers align parallel to the  $B_0$  axis and the upright coils that are perpendicular to  $B_0$  are designed to fill an important sensitivity gap in the regions between the surface coils. In this orientation a second set of images is acquired with the upright coils removed to make a comparison with the surface coils alone. Removal of the upright coils ensures that no degradation of surface coil performance can be attributed to their presence. In the second orientation the array is rotated so that the coil centers align perpendicularly to  $B_0$ .

#### **3.7.1. Noise Correlation**

The noise correlation matrix for the complete 8-coil array (measured in the orientation parallel to  $B_0$ ) is shown in Figure 3.9. Large values of noise correlation ( $>0.2$ ) occur between surface coils and adjacent upright coils that are oriented facing each other (the symbol  $| \text{O}$  shows schematically the top view of an upright coil and an adjacent surface coil). Most composite elements (those that are part of the same coil triplet) have very low noise correlation except a slightly elevated value for the middle pair. Most correlations above 0.1 occur between coils in different triplets, thus confirming that coils within each triplet are highly decoupled.

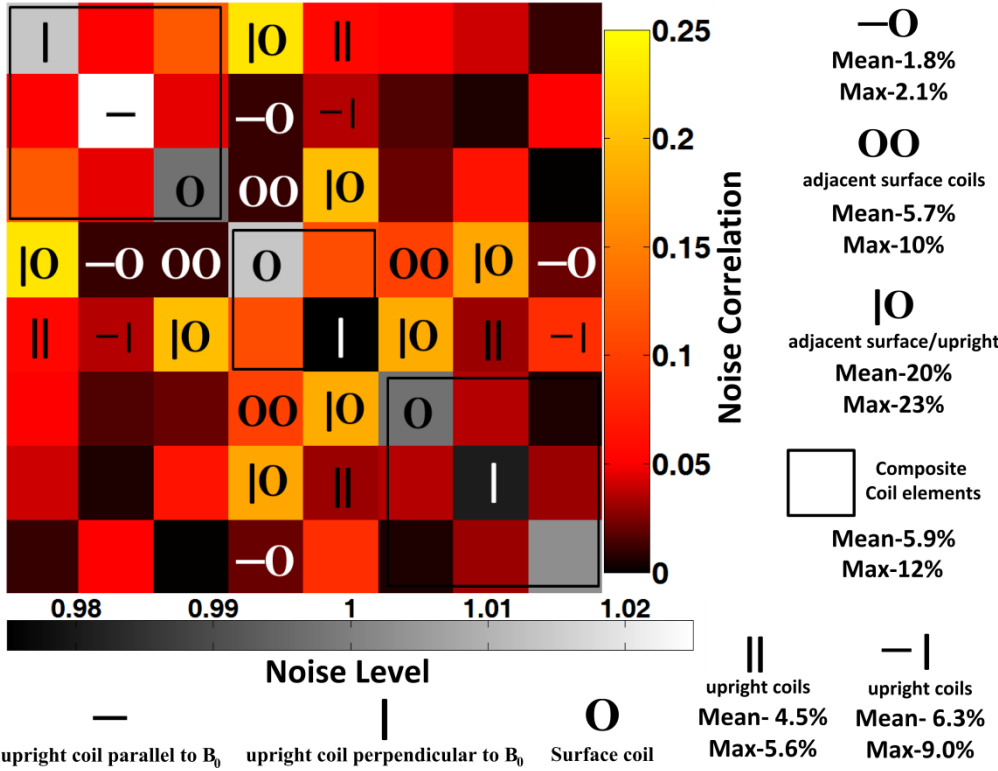


Figure 3.9: Noise correlation matrix (magnitude) for the 8-coil array. The diagonal represents the noise level (variance) for each coil normalized to the mean and symbols are placed over the elements to distinguish types of coil-to-coil interaction. Coils within composite elements are enclosed within square boundaries to indicate the values belonging to each triplet.

The average difference and standard deviation between the magnitudes of the 28 noise correlations measured in the orientations parallel and orthogonal to  $B_0$  is  $0.19\% \pm 0.85\%$ . These minor, insignificant differences in coupling are consistent with small changes in electromagnetic fields and cable routing in the two setups.

### 3.8. SNR improvements

#### 3.8.1. Constant phase combination

Constant phase signal combination was performed to explore the suitability of using hardware signal combiners (e.g., quadrature hybrids) to reduce the number of receiver channels. Figure 3.10(a) shows the SNR normalized to that of a surface coil alone when the signals from a surface coil and an upright coil are combined in a coronal slice below the surface coil with a constant phase of 288 degrees applied

to the signal from upright coils. This angle corresponds to the maximum average SNR increase possible (16%) shown in Figure 3.10(b), and differs only slightly from the 270° angle predicted for quadrature combination. Comparable increases of 21-22% in iSNR have been shown [11] using a microstrip or butterfly coil and a surface coil combined in quadrature. Figure 3.10(b) shows the SNR with constant phase combination, averaged over 3 sagittal and 3 coronal slices, and normalized to that of the surface coil alone (for pixels within the same cuboid defined earlier for single upright coils). When the upright coil is oriented perpendicularly to the magnetic field all constant phase combinations lead to less *average* SNR than with the surface coil alone, even though there are some limited regions with significant SNR gain (Figure 3.10a). For all constant phase combinations the average SNR increase is considerably less than that obtained with optimal SNR combination (at most 16% compared to 48%), thus confirming the necessity of separately receiving and processing the individual channels within one composite coil triplet.

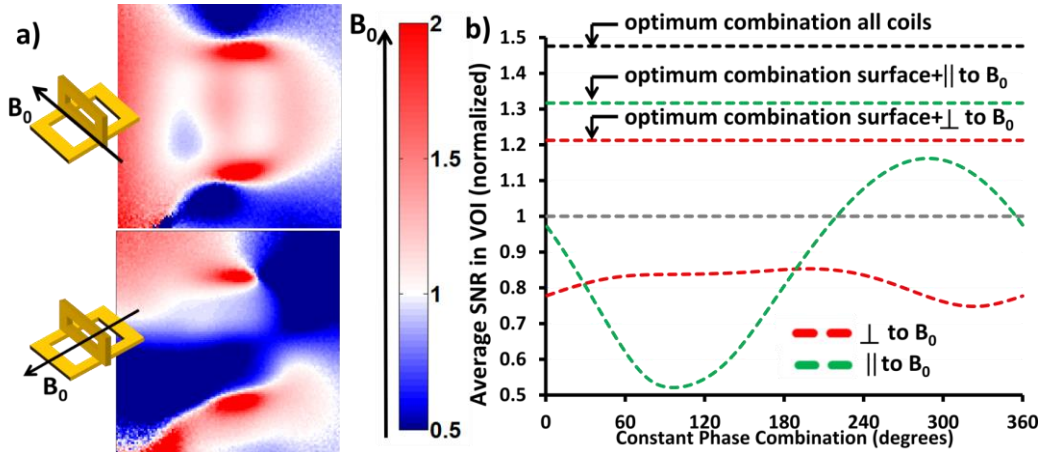


Figure 3.10: (a) Maps of SNR improvement over surface coils alone obtained by combining the signals using a constant phase of 288° throughout the image, with the upright coil parallel to the magnetic field (top) and perpendicular to the magnetic field (bottom). (b) Average image SNR normalized to the average from the surface coil alone for different phase combination angles compared to that obtained with optimal SNR combination.

### 3.8.2. Optimal SNR combination

The sensitivity of the upright coils near the surface is comparable to that of the surface coils and thus contributes significantly to the overall SNR in these regions. The SNR profiles of the composite array are compared to those for the surface coils alone in Figure 3.11. When the array is oriented parallel to  $B_0$  large SNR gains occur in the region between surface coils and beyond the extent of the array along the  $z$  direction where they provide low sensitivity because in these locations the  $B_1$  field is parallel to  $B_0$  (Figure 3.11a and b).

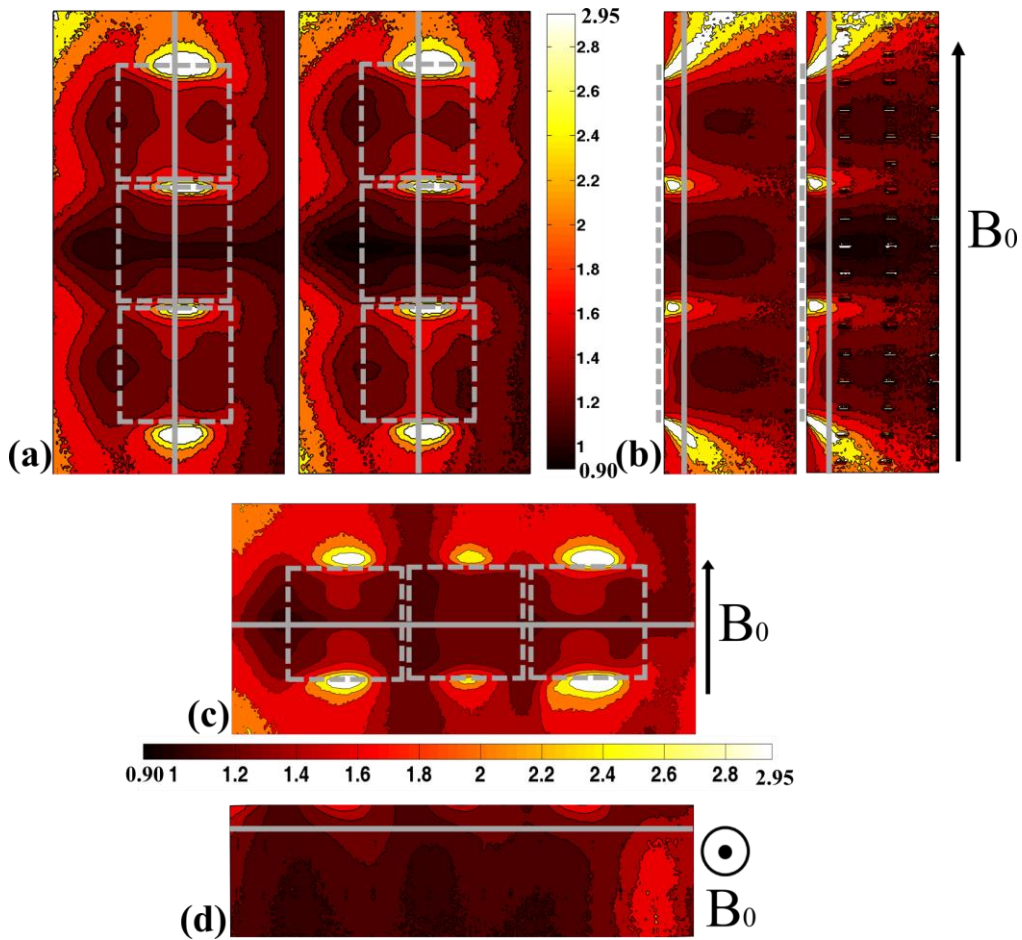


Figure 3.11: Improvement in SNR (optimal combination) relative to that with surface coils alone in (a) a coronal slice and (b) a sagittal slice for surface coil images taken with the full array (left) and taken with upright coils removed (right). The solid gray lines indicate the locations of the slices: 1.2 cm below the surface for the coronal slices and through the center of the array for the sagittal slice. The SNR increase is also shown for the array in the orientation orthogonal to  $B_0$  for (c)

a transverse slice and (d) a coronal slice. Approximate locations of the surface coils are shown as thin dashed lines.

The overall increase in SNR (Table 3-2) is approximately 40% averaged over all pixels contained within a  $280 \times 14 \times 8 \text{ cm}^3$  cuboid (using three sagittal and three coronal slices), and it is approximately 34% when the array is orientated orthogonally to  $B_0$  (averaged over three axial and three coronal slices). Physically removing the upright coils alters these SNR comparisons on average about 3.5% in Table 3-2 or less than 8% when limited to sagittal slices (Figure 3.12), thus confirming that the upright coils do not introduce a substantial amount of coupling and losses. An important result shown in Figure 3.12 is that the improvement in SNR due to the upright coils relative to that from the surface coils alone does not change much with depth into the phantom (averaged across the 3 sagittal slices and  $\pm 10.5 \text{ cm}$  in the direction of  $B_0$ ). The SNR gain due to the upright coils is therefore appreciable throughout the phantom, in contrast to increasing array density by decreasing coil size which leads to SNR improvements that taper off with depth [22-24].

Table 3-2: average SNR comparisons for the 8-coil array: optimal vs. RSS combination and SNR improvement over surface coils only (both with the array oriented parallel and orthogonal to  $B_0$ )

	Average SNR increase in $280 \times 14 \times 8 \text{ cm}^3$ volume
Parallel orientation	Optimal vs. RSS combination (full array)
	2.5%
	Full array vs. surface coils only (upright coils removed)
	36.9%
	Full array vs. surface coils only (upright coils in place)
	40.4%

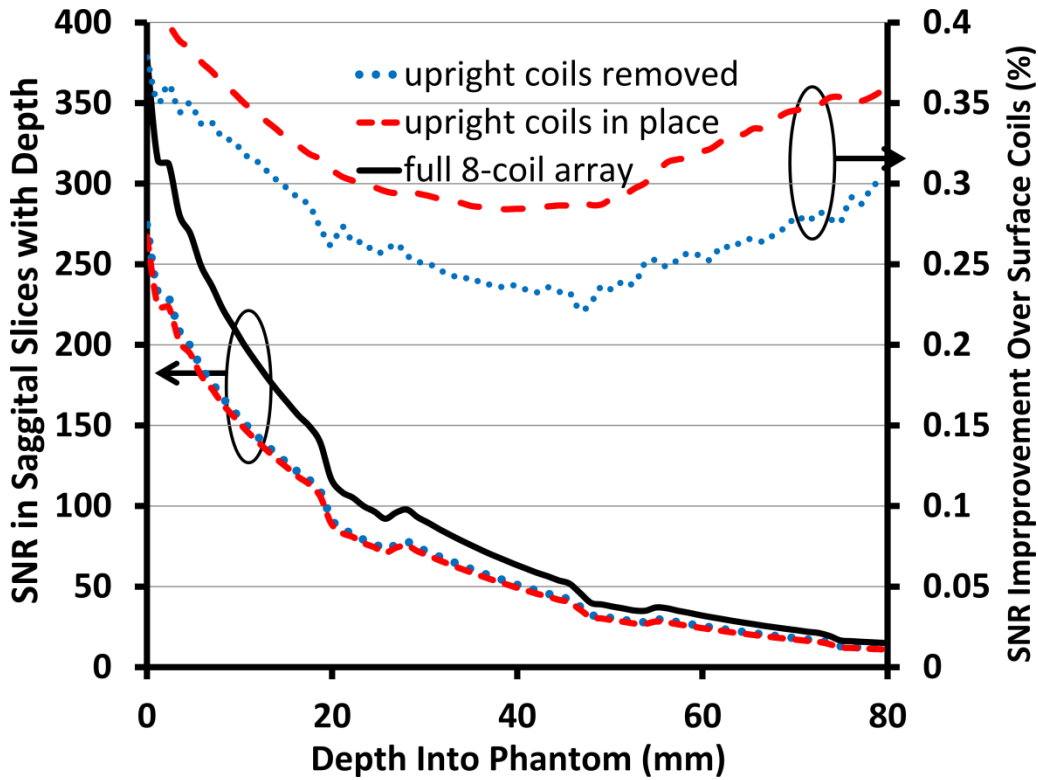


Figure 3.12: optimal SNR as a function of depth into the phantom (left-hand scale) of the 8-coil array or surface coils alone averaged along the direction of  $B_0 \pm 10.5$  cm in 3 sagittal slices (centred with array  $\pm 2.5$  cm in the lateral direction). The SNR of the full array is compared to that from the surface coils in the presence or absence of the upright coils (right-hand scale), and shows that the SNR improvement due to the upright coils does not taper off to zero with depth.

### 3.8.3. Effect of Noise Correlation

The importance of including noise correlation in image combination is illustrated in Figure 3.13, where the SNR obtained using RSS combination is compared to that using optimal combination (wRSS). The loss of SNR incurred by ignoring noise correlation is as high as 6%, and is maximal below the central composite coil, as expected from the relatively large noise correlation (average of 16% between the central surface coil and other non-orthogonal coils) between its elements and neighboring elements (Figure 3.9). The SNR loss, averaged over the same volume as the SNR in section 3 is only 2.5% (Table 3-2) as a consequence of the limited noise correlation between most elements of the array. In large coil arrays with significant noise covariance between elements the SNR difference between RSS and optimum combination reach differences of 20% or higher [24]; the low

noise correlation between elements of composite arrays may mitigate this degradation.

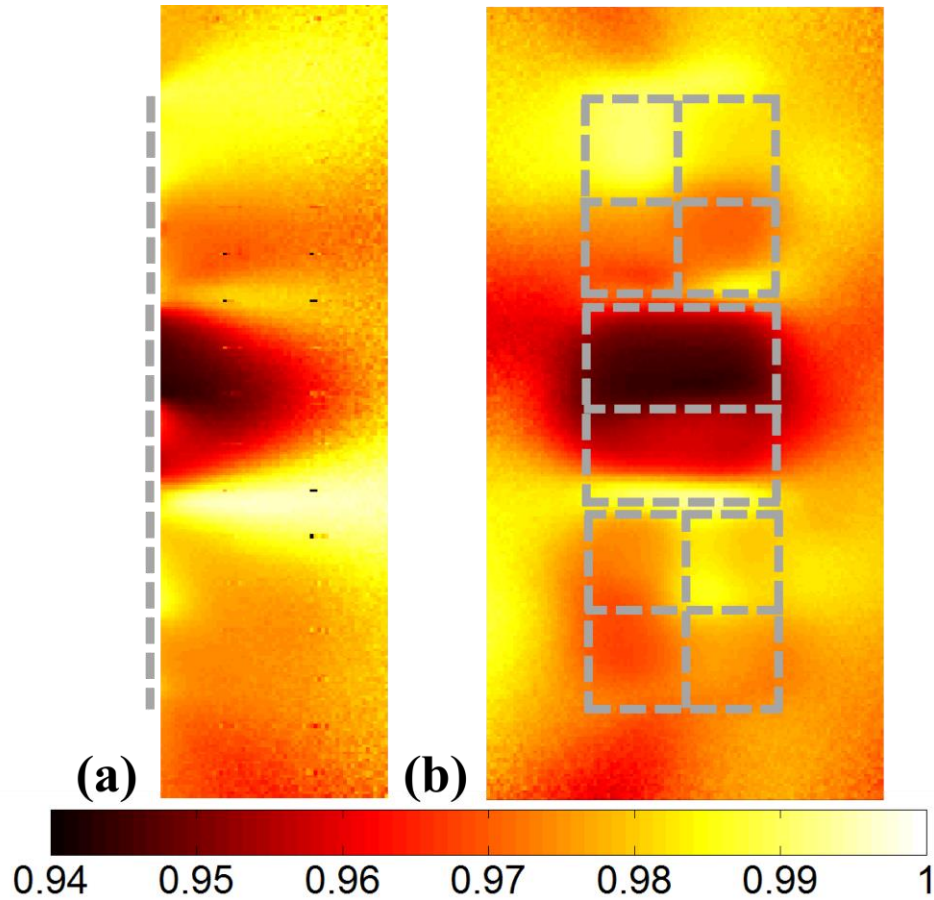


Figure 3.13: SNR of RSS combination relative to that using optimal combination (wRSS) in (a) a coronal slice and (b) a sagittal slice. The SNR loss using RSS is as high as 6% below the central composite coil and is attributed to the significant noise correlation between it and the other elements (especially the adjacent upright elements orthogonal to  $B_0$ ).

### 3.9. Parallel Imaging Performance

Parallel imaging performance is illustrated in Figure 3.14, which contains the  $1/g$ -factor maps of the surface coils alone and those of the full array in the same slices of Figure 3.11. When the array is oriented parallel to  $B_0$  and only surface coils are used, high  $g$ -factors occur in the regions between the coils because of their similar sensitivities. When upright coils are included the  $g$ -factor remains close to 1 everywhere except at depths  $> 7$  cm (one coil diameter) and is consistently

improved near the surface over that for surface coils alone. Much of this improvement in parallel imaging performance is due to the upright coils oriented perpendicular to  $B_0$  because their sensitivities are highly complementary to those of the surface coils. The mean and maximum g-factor values for the slices shown in Figure 3.14 are listed in Table 3-3. The mean g factor is below 1.2 for acceleration factors up to 5, which is commonly taken as the limit above which parallel imaging is not advantageous [25]. Achieving similar performance with the surface coils alone limits the acceleration factor to 2.

Table 3-3: average and maximum g-factors for the slices shown in Figure 3.14 using surface coils only or with the full 8-coil array for 1-D accelerations in the direction parallel to the array

SENSE Acceleration	g factor mean/max			
	Array $\parallel B_0$		Array $\perp B_0$	
	Complete array	Surface coils only	Complete array	Surface coils only
<b>2</b>	1.00/1.09	1.05/2.07	1.01/1.21	1.04/1.73
<b>3</b>	1.01/1.42	1.28/78.0	1.16/2.25	1.71/132
<b>4</b>	1.07/1.67	$\infty$	1.50/2.94	$\infty$
<b>5</b>	1.22/3.80	$\infty$	2.19/7.94	$\infty$
<b>6</b>	1.60/6.95	$\infty$	3.64/21.0	$\infty$

When the array is oriented orthogonally to  $B_0$ , the g-factors are higher both with the full coil array and with the surface coils alone. The inferior parallel imaging performance in this orientation is due in part to the alignment of the slice with the symmetry plane of the array, in which the upright coils that are oriented orthogonally to  $B_0$  do not have significant sensitivity, thus limiting their effectiveness. The surface coil sensitivity profiles also overlap significantly more in this orientation and the upright coils have lower sensitivity between the surface coils.

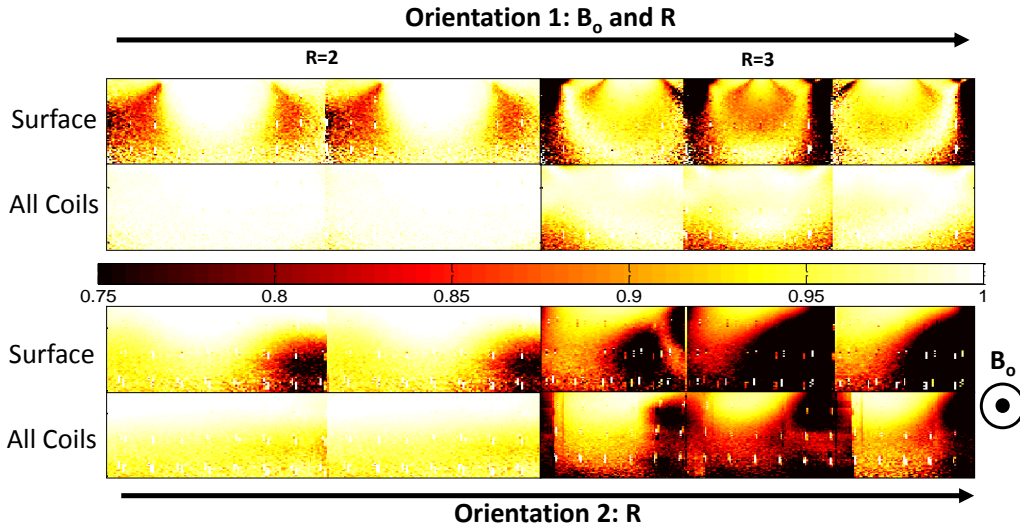


Figure 3.14:  $g^{-1}$ -factor maps for acceleration factors of 2 and 3 (sagittal view when the array is oriented parallel to  $B_0$ , and axial view in the orthogonal orientation) using only the surface coils or the complete 8-coil array. Arrows indicate direction of  $B_0$  and acceleration (phase encode direction). An acceleration factor of 4 would be impossible with the surface coils only but is readily achievable with the composite coil array with a mean  $g$ -factor of only 1.07 (Table 3-3).

### 3.10. Conclusion

The overall SNR improvement of a composite array over that of a surface coil (47% from Figure 3.10) and that of the overall results from the 8 coil array (34-40% depending on orientation from table 2) appear to be consistent with results predicted from simulations at 128MHz [2]. However, the coil and array sizes were smaller (5.5cm vs. 7cm side length), the phantom electrical properties were different, and coupling and noise from matching/preamplifiers were not included.

This study presents design criteria and imaging performance results for composite coils created by combining standard surface coils with upright coils that capture additional orthogonal field components. This is an alternative method of increasing channel density that avoids creating an array of small surface coils all of which operate in the coil-dominated noise regime. Composite coils allow the creation of high-density arrays that avoid some of the challenges of managing coupling encountered when surface coil size is reduced to accommodate more elements, and also allow reception with standard channel density by ignoring the

data acquired by the upright coils and using only the data from the surface coil elements.

Coupling and noise correlation within each composite coil triplet are negligible as predicted by the symmetrical coil arrangement. Between triplets coil interactions are stronger but managed effectively by preamp decoupling and optimal SNR reconstruction. Cable routing is somewhat more challenging than in traditional arrays due to the three-dimensional layout, but satisfactory arrangements are possible. The overall coupling and noise correlation of the composite array are comparable to those of standard surface coil arrays.

As predicted by previous simulations [3], capturing the components of flux parallel to the surface results in SNR gains and increased sensitivity in regions where surface coils alone have low sensitivity. These SNR gains are achieved in spite of the limited body loading of the upright coils and sometimes higher noise correlations between elements of different triplets. Pixelwise combination is required, since a fixed phase combination such as that achievable with hardware combiners (e.g., quadrature hybrids) does not offer SNR benefits throughout the field of view. Average SNR improvements of around 40% can be expected over that of surface coils alone. Furthermore, these SNR gains remain high deep in the phantom (Figure 3.12) which confirms the improved completeness of composite coils over arrays of surface coils alone. The largest improvements are seen in regions where the surface coils have low sensitivity therefore composite coils are also an effective way to increase the FOV with good SNR compared to surface coils alone.

While it is counter-intuitive that upright coils should contribute much to the SNR improvement because of their low body loading, they do pick up less body noise than surface coils while their sensitivity is similar to that of surface coils. At higher frequencies sample losses are expected to become dominant also in the upright coils, and consequently the SNR advantages of composite coils may be even more pronounced at high fields which is investigated in Chapter 4.

Parallel imaging performance also improves over surface coils alone, especially when the array and acceleration are oriented parallel to  $B_0$ . Upright coils

perpendicular to  $B_0$  have sensitivity patterns that are more complementary to those of the surface coils when acceleration is in the direction of  $B_0$ , despite providing an overall lower SNR increase when combined with surface coils than the upright coils oriented parallel to  $B_0$  (Figure 3.10). The average and maximum  $g$  factors in the slices shown in Figure 3.14 are substantially lower for the composite array thus allowing accelerations that would not be achievable or practical with surface coils alone.

## Bibliography

- [1] F. Wiesinger, P. Boesiger and K. P. Pruessmann, "Electrodynamics and ultimate SNR in parallel MR imaging," *Magn. Reson. Med.*, vol. 52, pp. 376-390, 2004.
- [2] Z. J. Wang, "Improving SNR of RF coils using composite coil elements," *NMR Biomed.*, vol. 22, pp. 952-959, 2009.
- [3] W. Zhiyue J., "Towards a complete coil array," *Magn. Reson. Imaging*, vol. 26, pp. 1310-1315, 2008.
- [4] W. A. Edelstein, G. H. Glover, C. J. Hardy and R. W. Redington, "The intrinsic signal-to-noise ratio in NMR imaging," *Magn. Reson. Med.*, vol. 3, pp. 604-618, 1986.
- [5] M. F. Mueller, T. Lanz, F. Breuer, M. A. Griswold and P. M. Jakob, "Three-dimensional quadrature array coil elements for improved parallel magnetic resonance imaging performance at 1.5 Tesla," *Concepts Magn. Reson.*, vol. 38A, pp. 61-73, 2011.
- [6] M. A. Ohliger, R. L. Greenman, R. Giaquinto, C. A. McKenzie, G. Wiggins and D. K. Sodickson, "Concentric coil arrays for parallel MRI," *Magn. Reson. Med.*, vol. 54, pp. 1248-1260, 2005.
- [7] D. A. Molyneaux and A. H. Qureshi, "Quadrature coil system for simultaneous reception," *Magnetics, IEEE Transactions on*, vol. 29, pp. 2470-2472, 1993.
- [8] P. B. Roemer, W. A. Edelstein, C. E. Hayes, S. P. Souza and O. M. Mueller, "The NMR phased array," *Magn. Reson. Med.*, vol. 16, pp. 192-225, 1990.
- [9] M. A. Ohliger, P. Ledden, C. A. McKenzie and D. K. Sodickson, "Effects of inductive coupling on parallel MR image reconstructions," *Magn. Reson. Med.*, vol. 52, pp. 628-639, 2004.
- [10] S. M. Wright and L. L. Wald, "Theory and application of array coils in MR spectroscopy," *NMR Biomed.*, vol. 10, pp. 394-410, 1997.
- [11] A. Kumar and P. Bottomley, "Optimized quadrature surface coil designs," *Magnetic Resonance Materials in Physics, Biology and Medicine*, vol. 21, pp. 41-52, 2008.

- [12] C. Chen, D. I. Hoult and v, *Biomedical Magnetic Resonance Technology*. Bristol: Adam Hilger, 1989.
- [13] D. M. Peterson, "Impedance matching and baluns," in *Encyclopedia Magnetic Resonance*Anonymous John Wiley & Sons, Ltd, 2011, .
- [14] P. Mansfield and P. G. Morris, *NMR Imaging in Biomedicine: Supplement 2 Advances in Magnetic Resonance*. New York: Academic Press, 1982.
- [15] B. Keil, G. C. Wiggins, C. Triantafyllou, L. L. Wald, F. M. Meise, L. M. Schreiber, K. J. Klose and J. T. Heverhagen, "A 20-channel receive-only mouse array coil for a 3 T clinical MRI system," *Magn. Reson. Med.*, vol. 66, pp. 582-593, 2011.
- [16] A. Reykowski, S. M. Wright and J. R. Porter, "Design of Matching Networks for Low Noise Preamplifiers," *Magn. Reson. Med.*, vol. 33, pp. 848-852, 1995.
- [17] S. M. Wright, "Full-wave analysis of planar radiofrequency coils and coil arrays with assumed current distribution," *Concepts Magn. Reson.*, vol. 15, pp. 2-14, 2002.
- [18] I. ANSYS, "Ansoft HFSS - User Guide," 2008.
- [19] J. G. Och, "Acceptance testing of magnetic resonance imaging systems: Report of AAPM Nuclear Magnetic Resonance Task Group No. 6" *Med. Phys.*, vol. 19, pp. 217, 1992.
- [20] X. Zhang, K. Ugurbil and W. Chen, "Microstrip RF surface coil design for extremely high-field MRI and spectroscopy," *Magn. Reson. Med.*, vol. 46, pp. 443-450, 2001.
- [21] A. M. Mauder, M. Daneshmand, P. Mousavi, B. G. Fallone and N. De Zanche, "Parasitic capacitance in MRI coil arrays: Models and application to Array decoupling," in *Microwave Symposium Digest*, 2013, .
- [22] S. M. Wright, "Receiver loop arrays," in *Encyclopedia Magnetic Resonance*Anonymous John Wiley & Sons, Ltd, 2011, .
- [23] F. Wiesinger, N. DeZanche and K. Pruessman, "Approaching Ultimate SNR with Finite Coil Arrays," *Proc. Intl. Soc. Mag. Reson. Med.*, vol. 13, pp. 627, 2005.
- [24] G. C. Wiggins, J. R. Polimeni, A. Potthast, M. Schmitt, V. Alagappan and L. L. Wald, "96-Channel receive-only head coil for 3 Tesla: Design optimization and evaluation," *Magn. Reson. Med.*, vol. 62, pp. 754-762, 2009.
- [25] Larkman David J., "Parallel Imaging in Clinical MR Applications; The g-Factor and Coil Design" *Medical Radiology*, pp. 37 - 48, 2007.

# **Chapter 4**

## **Comparison of Composite and Surface Coil Arrays in Approaching the Ultimate Signal to Noise**

### **4.1. Introduction**

In this chapter we investigate, whether it is a better strategy to use composite coils or an equivalent number of surface coils covering the same volume/surface area. There is a threshold level where reducing the size of surface coils in order to increases the number of array elements reduces SNR because the noise contribution of the coil and coil components increases greater than the relative sensitivity increase[1, 2]. Even before this point the SNR at greater depth will suffer at the expense of increases at the surface as seen in reference [3]. Studies have shown that for higher MRI frequencies ( $>3\text{T}$ ) it is necessary to have coils with curl-free fields (produced by electric-dipole like currents) as well as divergence free fields (produced by magnetic-dipole like currents) to approach the uiSNR [4, 5]. Therefore, for the purpose of increasing SNR in large element arrays, especially at greater depth, composite coil arrays will be beneficial since upright coils can produce current patterns on the surface similar to electric dipole (curl-free) patterns. In addition, composite coils provide the already known benefits of natural decoupling and enhanced parallel imaging performance [6] due to their complementary sensitivity patterns [7, 8] as shown in Chapter 2.

In this chapter large surface and composite coil arrays covering the surface of a sphere are simulated. The optimally combined SNR is calculated from HFSS simulated fields and impedance matrices that include coil conductor, radiation and dielectric losses at 128MHz and 300MHz and this is compared to the analytic uiSNR. The additional loss of matching networks and preamplifiers is included and the impact on array performance is compared. The results show the potential benefits and limitations of using composite coils instead of surface coils in receive arrays; results also apply to arrays using other coils naturally decoupled from

surface coils to provide complementary sensitivities (ie. vertical, butterfly, dipole antenna and microstrip coils). This chapter also resolves important questions concerning coil array design: the importance of decoupling in arrays, the best ways to approach the uiSNR with finite coil arrays and the impact of complementary phase sensitivity and noise statistics on the matching network and preamplifier noise in the final recombination.

## 4.2. Theory

After simulation of the magnetic field produced per unit current and impedance matrices of coils the open circuit signal voltage using equation (1.25) and open-circuit noise voltage covariance ( $4kBT\mathbb{R}(\mathbf{Z})$ ) are known, so calculation of the final output noise and signal can be found as follows. In addition, the analytical calculation of the uiSNR in a sphere is summarized in terms of the electrical properties of the sphere.

### 4.2.1. Noise and Signal Calculation

The analysis of preamplifier noise propagation in a multiport system has been developed using S-Parameters in the field of MIMO antennas [9-11] and with a Z-Parameter representation of the coil array plus matching networks [12]. These methods rely on the equivalent two-port noise source [12] or noise wave representation of preamplifiers [11]. The wave port representation is identical to equation (1.23) if the coils are the only noise source with lossless matching networks and preamplifiers.

Using the noise wave representation from reference [11] with the network illustrated in Figure 4.1 the voltage covariance and the signal voltage at the output of preamplifiers is given by

$$\begin{aligned}\mathbf{v}_s &= \mathbf{Q}\mathbf{G}_0\widehat{\mathbf{v}}_s \\ \mathbf{\Psi} &= \mathbf{Q}(\mathbf{\Psi}_p)\mathbf{Q}^H\end{aligned}\tag{4.1}$$

where  $\widehat{\mathbf{v}}_s$  is the open circuit signal voltages at the coil ports given in equation (1.26),  $\mathbf{\Psi}_p$  is the voltage covariance at the preamplifier input terminals. In reference [11] matrices  $\mathbf{G}_0$  relates the open circuit voltages at the coil terminals to the voltage at

the preamplifier input, while  $\mathbf{Q}$  relates this voltages at the preamplifier input to output, and they are given by

$$\mathbf{Q} = \sqrt{Z_0}(\mathbf{I} + \mathbf{\Gamma}_L) \left[ (\mathbf{I} - \mathbf{\Gamma}_0 \mathbf{S}_{A11})(\mathbf{S}_{A21}^{-1})(\mathbf{I} - \mathbf{\Gamma}_L \mathbf{S}_{A22}) - \mathbf{\Gamma}_0 \mathbf{S}_{A11} \mathbf{\Gamma}_L \right]^{-1} \quad (4.2)$$

$$\mathbf{G}_0 = \frac{1}{2\sqrt{Z_0}} \mathbf{S}_{21} (\mathbf{I} - \mathbf{S}_{RR} \mathbf{S}_{11})^{-1} (\mathbf{I} - \mathbf{S}_{RR})$$

$\mathbf{S}_{11}, \mathbf{S}_{12}, \mathbf{S}_{21}, \mathbf{S}_{22}$  are the S-parameters of the matching network,  $\mathbf{S}_{RR}$  is the scattering matrix of the array and  $\mathbf{S}_{A11}, \mathbf{S}_{A12}, \mathbf{S}_{A21}, \mathbf{S}_{A22}$  are the S-parameters of the preamplifiers, which are usually diagonal if coupling is appropriately managed, e.g., by shielding. The covariance matrix at the preamplifier terminals ( $\Psi_p$ ) without matching network noise ( $\Psi_n$ ), with matching network noise ( $\Psi_m$ ) [13] and with matching network and N-port preamplifier noise ( $\Psi_\eta$ ) are given by

$$\begin{aligned} \widehat{\Psi_n} &= 4Bk_b T_0 \mathbf{G}_0 \mathbb{R}(\mathbf{Z}) \mathbf{G}_0^H \\ \Psi_m &= Bk_b T_0 (\mathbf{I} - \mathbf{\Gamma}_0 \mathbf{\Gamma}_0^H) \\ \Psi_\eta &= Bk_b (T_\alpha \mathbf{I} + T_\beta \mathbf{\Gamma}_0 \mathbf{\Gamma}_0^H - T_\gamma^* \mathbf{\Gamma}_0^H - T_\gamma \mathbf{\Gamma}_0) + \Psi_m, \end{aligned} \quad (4.3)$$

where  $B$  is the bandwidth,  $T_\alpha, T_\beta$  and  $T_\gamma$  are the amplifier noise wave parameters which have units of temperature and in terms of the forward travelling ( $\mathbf{a}_\eta$ ) and reverse travelling ( $\mathbf{b}_\eta$ ) noise waves produced by the preamplifier at the input are given by

$$\begin{aligned} \mathbf{E}\{\mathbf{a}_\eta \mathbf{a}_\eta^*\} &= Bk_b T_\alpha \\ \mathbf{E}\{\mathbf{b}_\eta \mathbf{b}_\eta^*\} &= Bk_b T_\beta \\ \mathbf{E}\{\mathbf{a}_\eta \mathbf{b}_\eta^*\} &= Bk_b T_\gamma^*. \end{aligned} \quad (4.4)$$

The derivation of these parameters in terms of the preamplifier noise parameters are given in reference [14, 15].  $\mathbf{\Gamma}_0$  is the scattering matrix seen looking into the matching networks at the preamplifier terminals and is given by

$$\mathbf{\Gamma}_0 = \mathbf{S}_{22} + \mathbf{S}_{21} (\mathbf{I} - \mathbf{S}_{RR} \mathbf{S}_{11})^{-1} \mathbf{S}_{RR} \mathbf{S}_{12}. \quad (4.5)$$

If the preamplifiers are assumed to add noise individually to each channel based on the optimum individual noise figure the final noise covariance at the preamplifier output is given by

$$\boldsymbol{\Psi}_{diag} = \boldsymbol{Q}(\boldsymbol{\Psi}_m)\boldsymbol{Q}^H + \text{diag}(\boldsymbol{Q}(\boldsymbol{\Psi}_m)\boldsymbol{Q}^H)(\boldsymbol{F}_{pre} - \boldsymbol{I}), \quad (4.6)$$

where  $\boldsymbol{F}_{pre}$  is the diagonal matrix containing the noise factors of the preamplifiers.

For the purpose of comparing the arrays in this analysis  $\boldsymbol{\Psi}_{diag}$  is used to evaluate the effect of preamplifier noise on optimally recombined SNR of arrays, which is consistent with analysis done in other works [16]. The importance of preamplifier noise that is produced at the input and transferred into the array still needs requires further investigation [17], so the difference between using  $\boldsymbol{\Psi}_{diag}$  and  $\boldsymbol{\Psi}_\eta$ , the covariance resulting from using the N-port noise wave representation is compared. Assuming the noise contribution is only to individual channels proves to be good approximation under certain conditions, since the majority of noise added by amplifier arises from the thermally generated channel noise on the output side of the preamplifier [18], and only a negligible amount is transmitted to the input at the relatively low frequencies used in MRI.

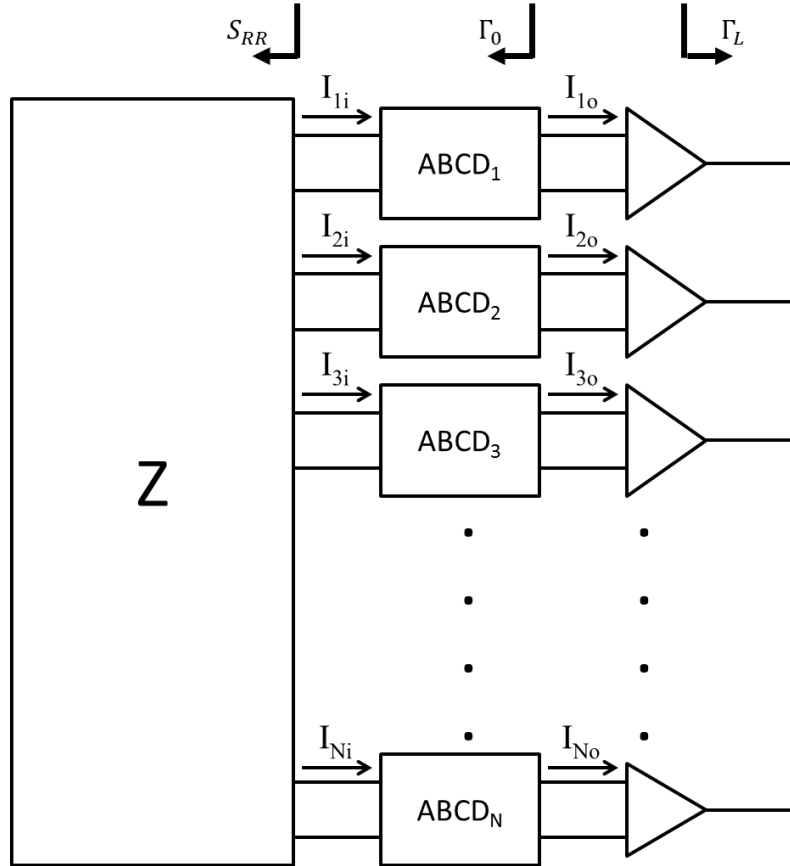


Figure 4.1: N-port representation of coil array impedance matrix ( $\mathbf{Z}$ ), matching networks and preamplifiers,

#### 4.2.2.uiSNR in sphere calculation

One method of calculating the ultimate intrinsic Signal to Noise Ratio (uiSNR) within a sphere with homogeneous electrical properties is finding the optimum combination of a hypothetical complete basis set of magnetic fields constrained to be solutions of Maxwell's equations within the sphere. The main result is repeated here as follows [19-21].

The terms for the receive sensitivity vector of these sources is given by,

$$\begin{aligned} \mathbf{s}(\mathbf{r}) &= \begin{pmatrix} S^{E,x} - iS^{E,y} \\ S^{M,x} - iS^{M,y} \end{pmatrix}, \text{ where} \\ \mathbf{s}_{lm}^{E,x}(\mathbf{r}) &= j_1(k_0 r_p) [\mathbf{X}_{lm}(\theta_p, \phi_p)]_x \\ \mathbf{s}_{lm}^{M,x}(\mathbf{r}) &= -\frac{i}{k_0 r_p} \left. \frac{\partial[j_1(k_0 r)]}{\partial r} \right|_{r=r_p} [\widehat{\mathbf{r}_p} \times \mathbf{X}_{lm}(\theta_p, \phi_p)]_x + \frac{\sqrt{l(l+1)}}{k_0 r_p} j_1(k_0 r) Y_{lm}(\theta_p, \phi_p) [\widehat{\mathbf{r}_p}]_x \end{aligned} \quad (4.7)$$

$\mathbf{s}_{lm}^{E,x}(r_p)$  and  $\mathbf{s}_{lm}^{M,x}(r_p)$  are defined similarly to  $\mathbf{s}_{lm}^{E,x}(\mathbf{r})$  and  $\mathbf{s}_{lm}^{M,x}(\mathbf{r})$ , replacing the x-components with y-components. The variables used are:  $r_p, \theta_p, \phi_p$  that denote the position of the calculated magnetic field at point  $p$ ,  $k_0$  is the complex wave number,  $j_l$  is the  $l$ -th spherical Bessel function,  $\mathbf{X}_{lm}$  and  $Y_{lm}$  are the vector and scalar spherical harmonic functions, respectively, for degree  $l$  and order  $m$ . The degree used in calculations is 80, which is found to be sufficient to converge to the solution with infinite basis functions demonstrated in reference [21] resulting in  $2(80+1)^2$  basis functions. The diagonal covariance matrix is calculated as

$$\begin{aligned} \boldsymbol{\Psi} &= B k_b T_0 \sigma \left| \frac{\omega \mu}{k_0} \right|^2 \begin{pmatrix} \boldsymbol{\psi}^E & 0 \\ 0 & \boldsymbol{\psi}^M \end{pmatrix}, \text{ where} \\ \boldsymbol{\psi}_{(l,m),(l',m')}^E &= \delta_{l,l'} \delta_{m,m'} \left| \frac{1}{k_0} \right|^2 \int_{r=0}^{FOV/2} \left[ \left| \frac{\partial[j_1(k_0 r)]}{\partial r} \right|^2 + l(l+1) |j_1(k_0 r)|^2 \right] dr \\ \boldsymbol{\psi}_{(l,m),(l',m')}^M &= \delta_{l,l'} \delta_{m,m'} \int_{r=0}^{FOV/2} r^2 |j_1(k_0 r)|^2 dr. \end{aligned} \quad (4.8)$$

where  $\sigma$ , the conductivity, is included to scale by the same amount of power dissipation as would be simulated or measured by a coil, and  $\delta_{ij}$  is the Kronecker delta. The optimum combined SNR is given by

$$\text{SNR} = B_0 \sqrt{\mathbf{s}^H \boldsymbol{\Psi}^{-1} \mathbf{s}} \frac{1}{\sqrt{B k_b T_0}} \frac{\Omega}{T^2} \quad (4.9)$$

The  $B_0$  factor is applied to account for the voltage induced on the coil being due to the change in RF magnetic field proportional to the Larmor frequency (and therefore  $B_0$ ). An additional term of  $B_0$  that usually accounts for the thermally-polarized magnetization that is proportional to field strength [22] is excluded. In this manner SNR at different frequencies can be compared fairly on the same scale. The additional factor of  $\Omega/(T^2\sqrt{Bk_bT_0})$  makes the relative SNR that will be compared a unit-less quantity. The g-factor is also calculated using equation (1.22) with these values of sensitivity and covariance matrices. The uiSNR and g-factors with the complete coil approximation are compared to the simulated values in the composite and surface coil arrays.

### **4.3. Methods**

The dimensions and parameters of 3-, 18-, 36- and 54-coil arrays are detailed. The method of comparing the arrays are also given: coil coupling, noise correlation, optimally combined SNR and g-factor calculation and comparison of noise added by matching networks and preamplifiers.

#### **4.3.1. Three Coil Array Comparison**

The size of the three-coil arrays is chosen so that the upright coils and surface coils are body loaded. The surface coil array, made from copper strip 5mm wide and 0.04mm thick copper strip, covers roughly the same surface area as the composite array (with 12cm diameter surface coil), made from 1.6mm diameter silver wire. The details of capacitor topography and port placement on the coils are shown in Figure 4.2. The built coil arrays are also shown in Figure 4.2c.

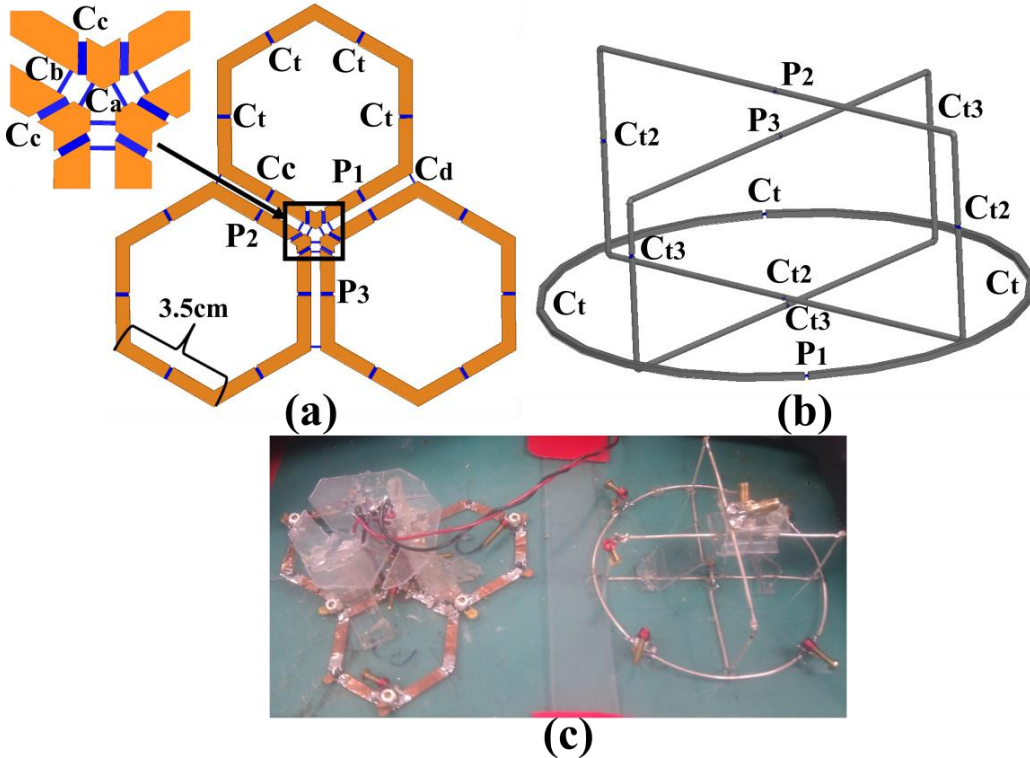


Figure 4.2: (a) Composite coil array design including labels of decoupling and tuning capacitors (blue rectangles) on one coil and (b) surface coil array design with the tuning capacitor locations next to labels. The built arrays are shown in (c), which has the same dimensions as the simulated coils.

Tuning capacitors are placed to remove the inductive reactance of the coils and to break them up into lengths less than  $\lambda/20$  to reduce the radiation resistance and dielectric losses. The capacitors labeled  $C_a$ ,  $C_b$ ,  $C_c$ , and  $C_d$  are used together to remove the mutual resistance and reactance, while  $C_t$  removes the self-reactance in the surface coil array design. The values used in simulation are 33, 130, 70 42 and a combined series tuning capacitance of 15pF, while they are approximately 33, 33-108 (includes varactor), 73-79, 68 and a combined series tuning capacitance of 17-19pF with two series  $C_t$  capacitors, in measurement.

The average simulated self-resistance of coils is  $2.5\Omega$  and measured is  $1.92\Omega$  with close to zero mutual impedance in both cases. Many choices of decoupling capacitors will result in zero mutual impedance with different self-impedance values and the additional factor of equivalent series resistance of capacitors and varactors result in differences between the simulated and measured values required for tuning capacitors and therefore the resulting self-impedance as

well. However, as Chapter 2 indicates differences in the decoupling capacitors result in very little change in the combined SNR. Diode varactors (ZC836BTA, Zetex Semiconductors) incorporated with capacitor  $C_b$  allows for variable decoupling with changing load. The combined series capacitance of  $C_t$ ,  $C_{t2}$ ,  $C_{t3}$  capacitors in Figure 4.2b are 6, 7.3 and 7.3pF respectively for simulation and 5-5.3pF, 6.7-7.4pF and 6.5-6.9pF respectively in measurement.

The simulated self-impedance of coils with these capacitance values is  $24.3+48.7j \Omega$ ,  $2.47+22.1j \Omega$ , and  $2.68+41.3j \Omega$ , while the measured self-impedance when tuned for matching networks is  $25.0+42.5j \Omega$ ,  $3.2 \Omega$  and  $3.8 \Omega$  for the surface coil and upright coils with 4.5cm and 5.5cm height respectively. The self-impedance of the surface coil has reactance since the matching network in Figure 1.2b requires remaining inductance. There is a 5% variation in all of the capacitors used for measurement and an approximate  $0.03-0.07\Omega$  ESR as well. The simulated upright coils lower resistance is likely due to variation in the conductivity of the phantom and ESR of capacitors.

The matching networks used for all coils except the 12cm-diameter surface coil is the quarter wave balun shown in Figure 1.2a, the 12cm-diameter coil uses the matching network in Figure 1.2b. Diode varactors (SVC389, Sanyo Semiconductors) used to tune  $C_{m2}$  in the matching network of the 12cm-diameter allows for variable matching with changes in loading.

### 4.3.2. Coils on a Sphere

In this analysis 128MHz and 300MHz are used since this range constitutes a transition from near to far-field behavior [21]. There is also a related transition from linear to greater than linear growth in uiSNR [21] and from coil-dominated loading to largely body dominated loading in composite coils.

In order to effectively compare composite array and those composed of just surface coils in terms of obtainable SNR and parallel imaging increasingly large arrays are simulated covering a sphere with approximately the same size of a human head (180cm diameter) with the coils spaced one centimeter away. For each array a set of angles is found in MATLAB using a numerical optimization routine that attempts to space coils equally apart on the sphere. Some array sizes provide better

surface density packing than others, (such as 6,12 or 20 count coil array sizes where points can all be equally spaced apart), which can lead to discontinuities in the g-factor of SNR in some regions [22], but by averaging over the volume these discontinuities are avoided.

The center of simulated coils are placed at these points in HFSS and then the radius of coils is chosen to be the largest possible without coils intersecting. Surface coils are modeled as polygons with 12 sides and upright coils are composed of straight segments as shown in Figure 4.3. The center and ends of the section of upright coils closest to the sphere are 1cm from the surface and are joined by a linear section.

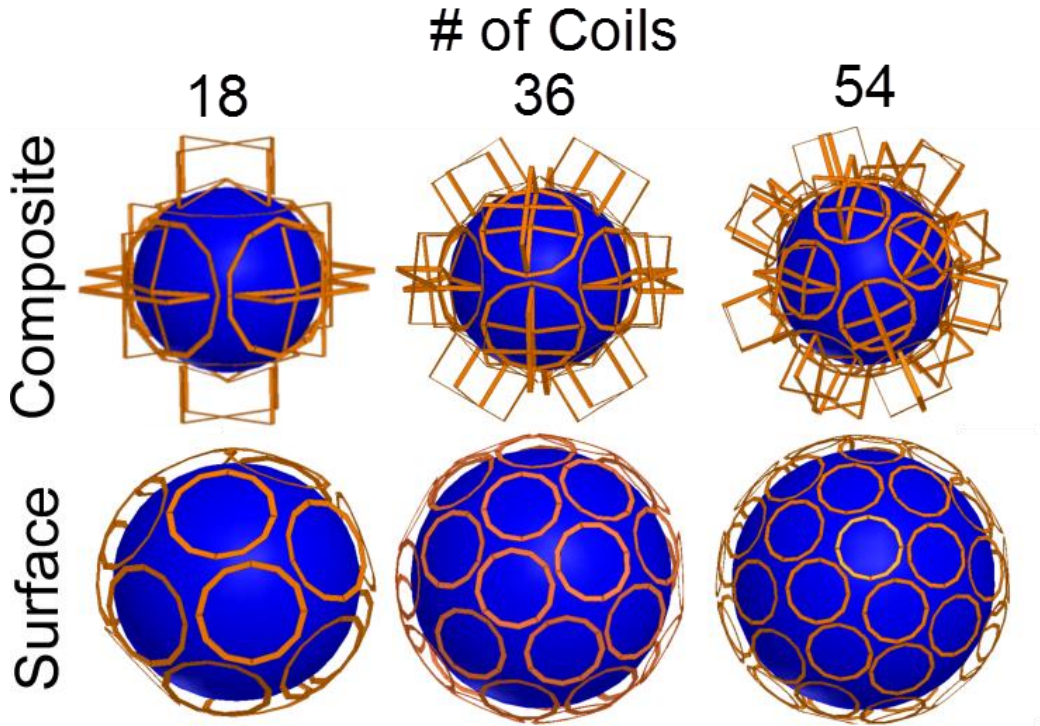


Figure 4.3: composite and surface arrays. Conductors are placed 1cm from the surface of the sphere.

The use of curved, circular or cylindrical components greatly increased the meshing and simulation time so simple strips/polygons were used. The coil material is composed of copper with a conductivity of  $5.8 \times 10^7 \text{ S/m}$  and the capacitor values that are distributed around the coils are found with preliminary simulations to remove a large part of the inductance and decrease the radiation and dielectric losses of the coils.

A single surface and upright element are shown in Figure 4.4, with important coil dimensions labeled. The coil conductors are placed  $10\pm1$ mm away from the surface of the sphere. The diameter of surface coils are 82mm 57mm and 45mm for 18-, 36- and 54- element surface coil arrays with coil copper strip widths of 5mm, 4mm and 3mm. The diameter of surface coils in composite arrays are 140mm 105mm and 82mm for 18-,36- and 54- element arrays with copper strip widths of 5mm for all. The heights of upright coils in these arrays are 56mm, 51mm and 51mm respectively. The position of surface coils in the 54 coil composite coil array is the same as those for the 18 coil surface coil array so the results of the two can be compared as the addition of composite coils to that particular array. The length of upright coils is that of the surface coil in the array minus double the copper strip width and an additional 4mm. All coils have three series tuning capacitors ( $C_t$ ) except the 140mm diameter surface coils, which have five series tuning capacitors.

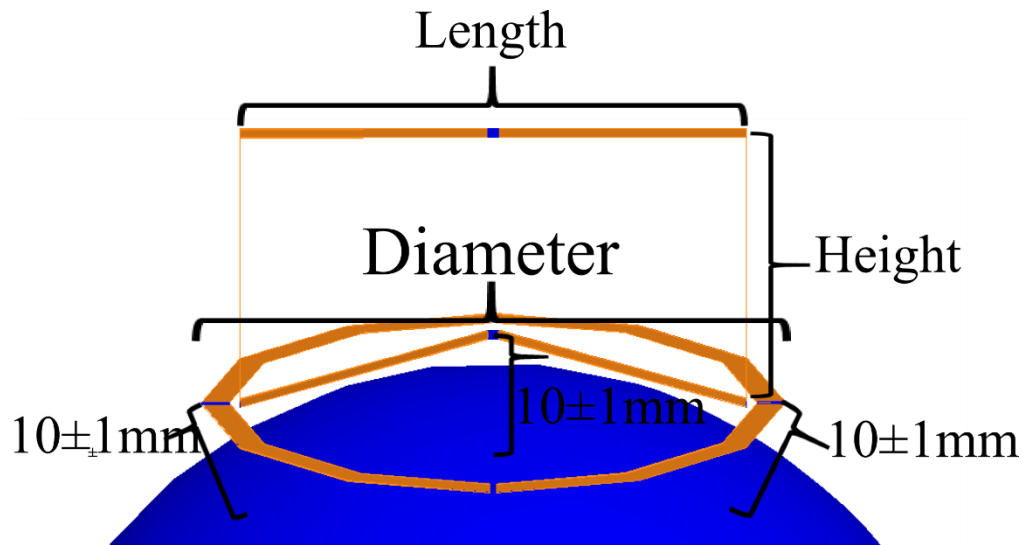


Figure 4.4: Diagram of an upright and surface coil element used in composite coil arrays with labels of coil dimensions and showing locations where the conductor is 10mm away from the sphere surface.

Table 4-1 shows the capacitor values and impedances of the coils. The impedance of both upright coils are shown; one upright coil in each composite coil is moved 2mm farther from the sphere to avoid intersection that results in a slightly higher self-resistance (<15% increase) than the closer upright coil.

The uiSNR and g-factors with the complete coil approximation are compared to the simulated values for arrays in the composite and surface coil

arrays. For the SNR of coil arrays without matching network or preamplifier noise they are modeled as connected to preamplifiers by lossless quarter wave baluns and with a very low preamplifier input impedance of  $0.1\Omega$ , although the input impedance does not change the calculated SNR or g-factors in this case.

Table 4-1: The value of tuning capacitors for each coil in the arrays and the impedance of the coils is listed which is averaged separately over the upright and surface type coils.

	128MHz		300MHz	
	Surface	Composite (surface)/(upright)	Surface	Composite (surface)/(upright)
18 coil- Ct (pF)	30	24/27	4	5.1/4.6
Zcoil ( $\Omega$ )	4.2+7.8j	(24-34j)/(1.1-2.4j) (1.26-2.5j)	34-53j	(95-37j)/(7.3-1.3j) (8.4-0.2j)
36 coil- Ct (pF)	27	22/28	6.7	5.1/4
Zcoil ( $\Omega$ )	1.4-52j	(9.7+15j)/(0.70+7.4j) (0.77+7.6j)	9.0-27j	(60+37j)/(4.5+30j) (5.1+31j)
54 coil- Ct (pF)	45	30/36	7.5	4/4.2
Zcoil ( $\Omega$ )	0.82-13j	(4.1+5.3j)/(0.48+10j) (0.52+10j)	4.5-35j	(22-55j)/(2.4-79j) (2.8-78j)

### 4.3.3. Coupling Comparison

This section introduces methods to measure the overall level of coupling and noise correlation between coils in a large array. The total number of unique coil to coil interactions in the array is

$$N_I = \frac{N_c^2 - N_c}{2}, \quad (4.10)$$

where  $N_I$  is the number of interactions and  $N_c$  is the number of coils in the array.

When the covariance matrix is calculated as if the arrays were matched to  $0.1\Omega$  input-impedance preamplifiers (transformed to a high-impedance at the coil ports) the noise correlation calculated from equation (1.24) is essentially equivalent to the resistive coupling coefficient since in equation (1.23)  $\tilde{\mathbf{Z}}^{-1}$  is close to diagonal.

For the most realistic representation the noise correlation is still calculated from  $\widehat{\Psi}_n$ , which includes the small amount of coupling present when  $Z_{pre}=0.1\Omega$ .

A measure of the coupling between coils is

$$k_c = \frac{|Z_{ij}|}{\sqrt{real(Z_{ii})real(Z_{jj})}} \Big|_{i \neq j}, \quad (4.11)$$

where  $k_c$  is a coupling coefficient similar to the magnetic and resistive coupling coefficients, but measures the overall level of coupling that leads to crosstalk when coils are tuned to resonance (reactive part of  $Z_{ii}$  is removed). Unlike the resistive and magnetic coupling coefficients this overall coupling coefficient can be significantly greater than one because the mutual inductance can be, and often is, greater than the self-resistance.

We define ratios of interactions that fall within various coupling ranges (noise correlation or coupling from equation (4.11)) to the total number of interactions in equation (4.10) as a measure of the coupling levels present in the arrays. Histograms of the interaction ratios are given for both noise correlations and coupling levels in the coil arrays to show the fundamental differences between composite and surface arrays as the element size increases. Each coil has  $N_c - 1$  interactions and the ratio of total interactions falling into specific ranges of coupling or noise correlation multiplied by (4.10) represents the average number of interactions for a coil in the array in that range.

A larger proportion of interactions that have low coupling measured using equation (4.11) is preferred to facilitate construction and optimize SNR. In addition, for a larger ratio of interactions that have low coupling a lower level of preamplifier decoupling as evaluated using equation (1.30) is required to prevent detrimental effects of coupling.

#### 4.3.4. Realistic Noise Comparison

To compare the effect of realistic noise from matching networks and preamplifiers the SNR is compared between using the optimum combination with  $\widehat{\Psi}_n$ , and then when using  $\Psi_{diag}$  for the noise with matching network and preamplifier noise from equation (4.3) and (4.6) at 128MHz. The quarter wave

balun shown in (Figure 1.2a) is used and the components chosen to transform the self-resistance of each coil to  $50\Omega$ .

Two values of equivalent series resistance (ESR) for the inductors and capacitors in the matching networks are used to compare the noise factor with a range of matching network noise at 128MHz; the low and large ESR of capacitors (ESR\_C) are  $0.05\Omega$  and  $0.15\Omega$ , while the low and high ESR of inductors (ESR\_L) are  $0.12\Omega$  and  $0.36\Omega$ . The final comparisons of array performance including matching network noise uses the higher ESR values and at 300MHz the higher ESR values are scaled by the square root of the frequency.

The minimum noise figure of preamplifiers added to coils individually in equation (4.6) is 0.5dB. When comparing to the N-port method of calculating noise using  $\Psi_\eta$  from equation (4.3) the preamplifier noise parameters in equation (1.28) used to calculate the noise wave parameters in equation (4.4) are  $Z_{opt} = 45\Omega$  and  $R_n = 2\Omega$ . The preamplifier S-parameters (magnitude∠angle) used are those of the ATF-54143 LNA at 100MHz when  $V_{ds}=3V$  and  $I_{ds}=60mA$ ; namely  $S_{11}=0.99\angle-18.9^\circ$ ,  $S_{21}=27.66\angle167.7^\circ$ ,  $S_{12}=0.01\angle80^\circ$ ,  $S_{22}=0.54\angle-14^\circ$ . An additional L matching circuit is applied before the preamplifier that transforms the input impedance of the preamplifier (calculated from effective series capacitance and resistance resulting in the given  $S_{11}$  at 100MHz at 128MHz and 300MHz) to the effective low input preamplifier impedance  $Z_{pre}$ . The value of  $Z_{opt}$  at the preamplifier terminals in the analysis is then the transformed value of  $45\Omega$  by the L-matching network.

For the final comparison between arrays with noise a preamplifier input impedance of  $6\Omega$  is used, and it will be shown that when using  $\Psi_{diag}$  the final SNR is not significantly dependent on  $Z_{pre}$ , but when using  $\Psi_\eta$  the SNR depends greatly on  $Z_{pre}$ . The S-parameters used in equation (4.2) are those of the quarter-wave baluns and L-matching networks together. ESR is not included in the lumped components of the L-network, since only their effect in changing SNR due to the preamplifier input impedance is being investigated.

The noise factor contributions of the preamplifier and matching networks is calculated as

$$F_{match}^{add} = \left( \frac{SNR_{int}}{SNR_{match}} \right)^2 \quad (4.12)$$

$$F_{pre}^{add} = \left( \frac{SNR_{int}}{SNR_{pre}} \right)^2$$

where  $F_{match}^{add}$  and  $F_{pre}^{add}$  are the overall noise factors of the matching networks and preamplifiers plus matching networks respectively.  $SNR_{int}$ ,  $SNR_{match}$ , and  $SNR_{pre}$  are the combined SNRs calculated using equation (4.9) using  $\widehat{\Psi}_n$ ,  $\Psi_m$ , and  $\Psi_{diag}$  respectively.

## 4.4. Results

The simulated and measured SNR of three-coil composite and surface coil arrays shown in Figure 4.2 are compared to validate the simulation method and to compare the SNR of an array with only surface components to a composite array with an equal number of elements over the same field-of-view (FOV). The coupling and noise correlation of arrays shown in Figure 4.3 are compared and because this affects the SNR of the optimally combined image the SNR when loss in capacitors and inductors are included is compared as well. Finally, the uiSNR and g-factors with the theoretically complete coil are compared to the simulated values in the composite and surface coil arrays with and without matching network and preamplifier noise.

### 4.4.1. Three Coil Array Comparison

Optimum SNR maps of the three-coil composite coil and surface coil array (Figure 4.2) in sagittal slices through the center are shown in Figure 4.5. The maps are normalized to the average SNR of the single 12cm diameter surface coil in three sagittal slices  $\pm 6\text{cm}$  in the direction of  $B_0$ , one central and two offset  $\pm 3.5\text{cm}$  (1.33 for simulated and 29.6 for measured). The images show the relatively higher SNR of the surface coil array and the difference in homogeneity between the two arrays. Since the slice shown is through the center of the array the composite coil array shows higher SNR at the surface due to the one upright coil parallel to  $B_0$ , which

has very high sensitivity there; the depth with this large SNR is approximately 2mm on the periphery.

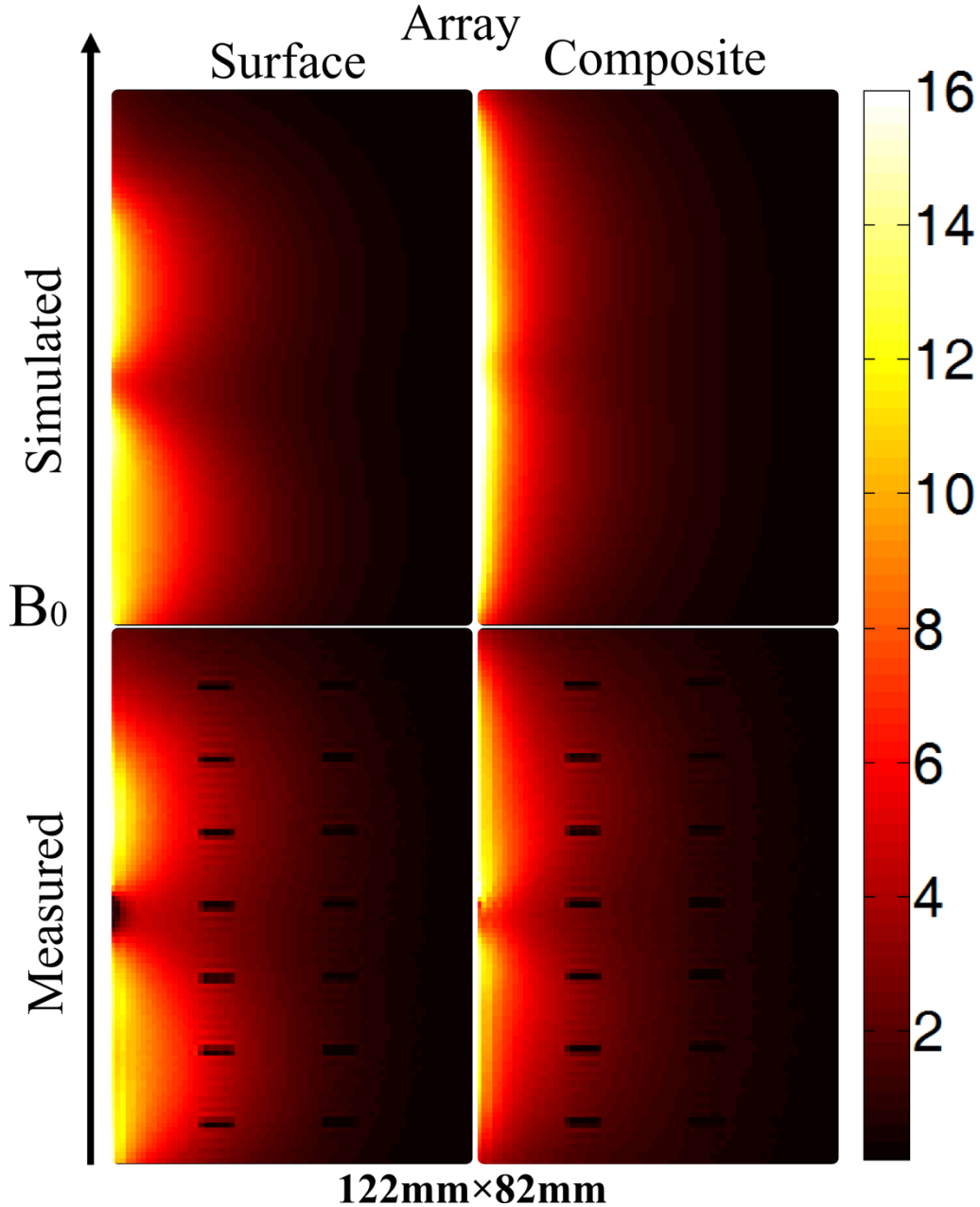


Figure 4.5: Optimally combined SNR maps of the three-coil surface coil array and composite array in a sagittal slice through the center. The dimensions of the images are indicated on the bottom which is the same for all images.

The average SNR in the direction of  $B_0$ , relative to the single 12cm diameter coil in the central sagittal slice of Figure 4.5 and slices offset by  $\pm 3.5\text{cm}$ , is shown in Figure 4.6. Also, the SNR of the single 12cm diameter coil normalized to its

average is shown. The improvement of the arrays to the single surface coils is slightly higher in measurement than in simulations, but both follow the same trend with depth. The measured single coil has decreases in the SNR where grid planes are present, which may change the overall comparison of simulated and measured results. The surface coil array outperforms the composite array up to a depth of 60mm, with a maximum difference of about 50% for a depth of 5-25mm. The composite coil array does provide more homogeneous sensitivity and the improvement stays significantly large with depth. The close relation between simulated and measured improvement with composite versus surface array over the single 12cm-diameter coil validate the simulation method.

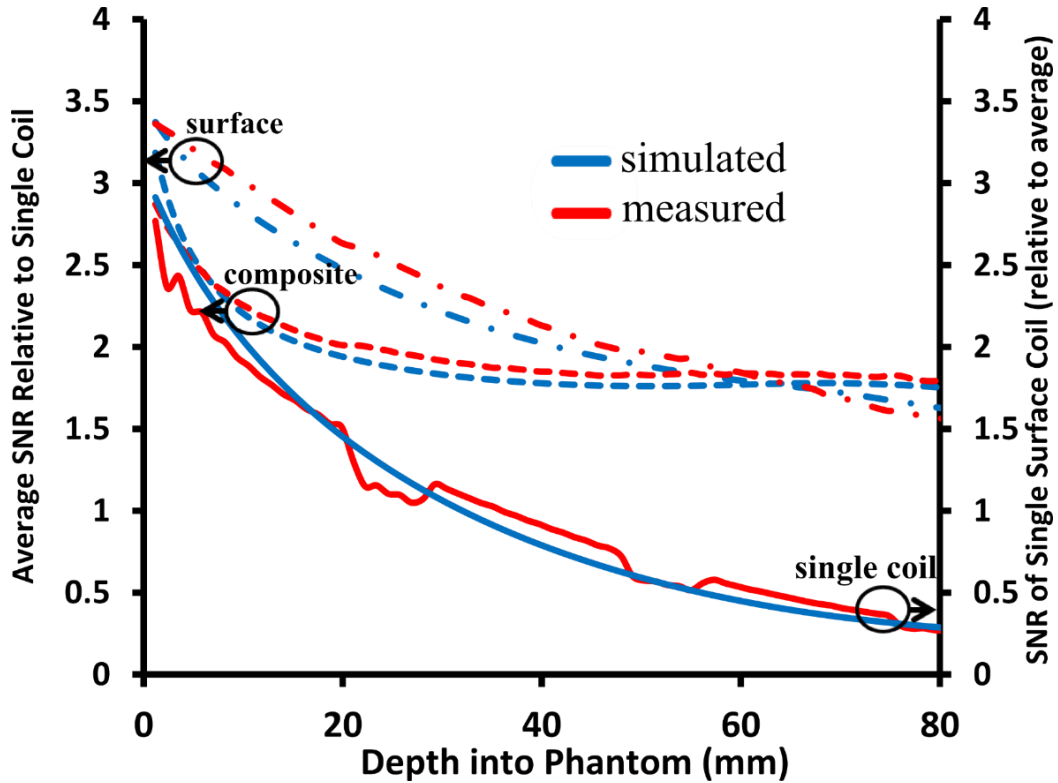


Figure 4.6: Average SNR in sagittal slices relative to the single 12cm diameter surface coil as a function of depth for the (dashed) composite array and (dash-dot) surface coil array. The simulated (blue) and measured (red) single surface coil SNR normalized to their average in the slices is also shown with solid lines. The composite array begins to out-perform the surface coil array at depths of 60mm

#### 4.4.2. Coupling of Arrays

The convention used for displaying the coil coupling/noise correlation between coils is shown at the top in the legend of Figure 4.7. The symbols used to indicate the types of adjacent coil interaction include surface coils that are next to each other, upright coils that are next to each other and either face each other or are coincident and upright coils that are facing adjacent surface coils.

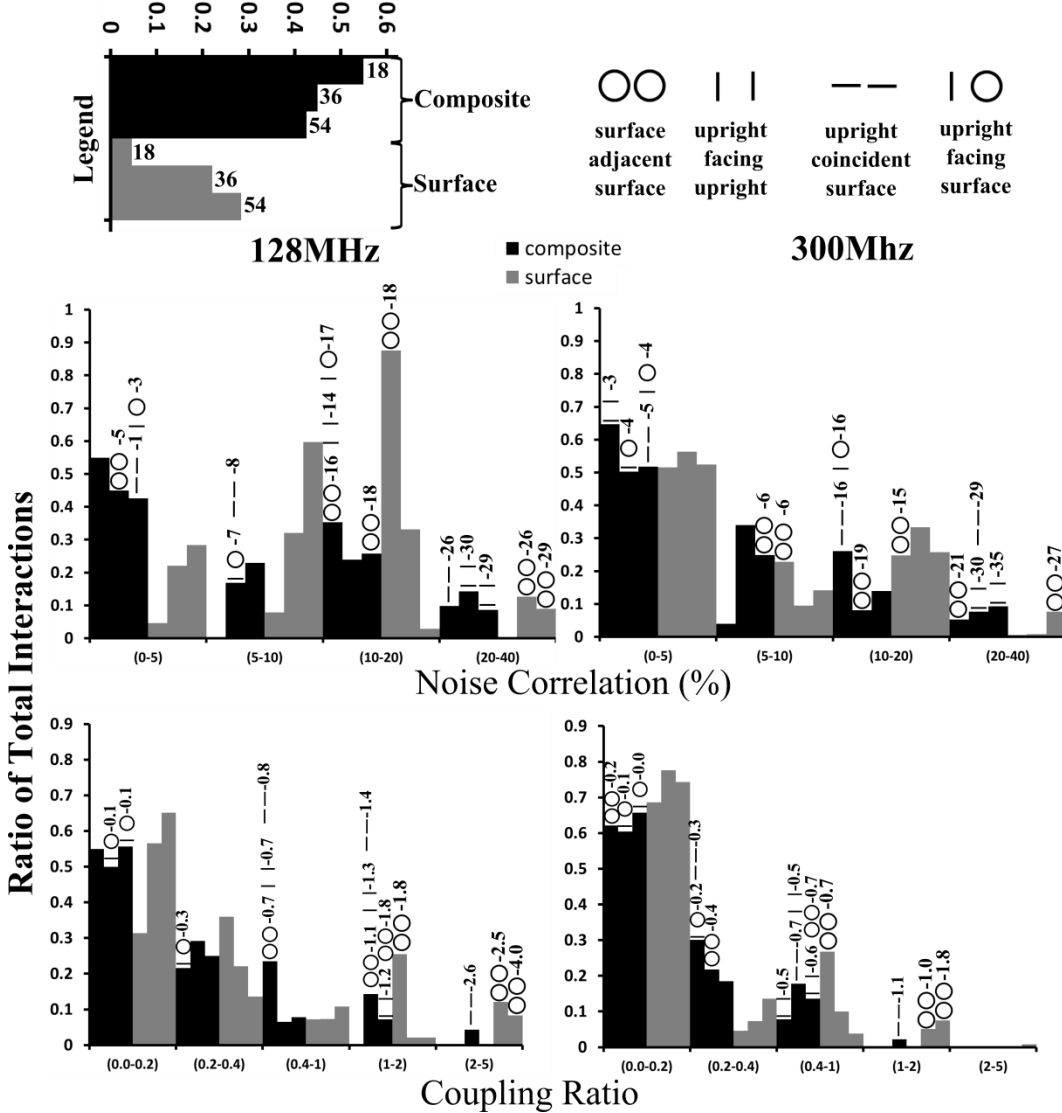


Figure 4.7: Histogram of simulated arrays' (top) noise correlations and (bottom) coupling ratios between elements in composite and surface coil arrays. The average values for the adjacent coil-coil interactions given next to their symbols above the corresponding bars; for the non-adjacent coil interactions that aren't shown the majority are in the lowest range shown.

The histogram of coil correlation/coupling interactions (equation (4.10)) is shown in Figure 4.7. The legend showing the bar graph convention and the symbol convention for coil interactions are given at the top. Symbols are given for adjacent coil interactions since they are the highest and have the greatest effect on final covariance and signal. The strongest interactions, largest noise correlations and coupling ratios, are between adjacent surface coils. The majority of composite array noise correlations are low (<5%), which accounts for coils that are within a composite coil triplet and in contrast to results in Chapter 3 the noise correlation between surface coils and upright coils facing them is very low for coils on a sphere compared to the large values for coils on a planar surface. The highest levels of noise correlation (>20%) and coupling ratios defined in equation (4.10) (>1) are between surface coils, especially as their array element count increases. For upright coils, adjacent coils that face each other and ones that are coincident have high noise correlations, but they are typically less than those between the adjacent surface coils. The coupling ratio levels in all arrays decreases as the frequency increases, largely because the self-resistance of coils increases (proportional to the square of frequency) faster than the mutual reactance between coil (proportional to frequency).

#### 4.4.3. SNR with Matching Networks and Preamplifier Noise

Figure 4.8 shows the added noise by matching networks and preamplifiers for the different arrays at 128MHz. As indicated in the legend at the top of Figure 4.8, the top of the bar shows the noise factor contribution of the preamplifiers ( $F_{pre}^{add} - F_{match}^{add}$ ) while the bottom indicates the contribution of matching networks ( $F_{match}^{add}$ ). The bar graph convention for different arrays is also shown. To the best of my knowledge, the variation of optimum SNR degradation with position due to additional noise sources has not been shown for MRI coil arrays, which proves to be an important criterion for judging final array performance.

The detriment from the matching network and preamplifier noise to the optimally combined SNR of composite arrays versus surface arrays is much less at the center, despite the lower body loading of the upright coils at 128MHz (Table

4-1). The orthogonal sensitivities, as well as covariance between upright and adjacent elements both contribute to the compensatory effect that allow the optimally combined SNR noise factor to be significantly less than the individual coil matching network and preamplifier (Table 4-2) noise factors.

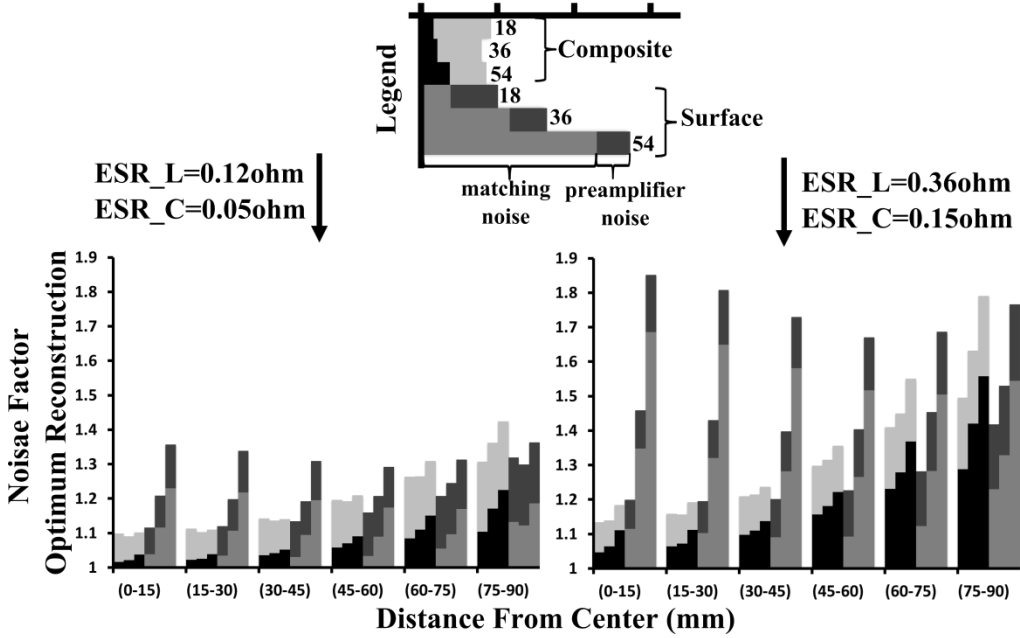


Figure 4.8: The noise factor contribution to optimum SNR at 128MHz using different lumped element ESRs with an added 0.5dB to the diagonal of the covariance matrix to represent preamplifier noise figure. With the higher ESR values the matching network is the larger noise contributor.

Going from the lower to higher ESR values in the matching networks also leads to a much larger increase in noise factor for the surface arrays with 35 and 54 elements compared to the composite arrays. Near the surface, where the coil sensitivities do not overlap, the SNR factors are larger than the individual matching and preamplifier noise factors and are about equal for composite and surface arrays.

#### 4.4.4. Comparison of SNR Varying Preamplifier Input Impedance

Figure 4.9 shows the average SNR 0-15mm and 60-75mm away from the center as the preamplifier input impedance is varied using the covariance matrix originating from the N-port preamplifier noise model ( $\Psi_\eta$ ), or the individually added preamplifier noise model ( $\Psi_{diag}$ ). The 18 element arrays are excluded for clarity, but the results are similar as well.

Changing the preamplifier input impedance from  $9\Omega$  to  $0.1\Omega$ , a significant increase in the level of preamplifier decoupling, has little effect on the SNR when using  $\Psi_{diag}$  (solid lines), but result in a large reduction when using  $\Psi_\eta$  (dashed lines). In fact, as the preamplifier input impedance decreases the noise from preamplifiers is much more easily transferred between channels in the N-port model. The transfer and decrease in SNR affects the arrays with the highest coupling and larger element count; composite coils are less affected by the noise added in the N-port model.

The N-port noise wave model as well as models assuming correlated noise sources at the input of the preamplifiers (both models being equivalent) assume physical currents are produced at the input. The discrepancy arises in Figure 4.9 because of the transfer of this noise back into the array in the N-port model that cannot. The individually added preamplifier noise model assumes the noise is added at the preamplifier output and does not couple back into the array.

The preamplifier input impedance has no effect on the optimum noise combination added by the matching networks using  $\Psi_m$ ; similar to there being no impact on the final SNR due to mutual inductance demonstrated theoretically in reference [17]. Although the individual noise coil noise covariance (diagonal of covariance matrix) can and does change.

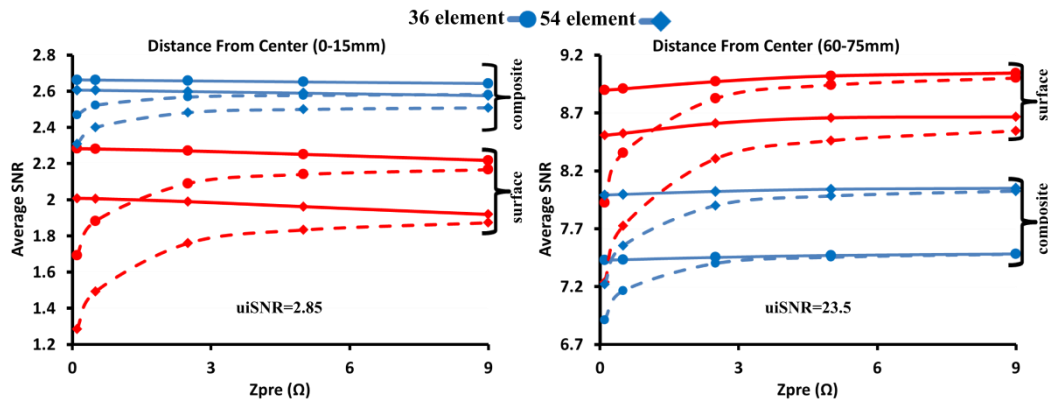


Figure 4.9: The average SNR at 128MHz of 36 (circle markers) and 54 (diamond markers) element arrays shown in Figure 4.4 using an N-port (dashed line) or individually added (solid line) preamplifier noise model at a distance of 0-15mm (left) or 60-75mm (right) from the center. Composite coil arrays (blue) show less sensitivity to the preamplifier input impedance than the surface coil arrays (red)

In the discussion of previous results using the N-port noise model it has been stated that “For optimal noise performance, the matching network must decouple the array and present isolated, individually noise-matched ports to the amplifier inputs” [11]. Therefore, in the case where current produced at the preamplifier inputs is freely transferred between coils, as seems to be the case here as preamplifier input impedance become extremely low ( $0.1\Omega$ ), either a decoupling matching network [23] or more complicated matching to the “active antenna impedance” seen at the preamplifier ports [9, 12] is required. Analysis of this matching and performing it on coil arrays is an undesirable proposition, especially if acceptable performance is more easily reached by using preamplifiers with higher effective input impedance.

As  $Z_{pre}$  increases the N-port model SNR converges with the individually added preamplifier noise model. This confirms that with some assumptions the individually added model can be used as in reference [16], but there may be some loss in accuracy compared to a full N-port model. For the rest of the SNR/parallel imaging comparisons presented the individually added noise model is used with a  $Z_{pre}$  of  $6\Omega$ , since it relies less on assumed preamplifier noise properties and S parameters, while losing little accuracy compared to the N-port model with  $Z_{pre}=6\Omega$ . Also, experimental validation is still required to confirm the accuracy of the N-port model in representing preamplifier noise in coil arrays. Validation of the N-port model’s veracity would have important implications for preamplifier use and design in MRI coils.

#### 4.4.5. Individual Coil Noise Factors

The difference in N-port channel noise figures is calculated from the increase in the covariance matrix diagonals going from  $\widehat{\Psi_n}$  to  $\Psi_m$  for matching networks and from  $\Psi_m$  to  $\Psi_\eta$  for preamplifiers. The individual noise figure is calculated using equation (1.27) for matching networks and a standard value of 0.5dB for preamplifiers. The individual and N-port noise figures are shown in Table 4-2. The surface coil arrays show the largest difference between the two

because of the larger levels of coupling between adjacent elements facilitates the transfer of noise between coils. Because of the lower resistance of upright coils they suffer greater noise factors, but as Figure 4.8 show, this is partially compensated for in the reconstruction.

Even though preamplifier input impedance and coupling doesn't affect the optimal reconstructed SNR with matching network noise it does have an obvious effect on the diagonal noise covariance values [24]. The noise figures using the N-port model of preamplifier noise greatly increase going from an input impedance of  $6\Omega$  to  $0.1\Omega$ . The matching network noise figures usually increases as well, but the increase is much less dramatic and doesn't occur in every array.

The additional noise from the ESR of tuning capacitors or solder joints [2] are not included in this analysis, but their effect is similar to the effect of larger ESR values in the matching network or a greater preamplifier noise figure. This chapter shows the importance of including the multiport model of coils noise for evaluation of noise added by these components and just looking at the noise factor with individual coils [2] is not sufficient to understand the impact on final SNR when coupling between elements is large.

Table 4-2: Noise figure (dB) added to individual channel noise variances for matching networks (ESR\_L=0.36,ESR\_C=0.15) and preamplifiers. The noise figures are either calculated using the diagonal of the N-port covariance matrices or from noise figures of the individual matching networks and preamplifiers when the coils self-resistance is transformed to  $50\ \Omega$ .

Matching/Preamplifier Noise Figure For Individual Coils (dB)				
		N-port		
		Individual	$Z_{pre}=0.1\Omega$	$Z_{pre}=6\Omega$
<b>18 coil</b>	surface	0.28	0.52/1.60	0.46/0.57
	composite	0.07	0.13/0.80	0.14/0.52
	surface-upright	0.88	0.92/0.72	0.95/0.52
<b>36 coil</b>	surface	0.76	1.29/2.56	1.11/0.63
	composite	0.13	0.31/1.32	0.29/0.56
	surface-upright	1.28	1.48/1.44	1.55/0.57
<b>54 coil</b>	surface	1.21	2.16/3.61	1.84/0.72
	composite	0.29	0.54/1.65	0.50/0.58
	surface-upright	1.88	2.33/2.32	2.38/0.65

#### **4.4.6. SNR of Arrays compared to uiSNR**

The SNR of the arrays and uiSNR in a transverse slice through the center at 128MHz and at 300MHz is shown in Figure 4.10. In a coronal slice the uiSNR at the surface along the  $B_0$  direction is found to be 82% of the uiSNR at the surface of the sphere along the axis perpendicular to  $B_0$  consistent with reference [21]. The SNR of the finite coil arrays is not homogeneous, and sensitivity is much greater at the regions next to the coils with many gaps in sensitivity at the surface between coils. Nearer to the center the homogeneity approaches to that of the uiSNR especially for the 54 coil arrays. It is noticeable in both the uiSNR and finite coils' SNR that with equal magnetization SNR is higher at 300MHz than at 128MHz, but the same at the surface; this is due to the transition from near field, with rapidly decaying amplitude, to far field with propagating fields that decay less rapidly from the source [21].

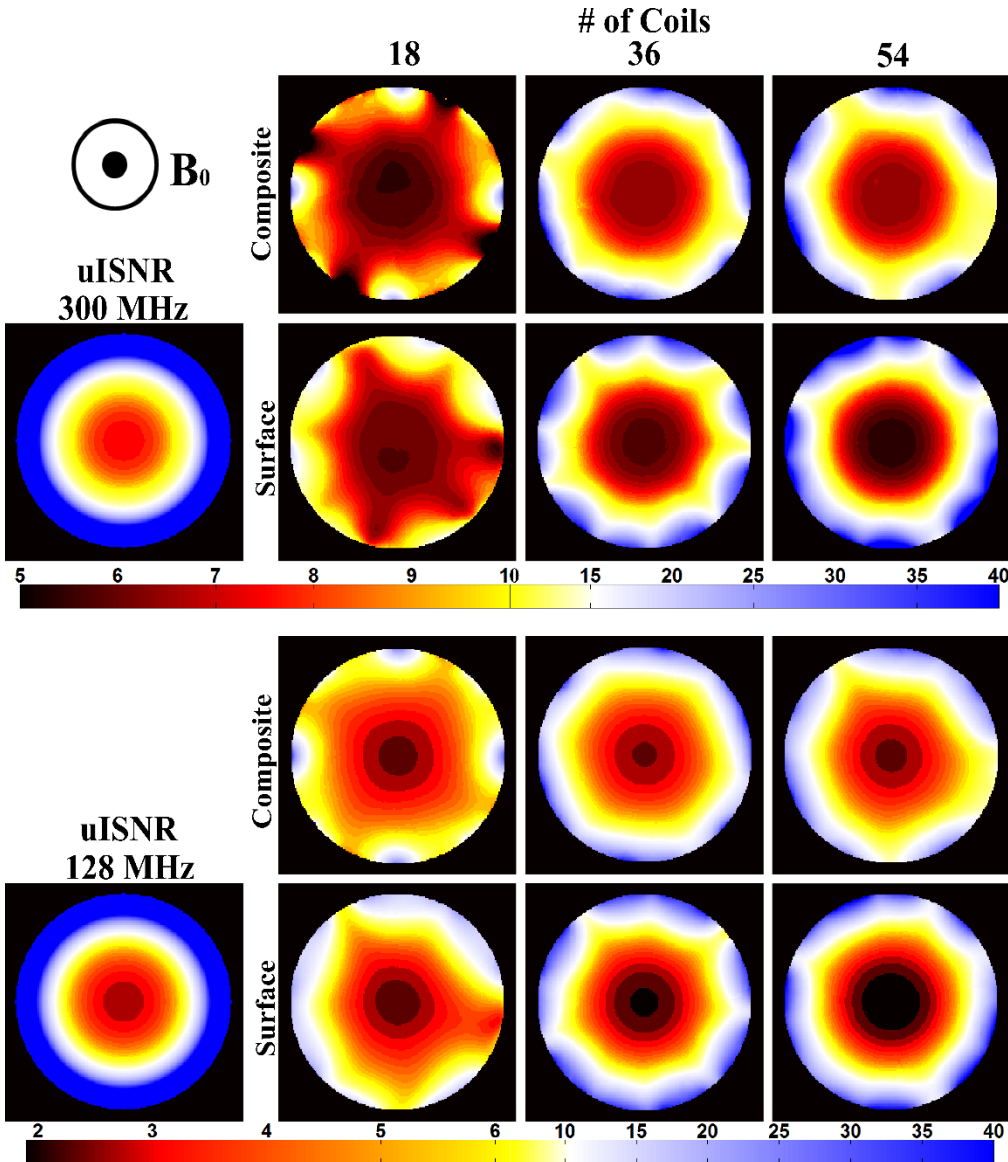


Figure 4.10: SNR of the arrays and uiSNR in a transverse slice through the center at 128MHz and 300Mhz. The uiSNR at the periphery (outer 1.5cm) increases exponentially and is much higher than with the finite coil arrays.

The average combined SNR of the arrays compared to the uiSNR calculated using equation (4.9) with and without preamplifier and matching network noise is shown in Figure 4.11; the SNR of the finite coils are compared to the maximum achieved by any of the arrays in each range. The ratio of the maximum achieved by the finite coils to the uiSNR is then given at the top of the graphs, and the uiSNR is plotted with the maximum of the arrays in each range on the secondary axis. The finite coil array SNR at distances from the center are

averaged over 3 coronal, 3 transverse and 3 sagittal slices (through the center and  $\pm 25\text{mm}$ ), while for the uiSNR the values are averaged at distances from the center using one coronal and one transverse slice; less slices are required for the uiSNR since it is far more homogeneous in the sphere for the same distance from the center.

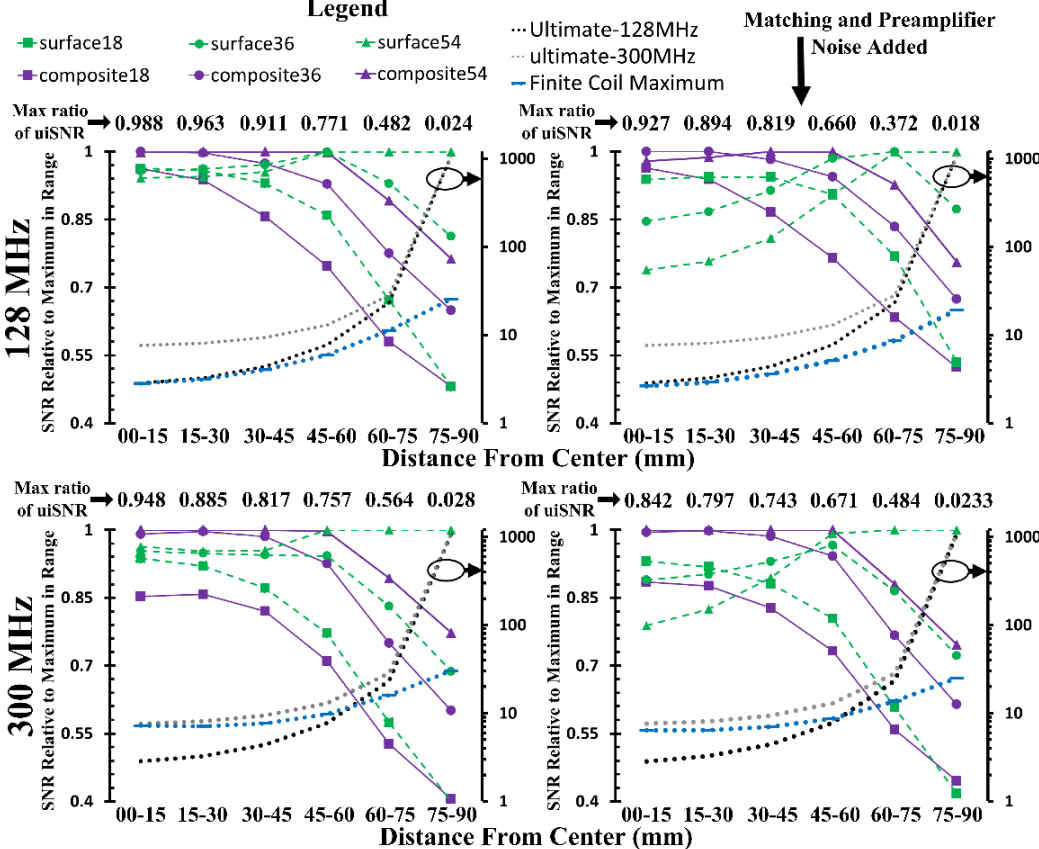


Figure 4.11: Optimally combined SNR for finite coil arrays coils compared to the maximum achieved by all arrays, the ratio of the maximum to uiSNR is shown above each graph. Plots are without preamplifier or matching network noise (left) and ( $Z_{\text{pre}}=6\Omega$ ) with both (right) at 128MHz (ESR\_C=0.15Ω, ESR\_L=0.36 Ω) and 300MHz (ESR\_C=0.23 Ω, ESR\_L=0.55 Ω). The marker and line corresponding to each array size and type is shown in the legend at the top. The right axis is the scale for uiSNR at 128MHz (black dots) and 300MHz (grey dots) and the maximum achieved by finite coil arrays (blue dots, line marker).

In addition to the factor of  $B_0$  in equation (4.9) the uiSNR at 300 MHz would be further improved over that at 128MHz by increased magnetization, which is proportional to the magnetic field strength [22]. Since the uiSNR and finite coil SNR at 300MHz is already higher than that at 128MHz the obtainable SNR improves at a faster than linear rate, consistent with results in references [21, 25].

The average of the uISNR for 75-90 mm at 128MHz and at 300MHz is both 1077, indicating a linear growth with field strength at the surface also found in reference [21].

The composite arrays shown in purple with solid lines have higher SNR at the center of the sphere than the surface coil arrays shown in green with dashed lines, which is significant because there is very little room for improvement near the center as the SNR is already very close to the uiSNR. Up to about 45-60mm from the center of the sphere the SNR of composite arrays remain larger or comparable to the surface coils, but close to the surface the SNR of surface arrays with equal number of elements are much higher. At the surface, both are very far from the uiSNR but in absolute terms they are also much higher than at the center. This is consistent with previous results that have shown electric-dipole like currents are important in approaching the uiSNR near the center of the phantom [4].

With the larger noise factors for surface coil arrays shown in Figure 4.8 the composite arrays perform even better comparatively at the center when including the impact of noise. This is partly because the SNR of the larger surface coils in the composite arrays are degraded less than the smaller coils in the surface arrays and partly because the upright coils have larger noise covariance with adjacent upright coils and complementary sensitivities that are able to compensate near the center. The composite arrays have higher SNR than surface array at the center for 36 and 54 element arrays, but lower at the periphery. Overall, with realistic noise the composite coil array performance suffers less noise degradation than the surface coil arrays in the inner half of the sphere.

At 128MHz the largest surface coil array, with 54 elements, loses the most SNR because of larger individual noise factors (Figure 4.8) and the large coupling ratios between adjacent coils (Figure 4.7) allows matching network noise to couple between coils. Also, the sensitivities of adjacent coils are similar near the center, limiting the amount of compensation the signal weighting can provide. However, the larger SNR of the surface coil arrays allow the surface arrays to still provide higher SNR at the periphery (>60mm from center). It is clear that with realistic noise included the use of composite coils (or similar coil types) provides

significantly higher SNR in the inner 2/3<sup>rd</sup> depth for arrays of the size studied and for this region their use is a better strategy than progressively decreasing the size of surface coils. However, if the imaging region of interest is at the periphery arrays consisting of surface coils are still the logical choice.

#### **4.4.7. Parallel Imaging Comparison**

Parallel imaging performance at 128MHz and 300MHz is illustrated in Figure 4.12, which contains average g-factors in the sphere for a central transverse slice both with and without preamplifier and matching network noise. The g-factors of the finite coil arrays are compared to the values calculated with the basis function sensitivities (as stated in section 4.2.2, a total of  $2(80+1)^2$  basis functions, which has converged to limit of infinity for SNR and g-factor comparisons) used to calculate the uiSNR. The g-factor maps in an axial slice are also shown, including noise from matching networks and preamplifiers in Figure 4.12. There is still significant room for improvement as the difference between finite coil and uiSNR g-factor performance indicates. After an acceleration of 4 the g-factors show an exponential growth and at an acceleration of 5 there is a transition to mean g-factors greater than 1.2 (0.79dB) in best coil array performance (54 element surface coil array) to worst coil array performance (18 element surface coil array), a common limit above which parallel imaging is not advantageous [26]. These trends and numbers are consistent with previous results for arrays of surface coils [21, 22, 25].

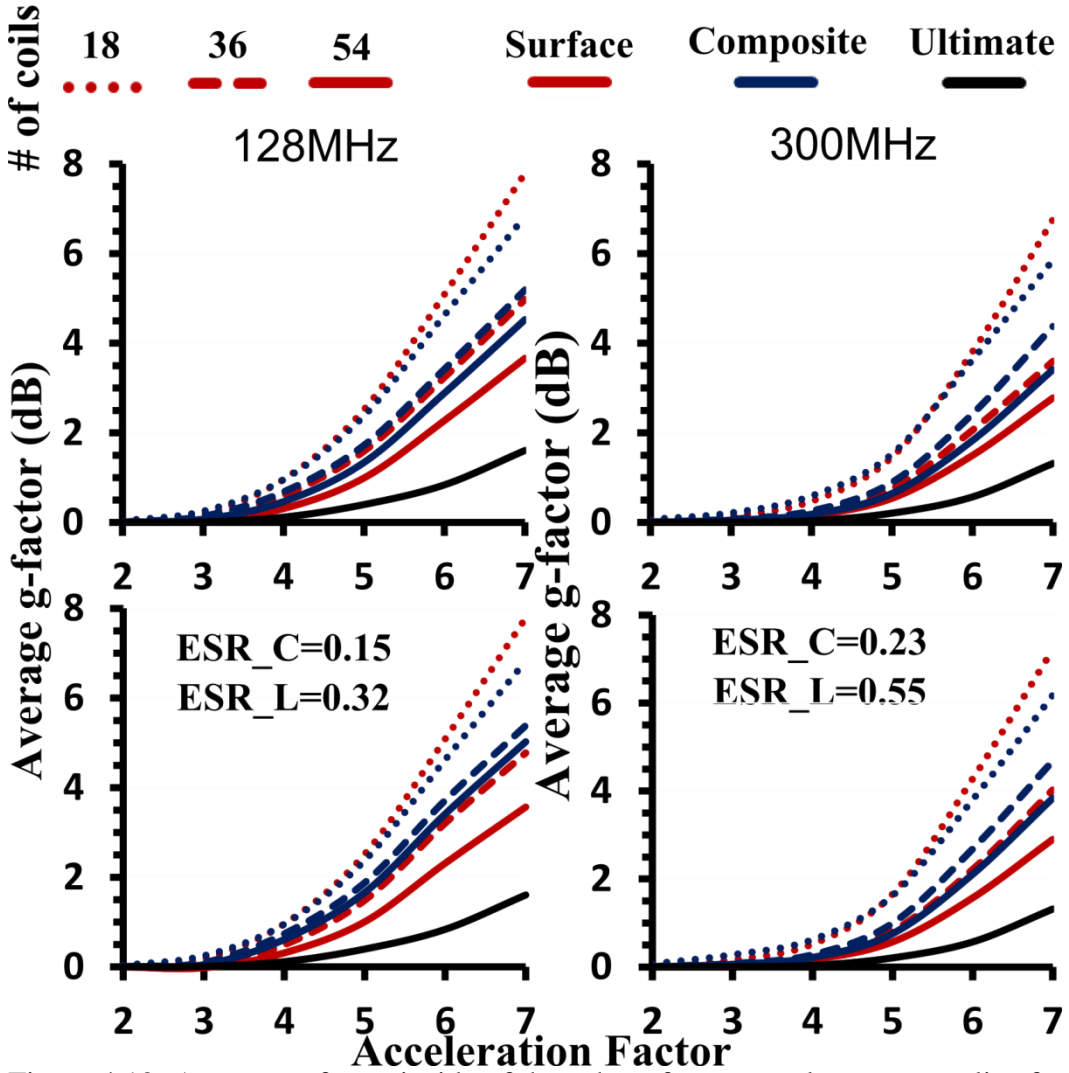


Figure 4.12: Average g-factor inside of the sphere for a central transverse slice for 128MHz and 300MHz. Blue lines are composite coil arrays, red lines are surface coil arrays and the solid black line is the uiSNR g-factors. The array size is indicated by the line type: 18 coils (dotted), 36 coils (dashed) and 54 coils (solid lines). The bottom row is the g-factors with preamplifier and matching network noise included.

The g-factor maps with realistic noise at an acceleration of 5 is shown for 128MHz in Figure 4.13 and for 300MHz in Figure 4.13 since the major transition to mean g-factors greater than 1.2(0.9dB) occurs at this acceleration. Note that the scale used for the uiSNR g-factors is different than for the finite coils arrays since otherwise it there would be very little contrast in the image. The difference in g-factors at 128MHz and 300MHz is dramatic for both the finite coil arrays and the uiSNR; basically, the obtainable acceleration factor is increased by one going from 128MHz to 300MHz (for 36 and 54 coil arrays). The performance of 36 and 54

element composite coil arrays are very similar and at 300 MHz the performance of all 36 and 54 element surface coil arrays are similar except for localized regions.

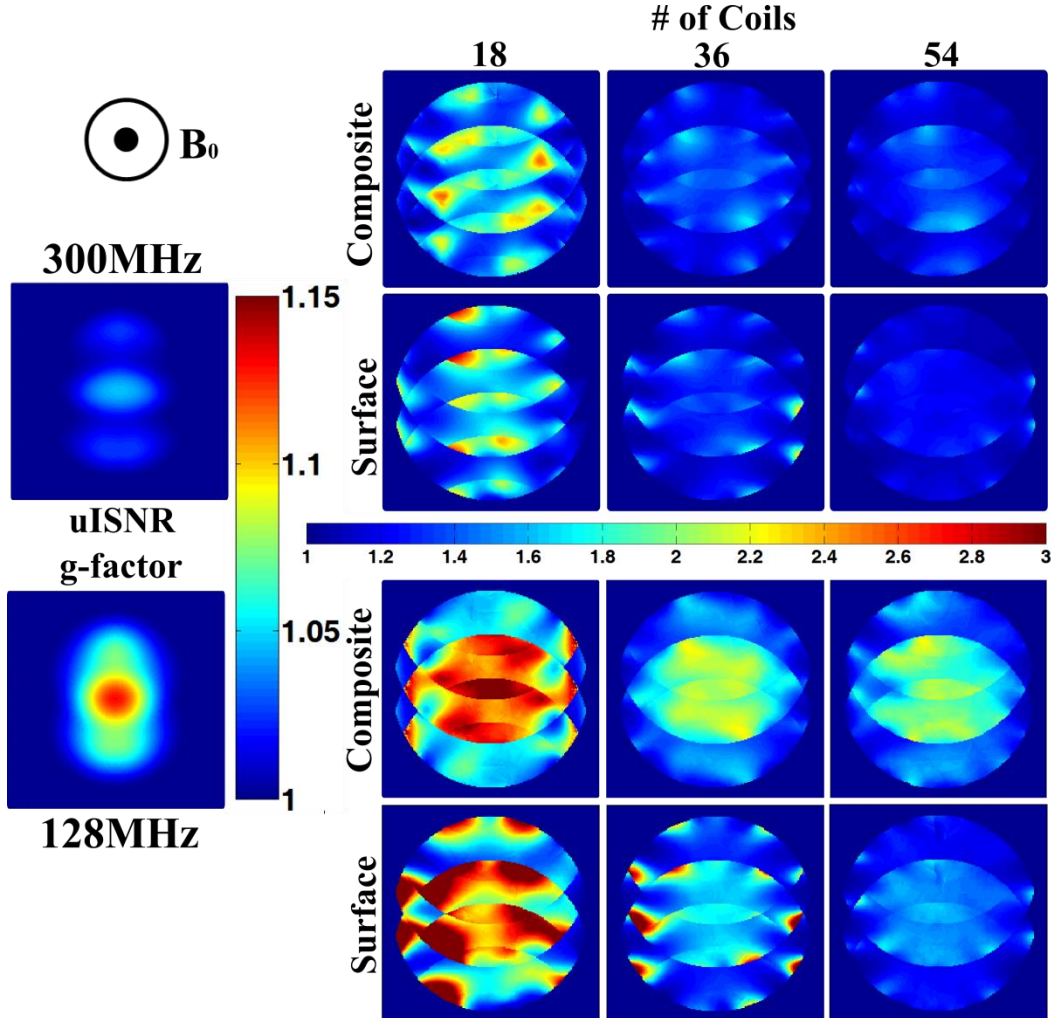


Figure 4.13: g-factor maps for a reduction factor of 5 in a central transverse slice at 128MHz with realistic noise included. It is readily seen that only the 54 element surface coil array would provide acceptable g-factors at 128MHz (using the 1.2 – average g-factor limit), but as frequency increases the 36 element and 54 element composite and surface coil array have acceptable performance.

The diversity of sensitivity phase information and coil sensitivity magnitude variation that are provided by upright coils are beneficial in parallel imaging with lower density coil arrays [25], and leads to smoother g-factor maps with lower peaks. In high-density arrays, however, these variations are provided more effectively by the smaller size and a larger number of surface coils. The surface coil arrays likely result in lower g-factors (for 36 and 54 coil arrays) because their

smaller physical size means more localized sensitivity fields for coils. Larger coil arrays consistently show lower g-actors, indicating that the lower penetration depth of smaller coils indeed isn't an issue for parallel imaging since the ability to distinguish pixels at different depths is actually improved [25]. Beyond an acceleration of 6, even at 300MHz, the uiSNR does not result in mean g-factors less than 1.2 (0.79dB) showing that putting much effort into increasing the g-factor performance with larger arrays may not be worthwhile.

## 4.5 Summary

In this chapter the comparison of finite coil arrays to the uiSNR with and without realistic noise from matching networks is done to show the potential benefits and shortcomings of using composite coil arrays rather than just surface coils as the size of arrays increases. Furthermore, the limiting factors in reaching the uiSNR and optimum obtainable parallel imaging performances are highlighted: losses due to coil losses, additional matching circuitry and preamplifier noise figure, but additional matching and preamplifier noise reduce this.

Compared to Chapter 3 results in this chapter show there are differences in coupling between composite coils on flat versus curved surfaces (ex. low noise correlations in this chapter versus small in previous chapter for upright coils facing surface coil). In addition to this difference, there will likely be differences in the parallel imaging performance and SNR on flat surfaces compared to curved that need to be researched as well.

In this study, partially because of coil noise and partially because of the noise after the coil ports, there is a sufficiently high relative decrease in SNR for the 54 element surface arrays shown in Figure 4.11 in the inner half of the sphere at both 128MHz and 300MHz, so that the 36 element arrays perform better in this region. This indicates that if the inner half of the sphere is the desired imaging region the additional noise due to matching and preamps limits the practical number of channels to around 36.

The SNR of the composite coil array is shown to be higher at depths greater than 4.5-9cm, and still increases with increasing element counts up to at least 54

coils. However, at this depth arrays of surface coils with greater than 16 elements already have iSNRs greater than 80% of the uiSNR [22] and for the inner third of the sphere the SNR of finite coil arrays is already extremely close to that of uiSNR (>90% at 128MHz and >80% at 300MHz in Figure 4.11), so the room for improvement is small. However, the composite coils maintain their performance with respect to the noise added by coupling, matching, and preamps as density increases, so the SNR provided by surface coil arrays with realistic noise conditions is reduced further. Although the g-factor performance of surface arrays with greater than 18 elements is better than the composite arrays Figure 4.13 indicates that the g-factor is more uniform for the composite coils, which is desirable since large regional decreases in SNR are more detrimental for imaging than uniform degradation.

Since there are limited applications that look at the surface of anatomical regions and most of the interesting anatomical structures are located in the center of the body or head, large composite coil arrays should prove to be more desirable for the majority of imaging applications.

## Bibliography

- [1] N. De Zanche, F. Wiesinger and K. P. Pruessmann, "The dependence of SNR on the number of independent coils," in *Proceedings of the Second International Workshop on Parallel MRI*, Zurich, 2004, pp. 112.
- [2] A. Kumar, W. A. Edelstein and P. A. Bottomley, "Noise figure limits for circular loop MR coils," *Magn. Reson. Med.*, vol. 61, pp. 1201-1209, 2009.
- [3] G. C. Wiggins, J. R. Polimeni, A. Potthast, M. Schmitt, V. Alagappan and L. L. Wald, "96-Channel receive-only head coil for 3 Tesla: Design optimization and evaluation," *Magn. Reson. Med.*, vol. 62, pp. 754-762, 2009.
- [4] R. Lattanzi and D. K. Sodickson, "Ideal current patterns yielding optimal signal-to-noise ratio and specific absorption rate in magnetic resonance imaging: Computational methods and physical insights," *Magn. Reson. Med.*, vol. 68, pp. 286-304, 2012.
- [5] W. Schnell, W. Renz, M. Vester and H. Ernert, "Ultimate signal-to-noise-ratio of surface and body antennas for magnetic resonance imaging," *IEEE Transactions on Antennas and Propagation*, vol. 48, pp. 418-428, 2000.
- [6] M. F. Mueller, T. Lanz, F. Breuer, M. A. Griswold and P. M. Jakob, "Three-dimensional quadrature array coil elements for improved parallel magnetic

resonance imaging performance at 1.5 Tesla," *Concepts Magn. Reson.*, vol. 38A, pp. 61-73, 2011.

[7] Z. J. Wang, "Improving SNR of RF coils using composite coil elements," *NMR Biomed.*, vol. 22, pp. 952-959, 2009.

[8] W. Zhiyue J., "Towards a complete coil array," *Magn. Reson. Imaging*, vol. 26, pp. 1310-1315, 2008.

[9] K. F. Warnick, B. Woestenburg, L. Belostotski and P. Russer, "Minimizing the Noise Penalty Due to Mutual Coupling for a Receiving Array," *Antennas and Propagation, IEEE Transactions on*, vol. 57, pp. 1634-1644, 2009.

[10] M. L. Morris and M. A. Jensen, "Network model for MIMO systems with coupled antennas and noisy amplifiers," *Antennas and Propagation, IEEE Transactions on*, vol. 53, pp. 545-552, 2005.

[11] K. F. Warnick and M. A. Jensen, "Optimal Noise Matching for Mutually Coupled Arrays," *Antennas and Propagation, IEEE Transactions on*, vol. 55, pp. 1726-1731, 2007.

[12] C. Findeklee, "Array Noise Matching—Generalization, Proof and Analogy to Power Matching," *Antennas and Propagation, IEEE Transactions on*, vol. 59, pp. 452-459, 2011.

[13] S. W. Wedge and D. B. Rutledge, "Noise waves and passive linear multiports," *Microwave and Guided Wave Letters, IEEE*, vol. 1, pp. 117-119, 1991.

[14] R. P. Meys, "A Wave Approach to the Noise Properties of Linear Microwave Devices," *Microwave Theory and Techniques, IEEE Transactions on*, vol. 26, pp. 34-37, 1978.

[15] O. Pronic and V. Markovic, "Wave approach to S-parameter and noise parameter prediction of FET devices," in *Microwave and Millimeter Wave Technology, 2000, 2nd International Conference on. ICMMT 2000*, 2000, pp. 164-167.

[16] F. Wiesinger, "Parallel magnetic resonance imaging: potential and limitations at high fields," 2005.

[17] M. A. Ohliger, P. Ledden, C. A. McKenzie and D. K. Sodickson, "Effects of inductive coupling on parallel MR image reconstructions," *Magn. Reson. Med.*, vol. 52, pp. 628-639, 2004.

[18] G. Gonzalez, *Microwave Transistor Amplifiers Analysis and Design*. Englewood Cliffs, New Jersey: Prentice-Hall, INC., .

[19] J. D. Jackson, *Classical Electrodynamics*. New York: Wiley, 1975.

[20] J. R. Keltner, J. W. Carlson, M. S. Roos, S. T. S. Wong, T. L. Wong and T. F. Budinger, "Electromagnetic fields of surface coil in vivo NMR at high frequencies," *Magn. Reson. Med.*, vol. 22, pp. 467-480, 1991.

- [21] F. Wiesinger, P. Boesiger and K. P. Pruessmann, "Electrodynamics and ultimate SNR in parallel MR imaging," *Magn. Reson. Med.*, vol. 52, pp. 376-390, 2004.
- [22] F. Wiesinger, N. DeZanche and K. Pruessman, "Approaching Ultimate SNR with Finite Coil Arrays," *Proc. Intl. Soc. Mag. Reson. Med.*, vol. 13, pp. 627, 2005.
- [23] R. F. Lee, R. O. Giaquinto and C. J. Hardy, "Coupling and decoupling theory and its application to the MRI phased array" *Magn. Reson. Med.*, vol. 48, pp. 203-213, 2002.
- [24] C. Possanzini, E. Holle, M. Boutelje, M. Verheyen and P. Haans, "Balancing noise sources and coupling in phased array coils," *Proc. Intl. Soc. Mag. Reson. Med.*, vol. 15, pp. 329, 2007.
- [25] M. A. Ohliger and D. K. Sodickson, "An introduction to coil array design for parallel MRI" *NMR Biomed.*, vol. 19, pp. 300-315, 2006.
- [26] Larkman David J., "Parallel Imaging in Clinical MR Applications; The g-Factor and Coil Design" *Medical Radiology*, pp. 37 - 48, 2007.

# **Chapter 5**

## **Summary and Conclusion**

### **5.1. Summary**

To remove crosstalk between elements of an array there should be zero mutual impedance between the elements. Capacitive coupling, which has not been quantitatively studied before, was studied extensively in Chapter 2 and it was discovered that capacitive coupling can effectively remove the resistive coupling, in addition to the reactive coupling, between adjacent coils. In addition, the removal of mutual resistance results in no significant SNR or parallel imaging performance degradation. This means that the benefit of zero coupling between elements, which usually requires a special geometric arrangement of coils, can be extended to surface coils without trade-offs. The capacitive coupling itself was shown to become noticeable when the field strength is greater than 1.5T; there is a significant transfer of current between coil conductors and the mutual and self-impedance changes significantly. However, the choice of series capacitance distribution on coils, and the inclusion of parallel capacitance between coils, can mitigate these effects or use them advantageously with considerable ease when the capacitive coupling models introduced are used for prediction.

Composite coils, consisting of a standard surface coil with two additional orthogonal upright coils, were also described in detail in this thesis. The optimization of coil height was demonstrated in Chapter 3, and it was found that beyond a certain height the SNR of upright coils decreases. The coupling and noise behavior (noise covariance with adjacent surface and upright coils) was studied, showing that although there is very little noise correlation or coupling within composite coil triplets there can be significant interactions between adjacent triplets. The benefits in SNR and parallel imaging of composite arrays over just surface coils alone was demonstrated by comparing an 8 coil composite coil array against three surface coils covering the same surface area.

In Chapter 4 the comparison of surface coils and composite coils with equal numbers of elements was done. Overall, composite coil arrays show comparatively better performance as the depth increases, but the surface coil arrays have higher SNR near the periphery. Although composite arrays have marginally reduced parallel imaging performance in large element arrays, they are found to be less sensitive to noise added by preamplifiers and matching networks. Additionally, while preamplifier impedance is shown to have some effect on the final optimum SNR when preamplifier noise figure is applied individually to each coil, the difference is small. There is no difference on the optimum SNR with just matching network noise included.

## 5.2. Conclusion

The number of receive channels available is limited and the efficient use of channels requires designing arrays with the arrangement and specific coil type that provide the highest SNR and parallel imaging performance for a given channel count. Also, as the number of receive channels available increases electronic noise in preamps and matching circuits limit the SNR improvement, so the choice of coil type that avoids this limit for as high a channel count as possible is important too. Composite coil arrays are an appealing alternative to just surface coil arrays since larger body loss dominated surface coils are used in cases where three coils over the same surface would be coil loss dominated, limiting SNR improvements.

This work has confirmed that composite coils provide a viable alternative with potential benefits in performance. Their analysis validated the theoretical prediction that coils which provide electrical-dipole like currents on the surface, rather than magnetic-dipole like currents, are required at higher field strengths to approach the uiSNR. As the MRI field strength increases, and consequently the Larmor frequency, the performance of composite coils relative to surface coils alone increases. Also, Chapter 2 shows that as the frequency increases capacitive coupling becomes increasingly important, and gives practical and reliable methods for not only avoiding the effects of capacitive coupling, but using it advantageously.

### **5.3. Future Work**

The capacitive coupling model presented in Chapter 2 can be modified for large arrays with large MRI frequencies (300MHz). The complicating factor of multiple coils interacting capacitively could then be investigated as a viable research direction. In addition, the application of completely decoupled transmit coils using the capacitive decoupling method developed may show increases in the efficiency of transmit coils and lessen the design constraints of power amplifier protection, which should be investigated.

Using an n-port model of preamplifier noise the final recombined SNR depends was shown to depend greatly on the preamplifier input impedance, indicating that the n-port model warrants additional investigation and experimental testing.

The extension of the comparison between composite and surface coil arrays to the uiSNR in geometries such as planar surface or cylinders to represent other parts of the anatomy (ie. arms and legs or torso) with different electrical parameters and smaller sizes will likely result in different conclusions on the optimum array size and optimum coil type to be used. Therefore, simulations with the same method of chapter 4 will results in interesting comparisons between using composite arrays with different geometries.